

## ARTICLE

## The fluorescent toolbox for visualizing autophagy

Siyang Ding and Yuning Hong\*

Received 00th January 20xx,  
Accepted 00th January 20xx

DOI: 10.1039/x0xx00000x

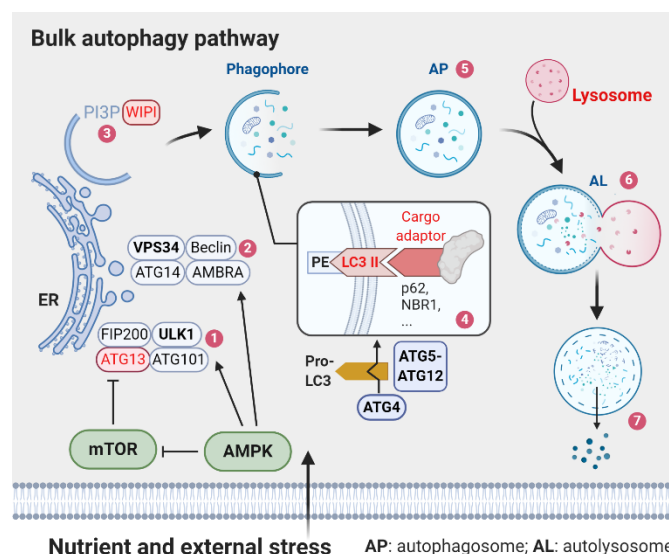
Autophagy is an adaptive catabolic process functioning to promote cell survival in the event of inappropriate living conditions such as nutrient shortage and to cope with diverse cytotoxic insults, which is regarded as one of the key survival mechanisms in living organisms. Cells perform autophagy to accomplish the lysosomal digestion of heterogenic intracellular materials including damaged proteins, organelles, and foreign bodies, in both bulky non-selective and cargo-specific manners. Studies in the past decades have shed light on the association of autophagy pathways with various diseases, which also highlighted the therapeutic value of autophagy modulation. As such, it is crucial to develop effective approaches for monitoring intracellular autophagy dynamics, yet a comprehensive account of the methodology establishment is far from complete. In this review, we aim to provide an overview of the major current fluorescence-based techniques utilized for visualizing, sensing or measuring autophagy activities in cells or tissues, which are categorized firstly by detecting targets and further by types of fluorescent tools. We will mainly focus on the working mechanisms of these techniques, put emphasis on the insight of their roles in biomedical science and provide a perspective on the challenges and future opportunities in the field.

## 1. Introduction

Autophagy (Greek for “self-eating”) is an evolutionally conserved survival pathway participating in many cellular, tissue and organismal physiological processes. Basal autophagy plays a number of vital roles in maintenance of cellular homeostasis<sup>1</sup>, such as resistance of starvation by keeping the amino acid pool recycling<sup>2</sup>, prevention of neurodegeneration<sup>3</sup>, antiaging, tumor suppression, clearance of intracellular microbes, and regulation of innate and adaptive immunity. The decline in autophagy levels is commonly associated with diseases<sup>4</sup>, including earliest stages of cancers, neurodegenerative disorders<sup>3</sup>, infectious diseases<sup>5</sup>, and inflammatory bowel disorders<sup>6</sup>. Interestingly, recent studies have revealed that the overactive autophagic process is attributed to tumor production and growth.<sup>7</sup> In this case, many efforts have been made to develop specific autophagy inhibitors that show promise in cancer treatment.<sup>8</sup> Modulating autophagy activity thus represents a new strategy for disease treatment.

Autophagy involves with the delivery of cytoplasmic cargo to the lysosomal compartment for degradation. Based on different cargo delivery intermediaries, there are three distinct forms of autophagy—macroautophagy, microautophagy, and chaperone-mediated autophagy (CMA). Macroautophagy is the process in which the cargo is sequestered within a double-membrane vesicles which further fuse with lysosomes for

degradation. Microautophagy pathway directly translocates cytoplasmic substances or soluble cellular constituents into the



**Fig. 1** The bulk autophagy pathway. Components in the pathway that have served as markers for monitoring autophagy are highlighted in red.

lysosomal lumen through the inward invagination of lysosomal membrane.<sup>9, 10</sup> Whereas for the CMA process, chaperone-mediated cargo selectivity and substrate unfolding are followed by lysosomal receptor-mediated translocation into lysosomes to achieve the removal of unwanted cytosolic contents.<sup>11</sup> Of the three types of autophagy, macroautophagy is the principal catabolic mechanism adopted by eukaryotic cells to support nutrient recycling as well as metabolic quality control and is thus extensively studied.<sup>12, 13</sup>

The current understanding of macroautophagy (henceforth termed autophagy) indicates that there are seven steps in the general autophagy mechanism, most of which are regulated by a series of evolutionarily conserved autophagy-related (ATG) genes (Figure 1).<sup>14</sup> In general, upon being triggered, signals from two major regulators of nutrient and energy stress, the mammalian target of rapamycin (mTOR)<sup>15-17</sup> and 5' adenosine monophosphate-activated protein kinase (AMPK)<sup>18, 19</sup>, activate the Unc-51-like kinase (ULK) complex<sup>20</sup> (Fig. 1, step 1), which further leads to activation of the Beclin 1 (BECN1)-VPS34 complex<sup>21, 22</sup> (step 2). Consequently, the VPS34 lipid kinase complex executes the preparation of the intracellular membranes termed phagophore, most commonly from the endoplasmic reticulum (ER)<sup>23</sup>, for autophagic vesicles (AVs) by forming phosphatidylinositol 3-phosphate (PI3P) on membranes (step 3)<sup>24, 25</sup>. This lipid enrichment supports a complex ubiquitin-like conjugation system that results in the conjugation of microtubule-associated proteins 1A/1B light chain 3B (LC3) family members to the lipid phosphatidylethanolamine (PE) on emerging AVs.<sup>26-30</sup> The lipidated form of LC3 (i.e. LC3-II) inserts on the surface of the AVs, serving as one of the major markers of AVs forming.<sup>31</sup> LC3, as a docking site for cargo adaptors, enables cargo recognition and being sequestered into the AVs (step 4).<sup>32</sup> Meanwhile, cargo receptors, such as Sequestosome 1 (also known as the ubiquitin-binding protein p62, SQSTM1/p62), bind to proteins and organelles marked for autophagic degradation (step 4).<sup>33</sup> Once the isolation membrane is enclosed with trapped cargo, the matured AVs, termed autophagosome (step 5), then fuse with lysosomes to form autolysosomes (step 6).<sup>34, 35</sup> Autophagic flux is completed with cargo and inner autophagosomal membrane being degraded by lysosomal enzymes and subsequently, recycled contents are withdrawn via nutrient transporters (step 7), continually fuelling the growth of the cell.<sup>34, 35</sup>

The above-mentioned steps are deemed to represent the dynamic features of autophagy. Under basal physiological conditions, cellular autophagic activity is usually low, but can be markedly enhanced by stimuli. Major types of autophagic inducers are classified as following: physical stress conditions (nutrient starvation<sup>2</sup>, hypoxia<sup>36</sup>, energy depletion<sup>37</sup>, ER stress<sup>38, 39</sup>, high temperature, etc.), hormonal stimulation, pharmacological agents (e.g., rapamycin<sup>40</sup>), innate immune signals<sup>5, 41</sup>, and disease conditions (bacterial/viral/parasitic infections<sup>5, 42</sup>, acute pancreatitis<sup>43, 44</sup>, heart disease<sup>45</sup>, and aggregopathies in neurodegeneration<sup>3</sup>). On the other hand, knockouts of certain ATG genes and utilization of inhibitory drugs are common methods to suppress the autophagic activities both in vitro and in vivo. It is notable that autophagy, as a multi-step process, can be blocked at different stages. Generally, sequestration inhibitors [e.g., 3-methyladenine (3-MA), LY294002 and wortmannin], inhibit the formation of phagophore. Whereas other inhibitors [e.g., leupeptin, pepstatin A, E-64d, bafilomycin A1, chloroquine (CQ) and NH<sub>4</sub>Cl] acting at post-sequestration steps to block lysosomal degradation cause the accumulation of AVs, either autophagosomes or autolysosomes, or both. However, it is

unavoidable that under certain circumstances or in some models, drug treatments may have dual effects or cause other side effects. For instance, 3-MA, which was believed to be one of autophagic inhibitors, may promote autophagy when the treatment duration is prolonged, particularly at suboptimal concentrations.<sup>46</sup> Thereby, one of the significant challenges in the analysis of the dynamic role of autophagy is to identify specific regulators and their working conditions for autophagic signalling.

Given the significance of autophagy in different physiological and pathophysiological processes, it is thus of great importance to develop and construct reliable tools or methodologies for monitoring autophagy pathway. Research in the past two decades have uncovered a vast array of homeostatic, developmental, and other physiological characteristics of autophagy, which expedites the rapid development of methods for accurate detection of autophagy activities.<sup>47</sup> The existing approaches are mostly based on biochemical changes and molecular alternations during the autophagy process. How to subtly exploit and harness the autophagy mechanism is thus the premise of sensor design.

Two major pitfalls, however, should be taken into consideration when designing or applying a novel tool for autophagy studies. First of all, static or single measurements have shown inherent limitations that lead to inevitable biological bias on the data analysis. In this regard, how to comprehensively capture and track the dynamic processes of autophagy is the primary consideration. Moreover, as alternation of specific autophagy markers may result from compromise of various external and internal factors, an overall consideration is required to yield an appropriate interpretation when applying the autophagy toolkit. A case in point is the historical misconception regarding mammalian autophagy as a cell death pathway, which are mostly caused by mistakenly assigning biological functions to autophagy based on the misreading of the detection under a given physiological condition.<sup>48</sup> Therefore, it is of great importance to separate "form" from "function" when drawing a conclusion from the measurement results.<sup>49</sup>

As more and more studies have revealed and elucidated the molecular mechanisms of autophagy pathway, a number of advanced and reliable methods have been developed. In this review, we will start from a brief introduction of non-fluorescence methods followed by a comprehensive review on fluorescent methods including protein-based biosensors and chemical probes for visualizing, sensing and measuring autophagy activities. We mainly focus on the working mechanism of the techniques in which three principal aspects of probing autophagy will be highlighted in this review: a) to probe the actual accumulation of autophagosomes and autolysosomes in the cells; b) to characterize the dynamic parameter, termed "autophagic flux", in certain cellular process; c) to develop tools for monitoring selective forms of autophagy, e.g., mitophagy, aggrephagy, etc. Limitation of each technique and future opportunity in the area will also be discussed.

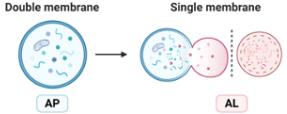
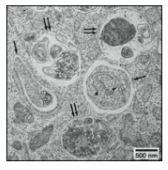

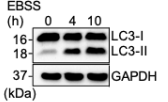
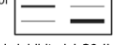
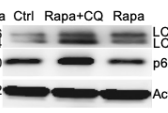
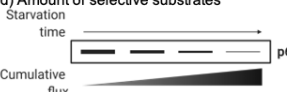
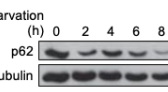
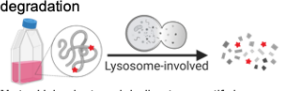
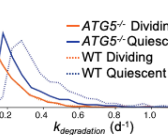
## 2. Monitoring autophagic degradation pathway by non-fluorescence methods

Autophagy was originally discovered in the late 1950s under electron microscopy (EM) observation, and since then, EM imaging has become the golden standard for autophagy research.<sup>50</sup> An autophagosome is defined as a double-membraned structure containing undigested cytoplasmic contents but has not yet fused with lysosomes. This definition provides a straightforward guidance for identifying autophagosomes under EM (Table 1, Entry a<sup>49</sup>). In addition to being time-consuming and prone to artefacts from sample preparation and fixation, unambiguously identifying autophagic structures under EM can be difficult and requires considerable experience as other cytoplasmic components, such as endosomes, swollen mitochondria, circular structures of lamellar smooth ER, etc., share similar parallel double membrane structure feature.

Utilizing EM is one of direct methods to visualise and quantify the number of autophagosomes accumulated in cells. However, the accumulation of autophagosomes can be the result of autophagic induction from the upstream or the blockage of the downstream lysosomal degradation. To clarify this, autophagic flux assays that provide direct information on lysosomal degradation of autophagic cargo should be taken into account. Conventional methods for measuring autophagic flux are based on the western blotting technology. As discussed before, LC3 turnover is one of critical markers of intracellular autophagic activities, which is based on the observation of LC3-II being further degraded in autolysosomes (Table 1, Entry b<sup>51</sup>). Theoretically, if cells are treated with lysosomotropic reagents or inhibitors of lysosomal proteases, autophagic flux will be blocked and results in the increase of LC3-II level to be seen by western blotting (Table 1, Entry c<sup>52</sup>). Nonetheless, the practical applications of this method remain challenging and limited. It is obvious that western blotting is not suitable for live contexts, not to mention live cell tracking and trafficking. Besides, a high flux can be detected even during basal conditions, particularly for some cancer cell lines, leaving a very small window to quantitatively and accurately detect changes in LC3 turnover upon autophagy upregulation.

To better demonstrate the tendency of autophagic flux, levels of other autophagy substrates are always included in the same western blotting experiment, of which the mostly studied example is SQSTM1/p62 (Table 1, Entry d<sup>53</sup>). It has been found that SQSTM1/p62 is selectively incorporated into autophagosomes through direct binding to LC3 and degraded by autophagy; thus, the total cellular expression levels of p62 inversely correlate with the level of autophagic flux. However, recent research has shown that p62 can undergo restoration upon prolonged starvation. Furthermore, both ATG-related proteins, like LC3, and autophagic substrates, such as SQSTM1/p62, are continuously expressed and transcriptionally regulated during the autophagy process, which may confound the interpretation of using them as indicators of autophagic flux. Therefore, biologists tend to combine other techniques (see below) with the western blotting-based assays to indicate

**Table 1** Non-fluorescence methods for monitoring AVs number and autophagic flux.

	Non-Fluorescence Assays	Detection methods	Example outputs
Determining AVs number	a) Morphology-dependent identification  <b>Note:</b> Differentiation of AP and AL during autophagy based on membrane structures.	Electron Microscopy	
	b) LC3-II amount (LC3-conversion)  <b>Note:</b> Upon AP accumulation, LC3-I is converted to LC3-II as an autophagy marker.	Western Blotting	
	c) LC3 turn over assay  <b>Note:</b> When flux is inhibited, LC3-II degradation is blocked, resulting in the increase of the amount.	Western Blotting	
Autophagic flux	d) Amount of selective substrates  <b>Note:</b> the amount of degradation substrates is negatively correlated with the flux intensity.	Western Blotting	
	e) Quantification of long-lived protein degradation  <b>Note:</b> Using isotope labeling to quantify lysosomal degradation of proteins to reflect the flux intensity.	Isotope release	

a. Reproduced from ref. 49 with permission from Elsevier, copyright 2010; b. Reproduced from ref. 51 with permission from MDPI, copyright 2019; c. Reproduced from ref. 52 with permission from NPG, copyright 2017; d. Reproduced from ref. 53 with permission from NPG, copyright 2010; e. Reproduced from ref. 54 with permission from National Academy of Sciences, copyright 2017.

autophagic flux under a given physiology condition.

Another traditional method to evaluate autophagic flux is to measure bulk degradation of isotope-labelled long-lived proteins, which was developed in the 1970s. Differing from short-lived proteins that are primarily degraded by proteasomes, the cellular release of radiolabelled long-lived proteins is usually quantified as the level of autophagic flux. In a proteome-wide study of cellular degradation dynamics, Ghaemmaghani et al performed stable isotope labeling by amino acids in cell culture (SILAC) in quiescent and dividing *ATG5*<sup>-/-</sup> cells, demonstrating that the blockage of autophagy leads to the decay of long-lived proteins degradation rates (Table 1, Entry e, example).<sup>54</sup> Although it may be the most effective assay so far to quantify autophagic flux by monitoring the total degradation of long-lived cellular proteins instead of a single marker, this method is not compatible with in vivo experiments and always requires extra treatment of autophagy inhibitor to ensure the accuracy of the measurement.

An overall summary of traditional non-fluorescence assays for monitoring autophagy pathway is shown in Table 1. Thanks to the rapid development of fluorescence-based techniques, using EM or western blotting to quantify the number of autophagosomes and to measure the autophagic flux has been gradually replaced by fluorescence-based methods. Compared to other methods, fluorescence-based approaches offer low background noise, high specificity and sensitivity, and more important, the opportunity to visualize dynamic biological

processes in real time in situ. The varieties of fluorescent sensors for visualizing autophagy activities can be grouped into two categories: protein-based biosensors and chemical probes. In the following sections, we will introduce these fluorescence-based assays firstly by types of fluorescence tools (marker proteins and chemical probes) and secondly by the targets of interest (i.e. forms of autophagy). Particularly, since protein-based assays are early established and well developed, this type of probes has broader applications in both bulk macroautophagy and different types of selective autophagy. We group the existing fluorescence-based autophagy tools into four sections: visualizing bulk macroautophagy by protein-based biosensors (section 3); visualizing selective forms of autophagy by protein-based biosensors (section 4); visualizing CMA by protein-based biosensors (section 5); and chemical probes for monitoring autophagy (section 6).

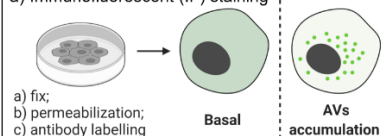
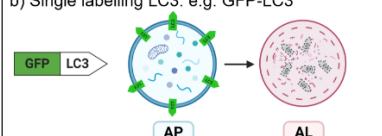
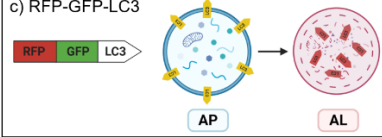
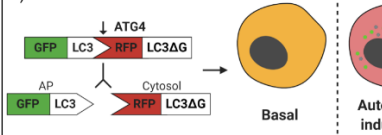
### 3. Visualizing bulk macroautophagy by protein-based biosensors

Based on the general mechanisms of autophagy discussed in the Introduction, a series of protein-based biosensors for visualizing bulk macroautophagy has been elaborately constructed and developed. There are numerous varieties of this type of autophagy sensors. In this section, we give a detailed introduction of protein-based biosensors for bulk macroautophagy by grouping them into three subclasses: a) marker proteins fused with fluorescent proteins, of which LC3 is the most commonly used one; b) pH-sensitive fluorescent proteins; and c) other important marker proteins.

#### 3.1 LC3 fused with fluorescent proteins

As noted above, the formation of LC3-II conjugated with PE is the major marker of autophagosomes and the decrease level of SQSTM1/p62 is deemed to be associated with autophagic degradation. The easiest way to qualitatively analyse these two processes is the immunofluorescent (IF) staining utilizing LC3 or SQSTM1/p62 antibodies. Among four isomers of LC3, the antibody for LC3B is the most commonly used one (Table 2, Entry a).<sup>55</sup> Antibodies of other ATG proteins are also involved depending on different research interests. However, IF staining is not compatible with live contexts due to the usage of permeabilization agents, which may also cause destructive effects to proteins, especially proteins in the lipidated form like LC3-II. Hence, methods based on the transfection of fluorescent protein tagged LC3 have been introduced and widely applied in autophagy researches, including single labelling LC3 for determining the AVs localization and tandem fluorescent tagged LC3 (tfLC3) for measuring autophagic flux. The comparison of strategies based on fluorescence proteins fused LC3 is summarized in Table 2 and will be elaborated in this section.

**Table 2** Summary of fluorescence protein tagged LC3 as markers for monitoring autophagy pathway

Fluorescence-tagged LC3	Detection Methods
a) Immunofluorescent (IF) staining 	Fluorescence Microscopy
b) Single labelling LC3: e.g. GFP-LC3 	Fluorescence Microscopy
c) RFP-GFP-LC3 	Fluorescence Microscopy; Flow Cytometry
d) GFP-LC3-RFP-LC3ΔG 	Fluorescence microscopy; Flow Cytometry; Plate reader

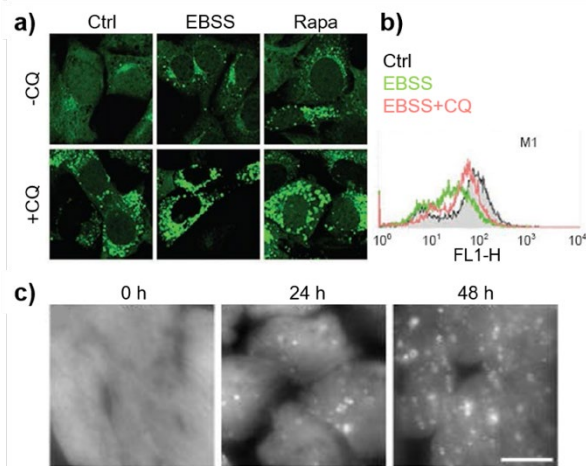
AVs: autophagic vesicles; AP: autophagosome; AL: autolysosomes

#### 3.1.1 Single labelling LC3

The newly synthesized LC3 is processed at the glycine residue on its C terminus by ATG4 to become cytosolic LC3-I,<sup>56, 57</sup> which is subsequently conjugated with PE to become LC3-II (LC3-PE) by a ubiquitination-like enzymatic reaction<sup>58</sup>. Unlike LC3-I, the designated LC3-II associates tightly with both inner and outer membranes of autophagosomes. Thus, aided by the fluorescence tag, the distribution of LC3 can serve as an indication of autophagic activities, for example, in a diffuse cytoplasmic pool (LC3-I) to represent the absence of autophagy, or in the punctate structures or even ring-shaped structures (LC3-II) that represents autophagosomes. Green fluorescent protein (GFP)-LC3 construct was the first example being generated and transfected in cells.<sup>59-64</sup> Except for GFP-LC3, plasmids of other fluorescent proteins (YFP/mCherry/RFP) tagged LC3 were also constructed and applied in various autophagy-related studies,<sup>65-70</sup> mostly being utilized as the counterparts of tfLC3 (describe below)<sup>71</sup>. It should be noted that since fluorescence of GFP is almost quenched in the acidic lysosomal environment, GFP-LC3 is normally used as the marker specific for autophagosomes, while LC3 fused with other fluorescent tags is considered labelling both autophagosomes and autolysosomes (Table 2, Entry b). This method was initially developed and verified in cell models for fluorescence microscopy imaging (Fig. 2a) and flow-cytometry analysis (Fig. 2b). Similar approaches have been successfully applied in several in vivo mammalian autophagy researches by generating GFP-LC3 transgenic mice (Fig. 2c).<sup>72</sup> Apart from the systemic GFP-LC3 transgenic mice, tissue-specific transgenic mice expressing GFP-LC3 and mCherry-LC3 have also been generated.<sup>73-75</sup> Other model organisms of interest that have



been tested with this method include *Drosophila*<sup>76, 77</sup>, *C. elegans*<sup>78</sup>, plants<sup>79</sup>, avian<sup>80</sup>, and zebrafish<sup>81</sup>. In fact, the combination of GFP-LC3 and LysoTracker Red (LTR) was also used as a live-cell imaging-based method for measuring autophagic flux.<sup>82</sup> This method has been successfully applied for determining the autophagic flux as well as the transition time by analysing the number of green (GFP, autophagosomes), red (LTR, lysosomes), and yellow puncta (GFP plus LTR, autolysosomes).



**Fig. 2** Single labelling LC3 for visualizing autophagosomes. (a) Fluorescence imaging of mouse embryonic fibroblast cells (MEFs) expressing GFP-LC3 in control (Ctrl) condition or upon EBSS or rapamycin (Rapa) treatment with or without co-incubation of CQ. (b) Representative histograms of total GFP intensity from MEFs stably expressing GFP-LC3 measured by flow cytometry. (c) GFP-LC3 images of heart muscles from transgenic mice upon 0, 24, and 48 h starvation. (a,b) Reproduced from ref. 64 with permission from NPG, copyright 2013; (c) Reproduced from ref. 72 with permission from ASCB, copyright 2004.

The transfection of GFP-LC3 generally works well in model studies but several limitations of this assay should be kept in mind especially in the interpretation of LC3 localization. Firstly, it has been found that LC3 tends to aggregate and incorporate into other aggregation-prone proteins, such as inclusion bodies induced by polyglutamine (polyQ) expression or formed in autophagy-deficient hepatocytes, neurons, or senescent fibroblasts.<sup>83</sup> In these cases, drawing conclusions about cellular autophagy activity in accordance with punctate dots observed under fluorescence microscopy may confound the final results. There are also precautions that can be conducted to possibly reduce the formation of GFP-LC3 aggregation. One is to avoid the use of transit transfection and only select clones that express appropriate levels of GFP-LC3 without artificial aggregation in stable-expressing cells. Another way, which appears the most essential to eliminate the influence of LC3 aggregation, is using a C-terminal glycine mutant GFP-LC3<sup>G120A</sup> as an inserted parallel control.<sup>84</sup> Assuming that both wild-type and mutant GFP-LC3 forms are expressed at a comparable level, in the scenario of autophagosome accumulation, the puncta number of wild-type GFP-LC3 should increase while that of mutant GFP-LC3 remains nearly unchanged. Secondly, it is conceivable that the background fluorescence signal of the cytosolic LC3-I may affect the quantitative analysis of the

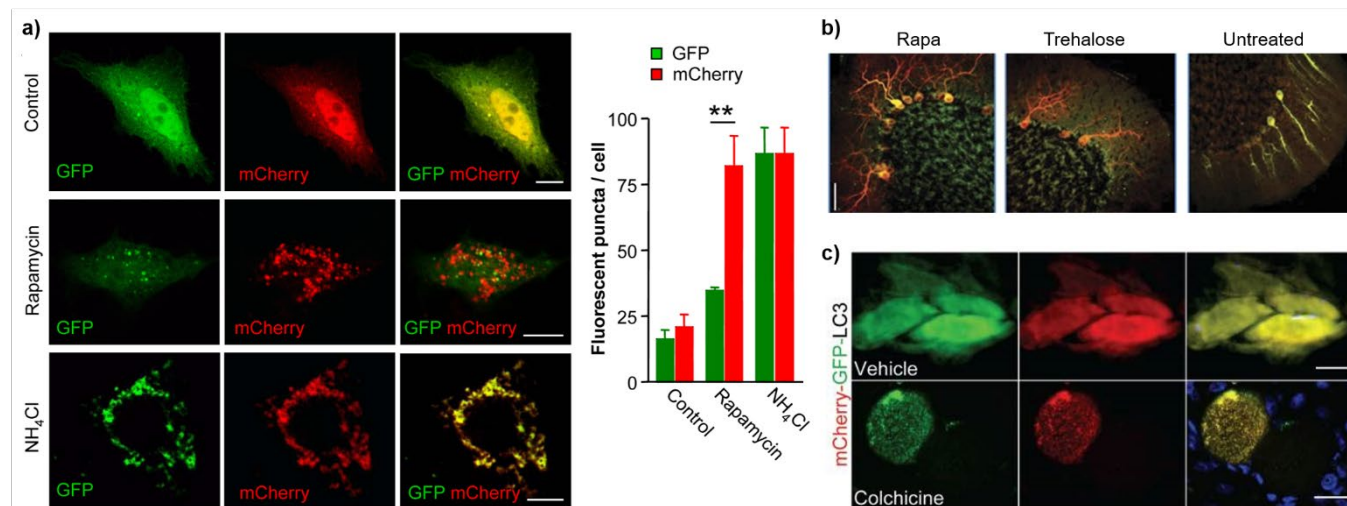
autophagosome accumulation, particularly for experiments based on flow cytometry. This pitfall has been tackled by the selective extraction of LC3-I using short-term saponin treatment, which was proven to be rapid and less subjective.<sup>85</sup> Although there are still some other shortcomings of this approach, generally it is widely applicable in most of basic autophagy researches.

### 3.1.2 Tandem fluorescent tagged LC3 (tfLC3)

Along with the process of autophagy, matured autophagosomes undergo the fusion process with lysosomes that provide an acidic environment and digestive function to the interior of autophagosomes to form autolysosomes. During the formation of autolysosomes, the LC3-II inserted on the double membrane of autophagosomes is cleaved off by ATG4 and degraded by lysosomal enzymes, finalising the whole process of the autophagy pathway. Thereby, the decrease amount of LC3-II can be used as an indicator of autophagic flux. As mentioned before, it was found that GFP-LC3 loses fluorescence due to lysosomal acidic conditions,<sup>59, 86</sup> whereas YFP/RFP/mCherry-LC3 remains emissive when encountering with lysosomes<sup>87</sup>.

Taking advantage of this property, mRFP-GFP tandem fluorescent-tagged LC3 (tfLC3) was designed and developed by Yoshimori et al for specifically monitoring the autophagosome maturation process.<sup>71</sup> In cells transfected with this construct, the yellow dots (GFP + RFP) and the red dots (RFP only) indicate the location of autophagosomes and autolysosomes, respectively (Table 2, Entry c). In comparison with the control condition, the induction of autophagy, for instance, by rapamycin (Rapa), leads to the increased number of red dots, whereas the addition of lysosomal inhibitor, such as NH<sub>4</sub>Cl, results in the accumulation of yellow dots (Fig. 3a).<sup>88</sup> On the basis of this hypothesis, the level of autophagic flux can be estimated by calculating the ratio of GFP/RFP signals obtained from the flow-cytometry setup,<sup>89-93</sup> which is supposed to inversely correlate with cellular autophagic flux. Notably, when using tfLC3 to monitor autophagic flux, its parallel control tfLC3<sup>G120A</sup> transfection should also be conducted to confirm the localization of tfLC3 is indeed autophagy-dependent.<sup>71</sup> As for the *in vivo* models, the tfLC3 based method is proven to be applicable in numerous organs in mice, including the nervous system (Fig. 3b)<sup>94, 95</sup>, postischemic kidneys<sup>96</sup>, heart<sup>97</sup>, skeletal muscle (Fig. 3c)<sup>98</sup>, liver<sup>99</sup>, and retina<sup>99</sup>. To further improve data reliability and veracity of tfLC3 probe, mWasabi, a fluorescent protein that is more sensitive to the acidic environment, was used to replace GFP.<sup>100</sup> In comparison with mRFP-GFP-LC3, mTagRFP-mWasabi-LC3 has much brighter fluorescence and has been shown to efficiently avoid misinterpreting autophagic flux results.

Contextually, as the cellular autophagic activity is a multistep bulk degradation pathway, it should be emphasized that it is equally important to develop strategies for quantitative analysis of original data acquired from aforementioned approaches for systematic studies in autophagy-related research. Based on confocal images, Spirito et al. developed an analysis method to accurately measure the number and pH of AVs by using tfLC3 as a ratiometric pH sensor, termed AIPD



**Fig. 3** Applications of tandem fluorescent tagged LC3 in cells and in vivo. (a) Localization of GFP and mCherry signals in Vero cells transfected with mCherry-GFP-LC3 plasmid under control condition or upon rapamycin/NH<sub>4</sub>Cl treatment. Quantification of the number of fluorescent puncta exhibiting green (GFP) or red (mCherry) fluorescence in cells shown at the right panel. Scale bar, 10  $\mu$ m. (b) Visualisation of the LC3 flux in the cerebella crest of mice injected with AAV2/2\_mCherry-GFP-LC3 under untreated condition or after trehalose/rapamycin treatment. Images show the merge channels of GFP and mCherry signals. Scale bars, 30  $\mu$ m. (c) Fluorescence images of the tibialis anterior muscle from mice electroporated with the mCherry-GFP-LC3 construct upon vehicle or colchicine (a microtubule depolarizing agent that can block autophagosome maturation to autolysosomes and increased LC3-II levels) treatment. Scale, 25  $\mu$ m. (a) Reproduced from ref. 88 with permission from PLOS, copyright 2013; (b) Reproduced from ref. 95 with permission from NPG, copyright 2013; (c) Reproduced from ref. 98 with permission from Elsevier, copyright 2015.

analysis.<sup>101</sup> In this way, the cellular autophagic states can be characterized by a continuous pH distribution (ranged from pH 4.5–6.5), which allows an elaborate quantification of autophagic flux by retrieving the concentrations of autophagic intermediates. Also, a comprehensive theoretical account of measuring autophagic flux is reported by Hofmeyr et al to provide a standardized approach that, hopefully, is useful for establishing systematic flux databases of clinically relevant cell and tissue types.<sup>102</sup>

Although tflc3 is suitable for short-term tracking of individual autophagic structures, it is unavoidable that RFP would eventually be degraded in the lysosome, which greatly limits its application in the assessment of autophagic flux in whole organisms. The reformative version of tflc3, GFP-LC3-RFP-LC3 $\Delta$ G, was developed to quantitatively monitor cumulative degradation of an autophagic substrate, which can be distinguished from reduction of its synthesis without extra treatment of lysosomal inhibitors.<sup>103</sup> In GFP-LC3-RFP-LC3 $\Delta$ G construct, GFP-LC3 is fused to the N terminus of RFP-LC3 $\Delta$ G whose C-terminal glycine is deleted. In cells expressing GFP-LC3-RFP-LC3 $\Delta$ G, this probe is cleaved by endogenous ATG4 family proteases<sup>58, 104</sup> in cytosol to produce equimolar amounts of GFP-LC3 and RFP-LC3 $\Delta$ G. Afterwards, GFP-LC3 takes part in the cellular autophagy, whereas the lipidation process of RFP-LC3 $\Delta$ G is blocked, owing to the lack of glycine on the C terminus, to obstruct it from being associated with autophagosomes, thus stably persisting the RFP signals in the cytoplasm as a long-term internal control (Table 2, Entry d). Immunoblotting analysis in Fig. 4a shows that GFP-LC3-RFP-LC3 $\Delta$ G is completely cleaved depending on the glycine at the end of the first LC3, fully supporting the design rationale of the probe. Further experiments revealed that among the cleavage products, GFP-

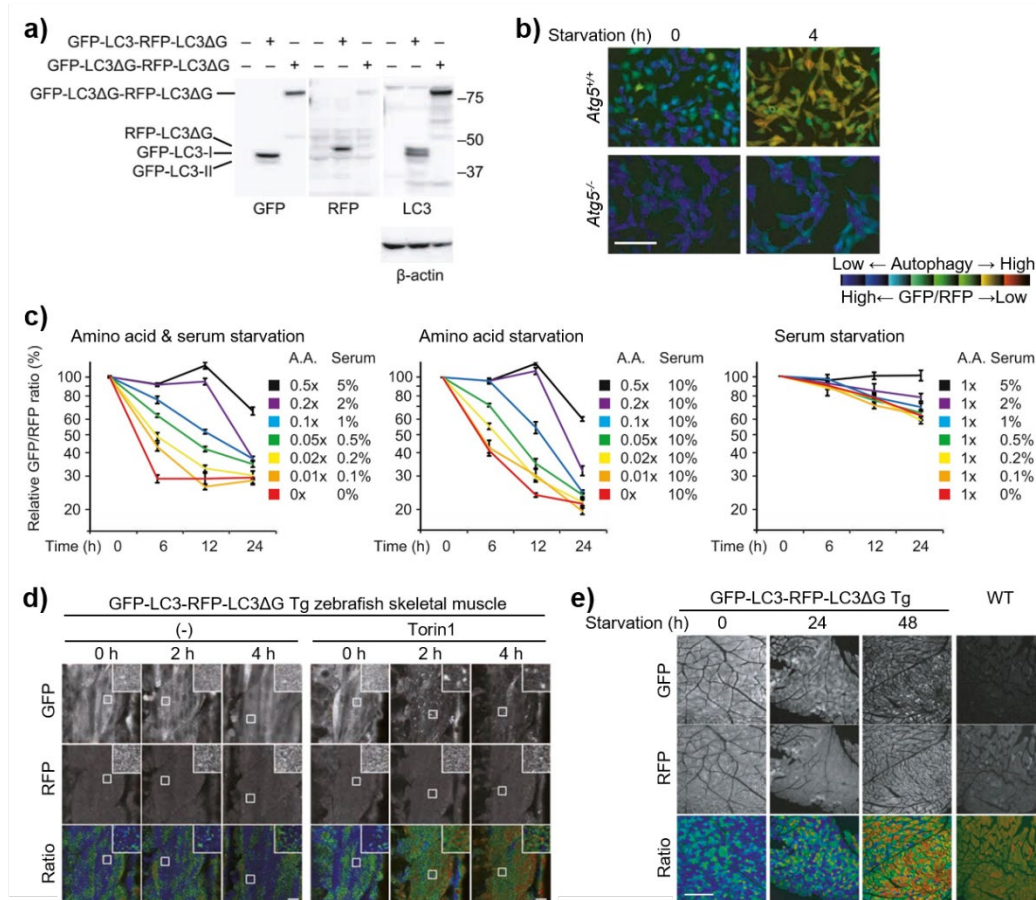
LC3, but not RFP-LC3 $\Delta$ G, was degraded in a starvation- and Atg5-dependent condition (Fig. 4b). Subsequently, this probe was utilized in the detection of a series of autophagy-related systems, including the starvation induced autophagy (Fig. 4c), re-evaluation of autophagic interferents, and screening of approved drug library for autophagy modulators. Moreover, the probe was also examined to be applicable for in vivo measurement of basal and induced autophagic flux in embryos and tissues of zebrafish and mice (Fig. 4d and 4e).<sup>105</sup>

### 3.2 pH-sensitive protein markers

As we illustrated above, the utility of tflc3 for measuring autophagic flux is attributed to the distinct pH-sensitivity between GFP and RFP/mCherry. Lysosomal acidic environment quenches the GFP signal but not RFP/mCherry and in this case, the color change in the merged images of two channels indicates the translocation of LC3 from autophagosomes to autolysosomes. Apart from tflc3, in this section, other pH-sensitive protein markers that have been reported as autophagy sensors by exploiting the lysosome-involved nature of this pathway will be introduced.

#### 3.2.1 Rosella

Rosella, a fluorescent pH-biosensor comprised of a fast-maturing pH stable red fluorescent protein (DsRed) and a pH-sensitive green fluorescent protein variant (super ecliptic pHluorin, SEP), was developed by Devenish et al as an alternative monitoring system for reporting vacuolar turnover of cytosol and organelles during autophagy processes in yeast.<sup>106</sup> Differing with tflc3 that is used for tracking a specific biomarker, in this case, the N-terminal end of Rosella was designed as an open box that enables further conjunction with subcellular targeting sequence for mitochondria (citrate



**Fig. 4** Validation and application of cleavable GFP-LC3-RFP-LC3ΔG. (a) Immunoblotting analysis of MEFs stably expressing GFP-LC3-RFP-LC3ΔG or GFP-LC3ΔG-RFP-LC3ΔG. (b) Fluorescence GFP/RFP ratiometric images showing wild-type and *Atg5<sup>-/-</sup>* MEFs stably expressing GFP-LC3-RFP-LC3ΔG that were starved (depletion of both serum and amino acids) for the indicated timepoints. Scale bar, 100 μm. (c) Detection of starvation-induced autophagy using a microplate reader. HeLa cells stably expressing GFP-LC3-RFP-LC3ΔG were cultured in medium containing the indicated concentration of fetal bovine serum and amino acids for the indicated times (mean ± SEM, n = 4). The GFP/RFP fluorescence ratio is expressed as a percentage relative to that at time 0. Data are representative of at least three independent experiments. (d) Representative fluorescence ratio images of skeletal muscle in GFP-LC3-RFP-LC3ΔG transgenic zebrafish under control (-) condition or upon Torin1 (an autophagy inducer by inhibiting mTOR) treatment for indicated timepoints. Scale bar, 10 μm and 2 μm (inset). (e) Representative fluorescence ratio images of gastrocnemius muscles of GFP-LC3-RFP-LC3ΔG transgenic mice starved for indicated timepoints and wild-type mice. Scale bar, 200 μm. Reproduced from ref. 103 with permission from Cell Press, copyright 2016.

synthase-targeting sequence) or nucleus (NAB35) in yeast cells (Fig. 5a). In the absence of autophagy, the unmodified Rosella remains in the neutral pH cytoplasm where it emits both red and green fluorescence. Following the induction of bulk autophagy, Rosella is targeted to the vacuole in yeast. The acidified environment quenches the fluorescence of SEP but not DsRed, leading to an observation of red emission only (Fig. 5b), which clearly delimitates different stages of the intracellular autophagy pathway.

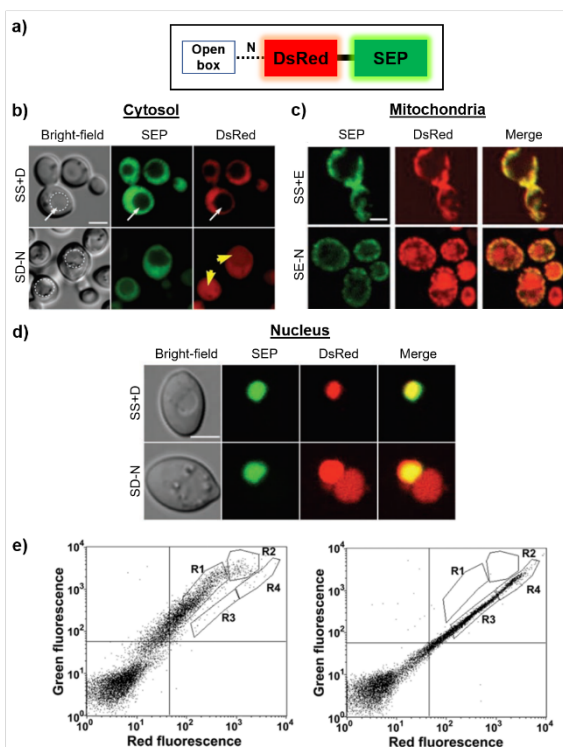
Moreover, when fused with a mitochondria-targeting sequence, Rosella can be used to track the selective autophagy of mitochondria, or mitophagy. As shown in Fig. 5c, red fluorescence in the vacuole during the starvation represents autophagy-dependent delivery of Rosella to the vacuole from mitochondrial matrix. Interestingly, only a small portion of cells showed the delivery of nucleus-targeting Rosella to the vacuole under nitrogen starvation conditions (Fig. 5d), indicating that the delivery of NAB35-Rosella to the vacuole is only partially

dependent on the autophagic machinery of the cell. Coupled with the usage of fluorescence-activated cell sorting (FACS) technology, Rosella sensor can be used as a tool for analysing and enriching populations of yeast cells undergoing autophagy of the nucleus (Fig. 5e). Collectively, Rosella is a facile tool to evaluate the uptake of intracellular compartments into yeast vacuoles for elucidating mechanistic aspects of the autophagy pathway.

### 3.2.2 Keima

In section 3.1.2, we have introduced biosensors generated by tandem fusion of pH-insensitive and pH-sensitive fluorescent proteins and their applications in various autophagy-related studies. However, there are a few factors that may affect the sensitivity and accuracy of those probes: a) the pH-insensitive fluorescent protein remained in the system largely depends on the sensitivity of the biosensor to lysosomal proteases, which was rarely tested in previous reports; b) the red-to-green





**Fig. 5** Rosella biosensor for visualizing autophagy in yeast. (a) Schematic representation of the Rosella construct. (b–d) Bright-field and fluorescence images of (b) cytosol-targeting, (c) mitochondria-targeting and (d) nucleus-targeting Rosella expressed wild-type yeast under growing conditions (SS+D) and after nitrogen starvation (SD-N) for (b) 4 h, (c) 6 h and (d) 24 h. (e) FACS analysis of yeast cells expressing the nucleus-targeted Rosella under growing (left) and nitrogen starvation conditions (right).  $10^4$  cells were counted for each experiment. R1, R3 and R2, R4 encompass cells with 'mid' or high levels green and red fluorescence, respectively. Scale bar, 2  $\mu$ m. (b–e) Reproduced from ref. 106 with permission from Taylor & Francis, copyright 2008.

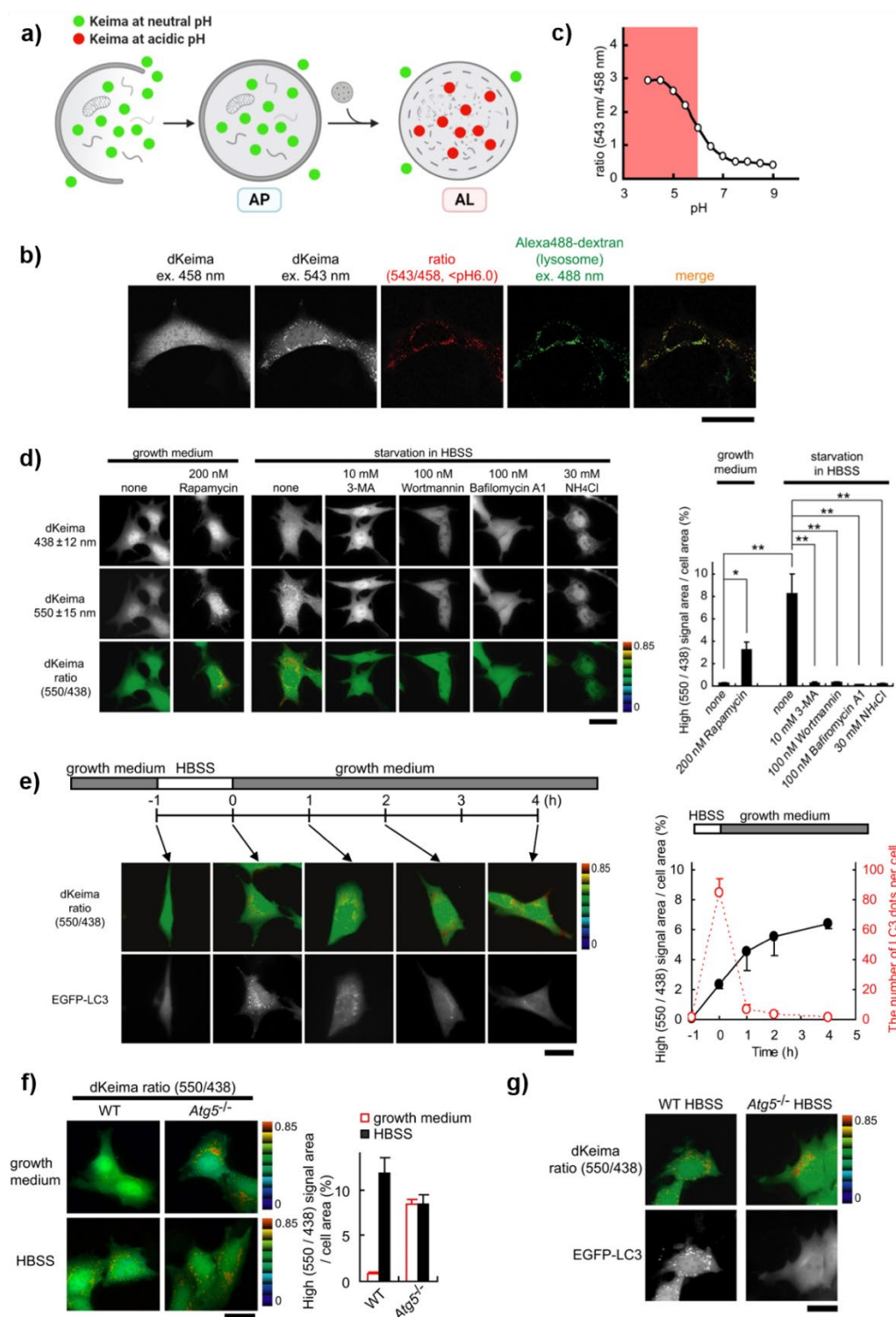
emission intensity ratio of this type of probes may be inevitably affected by different maturation rates of the proteins, fluorescence resonance energy transfer (FRET), and proteolytic cleavage between two proteins. To overcome these problems, Keima, a coral-derived acid-stable fluorescent protein that enables dual-excitation ratiometric pH measurements, was introduced for detecting cellular autophagic flux in a more comprehensive and reliable manner.<sup>107</sup> With a pKa of 6.5, Keima processes a bimodal excitation spectrum (Fig. 6a) peaked at 440 and 586 nm, which correspond to the neutral and charged states of the chromophore's phenolic hydroxyl at neutral/basic (pH > 6.5) and acidic (pH < 6.5) environments, respectively. Both excitations lead to the same emission maximum at 620 nm. Taking advantage of its pH-dependent excitation and resistance to lysosomal proteases, Keima-based assay was developed by Miyawaki and co-workers to provide a cumulative readout for flux quantification at a particular time point. Two versions of Keima, monomeric Keima (mKeima) and dimeric Keima (dKeima), were generated in this study. Owing to the faster

maturation property, dKeima was chosen to monitor different types of autophagy including macroautophagy and microautophagy in cells. Dual excitation ratiometric imaging revealed bright punctate structures with a higher ratio of excitation at 550/438 nm (pseudo red colour in Fig. 6b), which corresponds to the formation of autolysosomes. In combination with Alexa 488-conjugated dextran, a lysosome marker, the punctate structures high 550/438 nm excitation ratio were confirmed to localise in lysosomes (Fig. 6b). Note that the unique photophysical property of dKeima allows the simultaneous imaging with another green-emitting fluorophores such as Alexa 488 by using sequential scanning by using 458, 543 and 488 nm laser on confocal microscopes. A pH titration curve of dKeima in solution by using the same setting supports that a higher ratio (543/458) reflects a lower pH environment (Fig. 6c). These results verified that higher ratio than the basal corresponds to the signals in lysosomes and proves the hypothesis that dKeima-based assay could be used for visualizing autophagic events in cells.

Upon rapamycin treatment or starvation (HBSS culturing)-induced autophagy, those high ratio structures appear in dKeima-expressing MEF cells to indicate the cumulative autophagic flux in cells. When cells are treated with autophagy inhibitors, such as 3-MA, Wortmannin, Bafilomycin A1 and  $\text{NH}_4\text{Cl}$ , only basal level of ratios of excitation at 550/438 nm were observed (Fig. 6d). Differing from EGFP-LC3 dots that emblems the number of autophagosomes, the signals from Keima increases cumulatively over time and can be measured at any time point to quantify cumulative autophagic flux (Fig. 6e), making this technique amenable to high-throughput screening of autophagy regulators.

Conventional LC3-based biosensors are not able to detect *Atg5*-independent autophagy, a recently discovered type of macroautophagy, as ubiquitin-like protein systems were silenced in this type of autophagy.<sup>108</sup> Remarkably, in this study, dKeima was demonstrated to be capable of detecting and quantifying *Atg5*-independent autophagy in *Atg5*-deficient (*Atg5*<sup>-/-</sup>) MEFs (Fig. 6f). Such process was not detected by using LC3-associated systems (Fig. 6e,g). Therefore, it is believed that dKeima can serve as a more reliable tool to provide sufficiently quantitative data for *Atg5*-independent autophagy compared with previously adopted approaches such as hand-pick autophagosomes and autolysosomes by EM or quantification of autophagic activity by lysosomal protein (e.g. LAMP-2) immunofluorescence. The major limitation of Keima series, however, is the incompatibility with cell fixation because the lysosomal acidity could be destructed in fixed cells, leading to misconception of results.





**Fig. 6** Keima biosensor for measuring cumulative autophagic activity in live cells. (a) Schematic representation of autophagy detection with Keima. Green and red colors represent the excitation of Keima by 458 and 543 nm lasers, respectively. (b) Dual-excitation ratiometric imaging reveals the colocalization of high ratio (550/438) dKeima signals with lysosomal marker Alexa488-dextran in dKeima-expressing MEF cells. (c) pH titration curve of dKeima in solution. (d) Dual-excitation channel and ratiometric images of dKeima-expressing MEF cells incubated under indicated conditions. High ratio (550/438) signals are shown as red. Right: statistics analysis illustrating the proportion of the high ratio (550/438) signal area (red) to the total cellular area in 30 transfected cells calculated for each experiment. \* $p < 0.05$ , \*\* $p < 0.02$ . (e) Imaging of EGFP-LC3 and dKeima co-expressing MEFs acquired at the beginning (-1 h) and end (0 h) of the starvation period as well as after the growth medium was replaced (1, 2, and 4 h). Right: time-course chart shows the proportion of the high ratio (550/438) signal area (red) to the total cellular area in 30 transfected cells (black solid circles) and the number of EGFP-LC3-positive aggregates per cell (red open circles) plotted over time. (f) Left: dual-excitation ratiometric imaging of WT and *Atg5*<sup>-/-</sup> MEFs incubated in growth or starvation medium (Hank's Balanced Salt Solution (HBSS)). Right: statistics analysis illustrating the proportion of the high ratio (550/438) signal area (red) to the total cellular area in 30 transfected cells calculated for each experiment. (g) Simultaneous observation of EGFP-LC3 and dKeima in WT and *Atg5*-deficient (*Atg5*<sup>-/-</sup>) MEF cells stably expressing EGFP-LC3 under starvation conditions. Scale bar, 20  $\mu$ m. (b-g) Reproduced from ref. 107 with permission from Cell Press, copyright 2011.

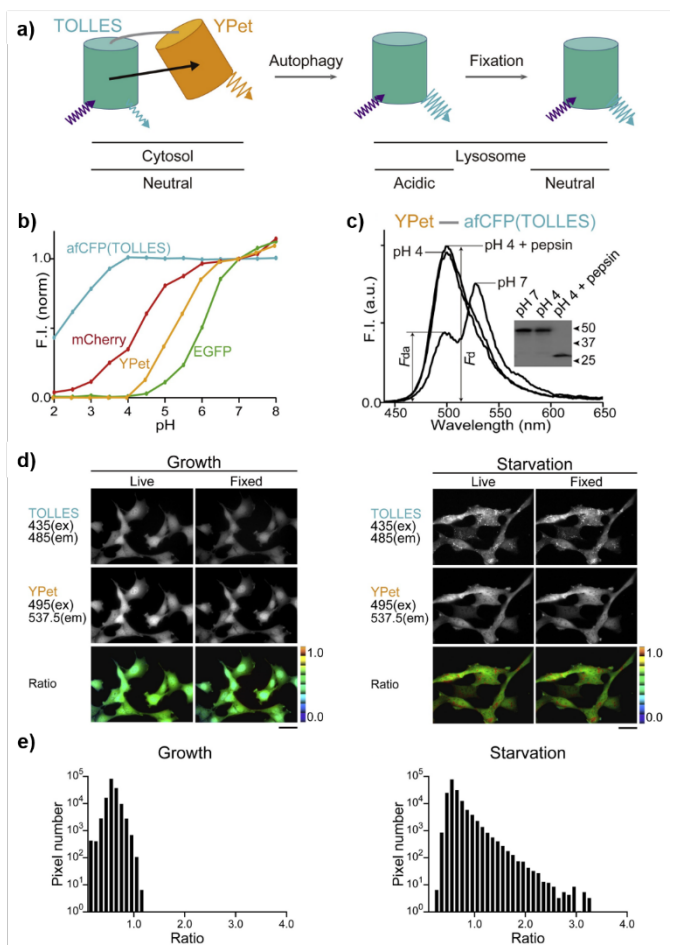
### 3.2.3 Signal-retaining autophagy indicator

Most recently, Miyawaki and coworkers reported another autophagy-related biosensor, termed signal-retaining autophagy indicator (SRAI), with improved properties compared to their previous invention of dKeima.<sup>109</sup> The hypothesis here is to use a fluorescence protein with constant spectral properties within the pH range of lysosomal and neutral cytoplasmic environments, and secondly, resistant to lysosomal protease-mediated degradation. The existing tandem fluorescent biosensor mCherry-GFP, however, cannot fulfil this need because little was known about its acid-sensitivity and FRET efficiency within the pair. TOLLES (TOLerance of Lysosomal Environments), a cyan-emitting fluorescence protein derived from mAG (monomeric AzamiGreen, a green-emitting fluorescence protein), stood out in the screening of a library of fluorescence proteins originated from Anthozoans, which suits the above requirements. SRAI with a tandem construct by coupling TOLLES with a moderate pH-sensitive yellow-emitting fluorescence protein, YPet, was introduced (Fig. 7a). The pH titration curves confirmed the stability of TOLLES over a wide range of pH while YPet was sensitive to the pH between 4–6 and completely quenched when pH < 4 (Fig. 7b). In lysosome-mimicking buffer (pH 4), YPet was irreversibly acid-denatured and degraded by pepsin, providing a noticeable contrast with environmentally stable signals from TOLLES (Fig. 7c). Ratiometric images clearly demonstrated distinct TOLLES distribution in SRAI-expressing MEF cells after incubation in normal growth or starvation medium (Fig. 7d). In cells cultured in growth medium, SRAI fluorescence was homogeneously dispersed, whereas the HBSS starvation-induced autophagy resulted in the formation of TOLLES puncta with high ratio values (Fig. 7e) due to the substantial quenching and/or digestion of YPet in lysosomes. Remarkably, signals of SRAI exhibit great tolerance with fixation procedures, as an improvement from Keima, which greatly prolongs the observation time and thus allows accurate statistical analysis. By virtue of the dual-excitation dual-emission ratiometric approach and the new data mining algorithm, SRAI was expected to be applicable for quantitative assessment of autophagic flux with a high signal-to-noise ratio in an image-based setup.

### 3.3 Other fluorescence tagged proteins for autophagy research

Apart from the usage of the fluorescence tagged LC3 and pH-sensitive fluorescence proteins, a few other methods based on different mechanisms for autophagic flux measurement have also been reported, which provide alternative choices in various models.

SQSTM1/p62, one of ubiquitin-binding autophagy receptors mentioned before, can be recognized by LC3 and degraded through the autophagy pathway. It is used to determine the cellular autophagic flux in the western blotting assay as one of most conventional methods in autophagy research. Taking advantage of this property, Carlisle et al designed and established a novel approach for monitoring autophagic flux in



**Fig. 7** SRAI biosensor for visualizing autophagy in live and fixed cells. (a) The design and working mechanism of SRAI - a tandem fusion of YPet and TOLLES. (b) pH titration curves of the emission of afCFP (TOLLES), YPet, mCherry, and EGFP, normalized against the values at pH 7. (c) Emission spectra and protein stability of YPet-afCFP (TOLLES) after 18-h incubation at 37°C at pH 7, pH 4, and pH 4 in the presence of pepsin. Measurements were performed after neutralization. Inset, immunoblotting with antibody against mAG. (d) Ratiometric imaging of SRAI-expressing MEF cells incubated in growth or starvation medium. Images acquired before and after fixation are shown. Scale bar, 20 μm. (e) Histograms of TOLLES/YPet ratios from SRAI-expressing MEF cells after incubation in growth or starvation medium. Reproduced from ref. 109 with permission from Cell Press, copyright 2020.

an image-based high content siRNA screening.<sup>110</sup> In the GFP-SQSTM1 expressing cells, reduction in fluorescence of GFP-labelled SQSTM1 in combination with either an increase or decrease in colocalization with lysosome marker was interpreted as an increase in autophagic flux, which was used as the first-step measurement in the screen flow. Coupled with viability test, mTOR-dependence assay, and tfLC3 autophagic flux measurement, this high-throughput time-lapse imaging assay was further utilized to assess candidate gene modulators of autophagic flux, which has identified previously undescribed regulatory mechanisms of known autophagy-involved proteins in two cell lines, human osteosarcoma cells (U2OS) and human neuroglioma cells (H4). Similar notion was also applied to determine the impaired levels of macroautophagy in immunosenescent T cells, for which the colocalization between

LC3 and lysosome marker was measured.<sup>111</sup> Notably, it is essential to incorporate other methods to testify the measurement of substrate-lysosome colocalization and to yield a convincing conclusion regarding autophagic flux, as whether those known substrates are diametrically specific to be degraded via autophagy pathway remains further verified.

Recently, the dual role of autophagy as both inhibitor and stimulator in cancers has been utilized for potential anticancer treatment. The studies of 2-dimensional (2D) monolayers and 3-dimensional (3D) multicellular spheroids mesothelioma cell lines, ex vivo 3D tumor fragment spheroid, and formalin-fixed tissue, shown that ATG13 is a better static marker of the autophagic flux in 3D models in comparison to the most commonly used LC3.<sup>112</sup> The positivity of ATG13 was found to have a strong correlation with prognosis of patients with mesothelioma, which was compatible with tissue microarrays and provided informative clinical outcome independent of known prognostic factors. ATG13 is thus considered more suitable for utilizing in measuring autophagic flux in fixed tumor samples which could be relevant to tumor prognosis.

WIPI1 and WIPI2 from human WD-repeat protein interacting with phosphoinositide (WIPI)  $\beta$ -propeller protein family have also been exploited as additional targeting sites for imaging autophagy process due to their specific binding to PI3P at the onset of autophagy. Researches have shown that human WIPI1 and WIPI2 are involved in the upstream of autophagy specifically in ATG12 and LC3 conjugation systems, where the PI3P effector activity of WIPI1 and WIPI2 promotes the lipidation of LC3-I to form LC3-II.<sup>113-117</sup> Hence, GFP-WIPI1 was stably expressed in U2OS cells as a tool for monitoring cellular autophagy process using fluorescence microscopy.<sup>118</sup> Specifically, upon starvation, the fluorescence signals of GFP-WIPI1 translocate from cytoplasm to the initiation site where autophagosomes are forming and eventually become punctate structures which can be used as the marker of phagophores and autophagosomes. Quantitative WIPI puncta assessment was subsequently developed, which served as a valuable tool for automated high-throughput/content image acquisition and quantification in system biology of autophagy.

#### 4. Visualizing selective autophagy by protein-based biosensors

Although autophagy was initially defined as a relatively non-selective mechanism adopted by eukaryotic cells to degrade and recycle cytoplasmic entities, the selectivity machinery of autophagy for specific cellular constituents as well as pathogens has been well established nowadays.<sup>119</sup> The selectivity of cargo docking is achieved by a plethora of selective autophagy receptors that are capable to recognize and sequester specific cargo.<sup>120</sup> Superimposed on the core autophagy machinery, the engagement of selective autophagy receptors then initiates the general macroautophagic process to fulfil the cargo degradation. To date, various types of selective macroautophagy have been identified and well characterised, including mitophagy<sup>121</sup>, pexophagy<sup>122</sup>, ER-phagy<sup>123</sup>,

ribophagy<sup>124, 125</sup>, lipophagy<sup>126</sup>, lysophagy<sup>127, 128</sup>, aggregophagy, xenophagy<sup>129, 130</sup>, ferritinophagy<sup>131, 132</sup>, proteaphagy<sup>133, 134</sup>, glycophagy<sup>135</sup> and nucleophagy<sup>136, 137</sup>. Table 3 summarises the definitions and classification of major selective forms of autophagy, among which mitophagy is arguably the best-studied form of selective autophagy, with a fast increase of biosensors for mitophagy visualization in recent years. However, fluorescence-based biosensors for other forms of selective autophagy remain limited or even none, which greatly impedes the future exploration in these areas. Note that more and more researchers have raised interrogation to question the nature of basal and selective autophagy since investigations focusing on specific autophagic substrates sometimes may omit the concomitant degradation of other cytoplasmic components during the same process. Hence, tools for discriminating cargo selection in autophagy pathway are urgently needed and will facilitate to solve related questions.

**Table 3** Summary of selective forms of autophagy.

Category	Selective forms of autophagy		Definition <sup>119</sup>
Organelles		Mitophagy	The specific removal of damaged or excess mitochondria by micro- or macroautophagy.
		Pexophagy	A macroautophagic response preferentially targeting peroxisomes.
		ER-phagy (reticulophagy)	The preferential autophagic degradation of portions of the ER.
		Ribophagy	A specific autophagic response targeting ribosomes.
		Lysophagy	The specific macroautophagic disposal of damaged lysosomes.
		Lipophagy	The selective autophagic degradation of neutral lipid droplets.
		Proteaphagy	Macroautophagic responses specific for inactive proteasomes.
		Nucleophagy	An autophagic response selectively targeting portions of the nucleus.
Cytotoxic molecules		Ferritinophagy	Selective autophagy-mediated degradation of iron-sequestering protein ferritin.
		Aggregophagy	An autophagic response specific for protein aggregates.
		Glycophagy	Selective autophagy-mediated degradation of glycogen.
Pathogens	Xenophagy	Virophagy	A macroautophagic response targeting fully formed cytoplasmic virions or components thereof.
		Bacterial xenophagy	The macroautophagic removal of cytoplasmic bacteria.

In Section 3, we have summarized the usage of protein-based biosensors functioning in the core autophagic machinery to visualize bulk macroautophagy. Here we centre around the selective forms of autophagy and give some examples to illuminate the design strategies for biosensor construction.

#### 4.1 Targeting mitophagy

Mitochondria have evolved sophisticated homeostatic mechanisms of quality control to ensure the requisite number of functional mitochondria and constitute mitochondrial turnover.<sup>138</sup> Mitophagy, a selective form of autophagy, functions for the elimination of damaged or superfluous mitochondria to restore energy metabolism<sup>139</sup>, during which the entire mitochondria are sequestered by autophagosomes followed by lysosomal fusion for degradation. Mitophagy was first visualized in EM imaging of cultured cells<sup>140</sup>, and since then, numerous fundamental biochemical steps in pathways directing mitochondria to autophagy system have been uncovered and well-studied. Basically, mechanisms of mitophagy can be classified as ubiquitin-dependent and ubiquitin-independent pathways. In yeast, Atg32 is essential for mitophagy that occurs in response to enforced respiration but not for non-selective autophagy under nutrient-deprivation conditions or for other selective autophagy such as pexophagy.<sup>141-143</sup> Atg32 was found to anchor on the outer mitochondrial membrane (OMM) and contain a WXXL-like Atg8-binding motif in its cytosolic domain, which facilitates the direct interaction of Atg32 with Atg8. Alternatively, Atg32 can indirectly associate with Atg8 bridged by Atg11 that is known to recruit a range of cargoes, including peroxisomes, into autophagosomes by interacting with Atg8. Although several researches have pointed out that Atg32 indeed participates in mitochondrial quality control in yeast cells<sup>143</sup>, the mechanism about how the expression and activity of Atg32 are regulated to eliminate the appropriate number of mitochondria remains an intriguing area for further study. Since Atg32 has no known metazoan homologue, it is believed that the process in mammalian cells possess completely different molecular mechanisms of mitophagy compared to yeast. During key processes of development, the programmed mitochondrial clearance in reticulocytes<sup>144-146</sup> is achieved by mitophagy, which requires the involvement of OMM protein NIP3-like protein X (NIX or BNIP3L).<sup>147-149</sup> NIX contains a similar WXXL-like motif that can directly recruit isolation membranes to mitochondria by binding with the mammalian Atg8 orthologue, LC3, and the LC3 homologue, GABA receptor-associated protein (GABARAP).<sup>150, 151</sup> This NIX-dependent mitophagy in reticulocytes also requires the participation of two core autophagic proteins, ULK1 and ATG7.<sup>144-146</sup> In another aspect, our understanding about how mammalian cells discriminate and eliminate damaged mitochondria is largely driven from two genes that are mutated in early-onset recessive Parkinson's disease (PD) – the kinase PTEN-induced putative kinase protein1 (*PINK1*)<sup>152</sup> and the E3 ubiquitin ligase *Parkin*<sup>153</sup>. When mitochondria are damaged and lose their membrane potential, these proteins operate in a common pathway, PINK1-Parkin pathway, to ubiquitylate mitochondrial proteins on OMM,<sup>154, 155</sup> eliciting the engulfment to isolated double-membrane in concert with autophagic cargo receptors and subsequent degradation via lysosomal hydrolases<sup>156</sup>.

Nowadays, alterations in mitophagy have been increasingly linked to instances of disease ranging from diabetes to neurodegeneration, as well as aging. On one hand, some

pathological proteins produced during disease progressions can disrupt the quality-control machinery of the cell including maintaining the requisite number of mitochondria. On the other hand, monitoring the process of mitophagy would provide a novel strategy for developing and screening drugs that regulate this process for therapeutic purpose. Hence, it is highly desirable to develop tools and models for mitophagy monitoring. In this section, protein-based fluorescence biosensors for quantitative studies of mitophagy will be introduced. Their working mechanisms and applicability, advantages and limitations will also be included.

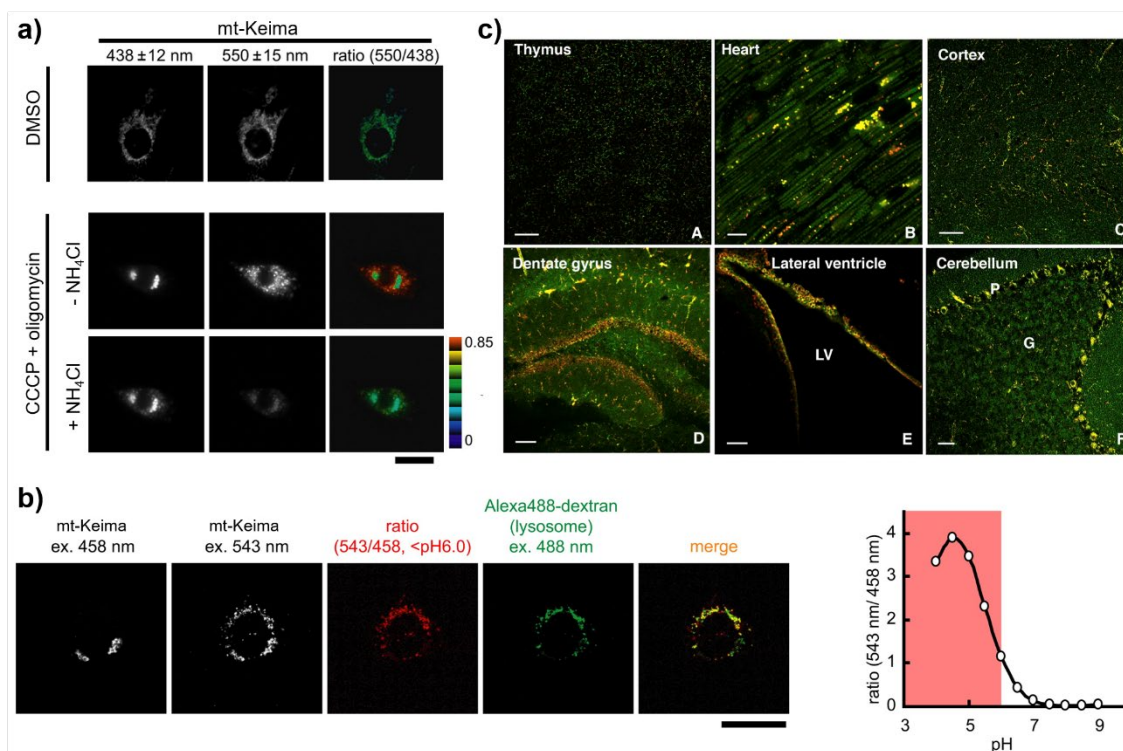
##### 4.1.1 mt-Keima

Proceeded with the achievement of dKeima to quantitatively monitor bulk autophagic events in cells, mKeima, which processes larger responses to pH changes, was engineered to localize to the matrix of mitochondria by fusing a tandem repeat of the COX VIII pre-sequence to facilitate the visualization of the mitophagy pathway.<sup>107</sup> The resultant construct, named mt-Keima, was generated, which can be controlled by the Ponasterone A-induced transcription in order to further enhance the mitochondria-anchoring specificity. In Parkin-overexpressing MEF cells, the transient expression of mt-Keima triggered by Ponasterone A treatment was localized in mitochondria without generating high ratio of signals excited at 550/438 nm under vehicle condition (Fig. 8a). However, after co-incubation with carbonyl cyanide m-chlorophenylhydrazone (CCCP) and oligomycin to depolarize mitochondria, strong signals of mt-Keima in 550 nm excitation window were detected, where punctate structures were formed throughout the cytoplasm (Fig. 8a), indicating that a large fraction of mitochondria was delivered to lysosomes. The dual-excitation (550/438) ratiometric image clearly presented a different distribution between intact (green) and degraded (red) mitochondria, which cannot be observed when lysosomes were neutralized by the treatment of NH<sub>4</sub>Cl (Fig. 8a). Subsequently, the localization of the high ratio mt-Keima signals in lysosome was confirmed by the pH titration curve, in which the high ratio mt-Keima signals were corresponded to pH<6.0 (Fig. 8b, right). Aided by the capability to qualitatively measure mitophagic flux, mt-Keima has been increasingly employed in many mitophagy-related studies.<sup>157-159</sup>

In addition to intracellular applications, a transgenic mouse model expressing mt-Keima has been generated, through which the ratiometric images of mt-Keima signals revealed the basal levels of mitophagy between and within tissues (Fig. 8c).<sup>160</sup> The mouse model was further tested under a variety of environmental and genetic perturbations including diet, oxygen availability, Huntingtin's disease transgene expression, deletion of *Atg5* or *Atg7*, the presence of metastatic tumors, and normal aging. Results suggested that the decline in mitophagy is the primary cause of mitochondria damage and dysfunction in diseases or aging-related processes.

These results suggested that mt-Keima is not only useful for molecular studies of in vitro mitophagy, but also provides a convenient and robust strategy for assessing in vivo mitophagy. However, it should be noted that the Keima protein experiences





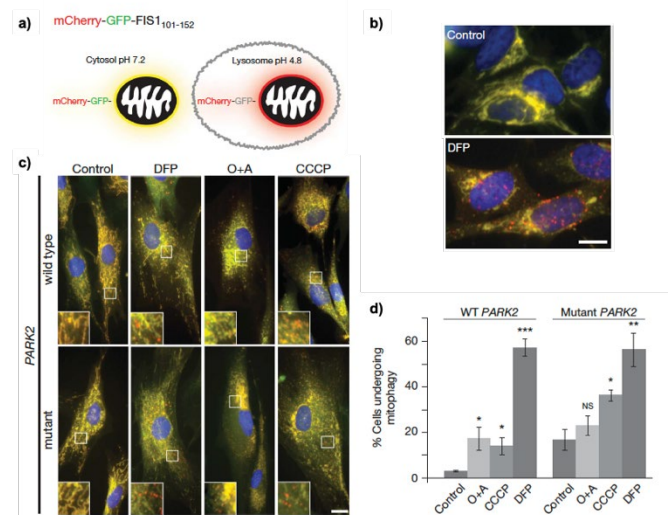
**Fig. 8** Measuring mitophagy in cells and in vivo by mt-Keima. (a) Dual-excitation ratiometric imaging of mt-Keima in Parkin-overexpressing MEF cells following a treatment with DMSO (vehicle alone) or with CCCP+oligomycin (for depolarizing mitochondria) before or after the addition of NH<sub>4</sub>Cl. (b) Left: dual-excitation confocal images reveals the colocalization of punctate structures with high ratio (543/458) mt-Keima signals with lysosomal marker Alexa488-dextran signal in mt-Keima expressing MEF cells. Scale bar, 20  $\mu$ m. Right: pH titration curve of mt-Keima in solution. (c) Fluorescence imaging of mt-Keima signals between and within tissues: (A) thymus, (B) heart, (C) cortex, (D) dentate gyrus, (E) lateral ventricle (LV) and (F) cerebellum (P: the purkinje cell layer; G: the granular layer). Scale bar, 50  $\mu$ m (for A, C, E and F), 10  $\mu$ m (for B), 100  $\mu$ m (for D). (a,b) Reproduced from ref. 107 with permission from Cell Press, copyright 2011; (c) Reproduced from ref. 160 with permission from Cell Press, copyright 2015.

a gradual shift in its fluorescence excitation during pH variation, which could overlap with its emission spectra. This may hamper the accuracy of mitophagy measurement in vivo due to the complex tissue environments and tedious section preparation process. Moreover, due to the incompatibility with the conventional fixation process (*vide supra* section 3.2.2), sections from the mt-Keima mouse model must be imaged immediately after preparation, which might not be feasible with certain applications or might be likely to cause certain unwanted ambiguity.

#### 4.1.2 mCherry-GFP-FIS1<sub>101-152</sub>

To circumvent the problem that Keima protein is incompatible with fixation, Ganley et al modified the tandem tag mCherry-GFP with the OMM localization signal of the protein FIS1 (residues 101-152) to afford mCherry-GFP-FIS1<sub>101-152</sub> as a biosensor to monitor mitophagy.<sup>161</sup> This construct has similar working mechanism of mCherry-GFP-LC3 but with specific mitochondrial targeting capability. As illustrated in Fig. 9a, mitochondria can exhibit dual-color emission under normal conditions but once fused with lysosome, the GFP signal will be quenched and only red emission from mCherry will be observed. Cells expressing mCherry-GFP-FIS1<sub>101-152</sub> were used to perform the chemical screen for mitophagy inducers, from which the

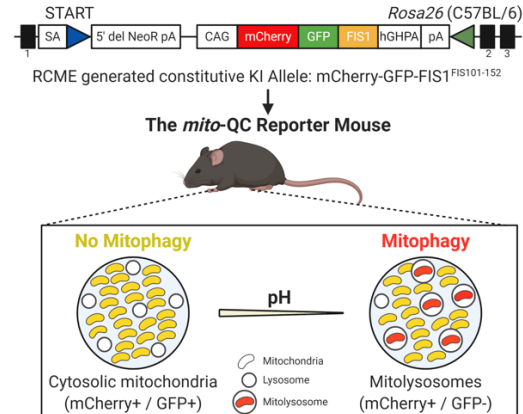
iron chelator deferiprone (DFP) was found to have the strongest mitophagy-inducing effect (Fig. 9b). Subsequently, mCherry-GFP-FIS1<sub>101-152</sub> was transfected in primary human dermal fibroblasts from a healthy individual (as WT *PARK2*) and a patient with early-onset Parkinson's disease (as mutant *PARK2*). Quantitative analysis of the dual-color emission imaging revealed mutant *PARK2* cells exhibited a higher basal level of mitophagy than WT *PARK2* (Fig. 9c, d). Moreover, the biosensor indicated DFP induced a much higher mitophagy level in both WT and mutant *PARK2* cells than the other drug treatment such as CCCP and combination of oligomycin A and antimycin A (O+A) (Fig. 9c, d). With aid of western blotting, their study suggested that iron chelation can serve as a strong *Parkin*-independent activator of mitophagy. Collectively, the great sensitivity of mCherry-GFP-FIS1<sub>101-152</sub> can facilitate the identification and characterization of potential therapeutic regimens for diseases where mitophagy plays a key role in the clearance of pathogenic factors.



**Fig. 9** Quantification of mitophagy in cells by mCherry-GFP-FIS1<sub>101-152</sub>-based mitophagy assay. (a) Schematic representation of working mechanism of tandem-tagged mCherry-GFP-FIS1<sub>101-152</sub>-based mitophagy assay. (b) Dual-color fluorescence images of cells expressing mCherry-GFP-FIS1<sub>101-152</sub> under control or DFP treatment. (c) Visualization of mitophagy in human primary fibroblasts from a control individual (wild-type) and an early-onset Parkinson's disease patient (mutant) transfected with mCherry-GFP-FIS1<sub>101-152</sub>. Cells were treated with DFP (1 mM), CCCP (20 μM) or oligomycin A (10 μM) + antimycin A (1 μM) (O+A) for 24 h. Scale bar, 10 μm. (d) Quantification of percentage of cells undergoing mitophagy in the same conditions of (c). Reproduced from ref. 161 with permission from EMBO Press, copyright 2013.

To continue the *in vivo* application of mCherry-GFP-FIS1<sub>101-152</sub>, Ganley et al further developed a transgenic mouse model expressing quality-control (QC) signal of mitochondria, named *mito-QC* (Fig. 10a), which allows the assessment of autophagic turnover of mitochondria and mitochondrial architecture *in vivo* at single-cell resolution within multiple organ systems.<sup>162</sup> The appearance of punctate mCherry-only foci can be identified and quantified as an index of cellular mitophagy (Fig. 10). In conjunction with histochemistry techniques, *mito-QC* has been utilized tissue-wide to reveal previously unknown biological pertaining to mitophagy and mitochondrial organization. The results show that embryonic heart (E17.5 heart) undergoes mitophagy only in restricted cellular zones where in the adult heart, the mitophagy level is in general lower but homogeneously distributed across all the cells in the heart tissue. *mito-QC* further reveals the physiological mitophagy in muscle tissue, liver, spleen, the nervous system and kidneys, highlighting the complex and selective nature of mitophagy within distinct cellular subsets.

Compared with mt-Keima, *mito-QC* affords superior versatility by presenting a simple binary-based readout (green, mitochondria; red, mitolysosome) instead of the gradual spectra changes. Also, the compatibility of *mito-QC* with immunohistochemistry allows its applications in tissue-wide imaging for quantifying global mitophagy in different organs, and for simultaneously identification of specific cellular subtypes using antibody staining. Cautions should be borne in mind when using *mito-QC* since it has been found that a fixative at pH 7 is crucial for the consistency in the readouts of *mito-QC*. Moreover, traditional heat-mediated antigen-retrieval



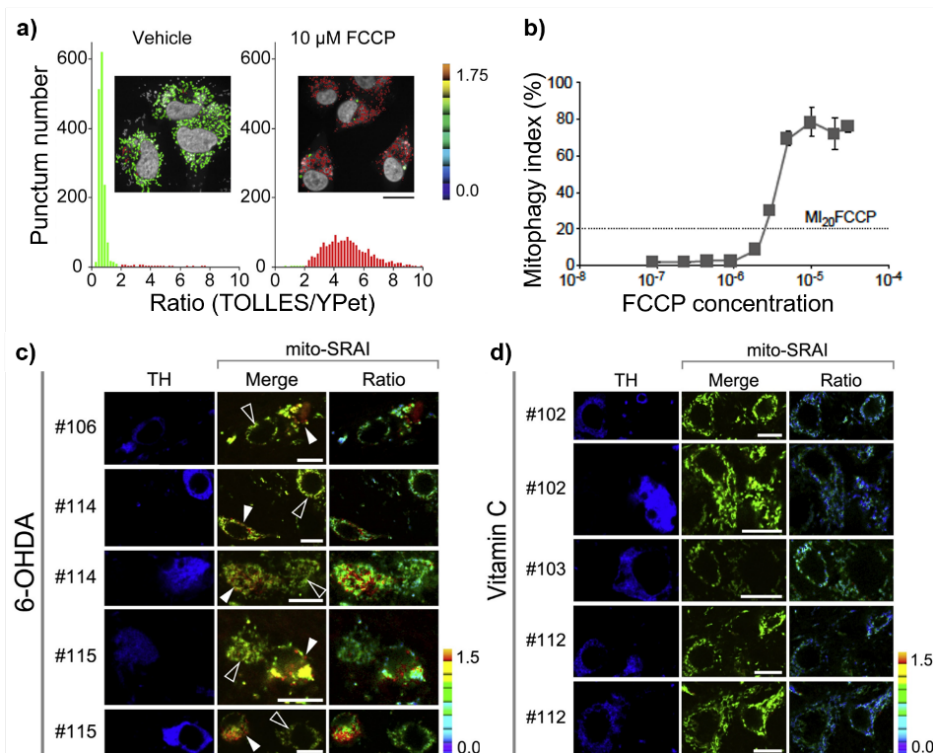
**Fig. 10** The design of *mito-QC* for illuminating mitophagy *in vivo*. (top) Schematic of gene targeting strategy used to generate the *mito-QC* mouse model. (bottom) The illustration of the optical readout of *mito-QC* in response to mitophagy.

techniques should be avoided when using *mito-QC* because of the incompatibility.

#### 4.1.3 mito-SRAI

To resolve the fixation-resistant problem and improve the reliability of mitophagy quantification concurrently, Miyawaki et al further engineered SRAI to localize into the mitochondrial matrix by fusing a tandem repeat of the COX VIII pre-sequence and adding two degrons, CL1 and PEST, resulting in mt-SRAI-CL1-PEST (or *mito-SRAI*).<sup>109</sup> The combination of the mitochondria-anchoring segment and degrons successfully eliminates the non-target signals of the construct, achieving mitochondrial specificity comparable to that of mt-Keima. The mitochondrial localization of *mito-SRAI* in MEFs is further secured by the usage of a tetracycline (Tet)-inducible gene expression system.<sup>163</sup> Subsequently, a reproducible expression system was established in the human glioblastoma H4 cell line co-expressing *mito-SRAI* and Parkin (H4/Tet-on:*mito-SRAI*/Parkin) and tested in control with DMSO (vehicle) or carbonyl cyanide *p*-trifluoromethoxyphenylhydrazone (FCCP) (Fig. 11a). As an uncoupling agent, FCCP was chosen to prepare damaged mitochondria to enhance mitophagy. The mitophagy index (MI) was defined as the area ratio of lysosomal (TOLLES only) to total signals (TOLLES-YPet FRET) in this system, from which a sigmoidal dose (FCCP concentration)-response (MI) relationship with small standard deviations was established (Fig. 11b). This result indicates that FCCP-dependent mitophagy is tolerant of cell cycle arrest, making it possible for this approach to be adapted for high-throughput screen of chemical libraries that contain cell cycle dysregulators. Therefore, the *mito-SRAI*-based assay was used for the screening and identified a therapeutic mitophagy enhancer that can act on damaged mitochondria prepared by FCCP-elicited 20 % MI (MI<sub>20</sub>FCCP).

Additionally, *in vivo* expression of *mito-SRAI* in neurons from the substantia nigra pars compacta (SNc) of C57BL6/J mice was achieved by using an adeno-associated virus (AAV) system. A Parkinson's disease model was generated by injecting 6-



**Fig. 11** Measuring mitophagy index by mt-SRAI. (a) Histograms of TOLLES/YPet ratios from puncta of H4/Tet-On:mito-SRAI/Parkin cells after incubation with vehicle (DMSO) and 10  $\mu$ M FCCP. Insets show the representative ratiometric images of cells under these two conditions. TOLLES was excited by 425 nm and YPet by 488 nm. Scale bars, 20  $\mu$ m. (b) The correlation of FCCP concentrations and mitophagy index (MI [%]). MI was defined as the area ratio of lysosomal signals (as red puncta) to total signal (green+red puncta).  $MI_{20FCCP}$  is the FCCP concentration that leads to 20% MI. (c-d) Representative fluorescence images of TH immunostaining (blue) and mitophagy signals (merge and ratio images of TOLLES and Ypet channels) from midbrain sections of (c) 6-OHDA-injected and (d) Vitamin C-injected mice. Mouse sample numbers are indicated in the leftmost column. TH-negative, mitophagy-positive neurons and TH-positive, mitophagy-negative neurons are labeled with solid and open triangles in (c), respectively. Scale bars, 10  $\mu$ m. Reproduced from ref. 109 with permission from Cell Press, copyright 2020.

hydroxydopamine (6-OHDA), a neurotoxin, into the SNc. Immunostaining with tyrosine hydroxylase (TH) reveals the 6-OHDA-induced mitophagy occurs in non-dopaminergic neurons (TH-negative), which were immediate neighbors of TH-positive neurons (Fig. 11c). This observation partially explains the loss of dopaminergic neurons in the SNc during PD-related progressions. On the other hand, ascorbic acid injection leads to no change in mitophagy signals (Fig. 11d). Collectively, these results emphasize the critical role of mitophagy in mitochondrial quality control mechanism to promote cell survival.

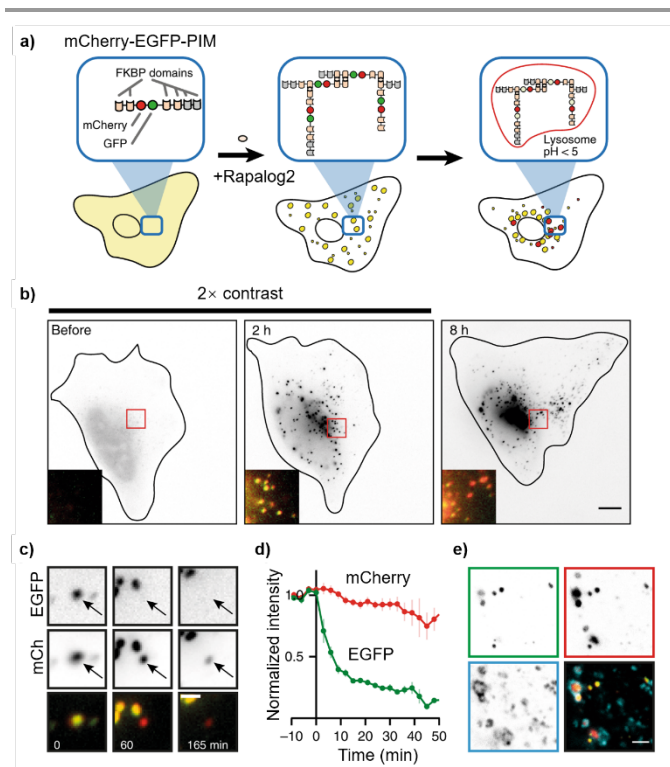
Aided by the addition of Tet-inducible gene expression system, mito-SRAI can be used effectively without the constitutive expression-generated basal mitophagy, which was found to be particularly useful in interpretation of mitophagic gene-involved pathways (e.g. PINK-Parkin pathway<sup>164</sup>). Furthermore, mito-SRAI, which anchors inside the mitochondrial matrix, can escape from the proteasomal attack, where *mito-QC*, which locates at the cytoplasmic site of the OMM, may be susceptible to proteasomal degradation. Therefore, it was concluded that mito-SRAI possesses many advantages for a proper and consistent measurement for mitophagy in a variety of biomedical applications.

Apart from mitophagy reporters shown here, there are more and more emerging fluorescence protein-based tools for studying mitochondrial dynamics. For instance, MitoTimer, a molecular clock for mitochondrial turnover, was constructed by utilizing the characteristic fluorescence shift of DsRed1-E5, a mutant of DsRed, from green to red as the protein matures.<sup>165</sup> Owing to the significant role of mitochondria, it is conceivable that the advance of sophisticated research tools will accelerate the mechanistic investigation of the mitochondria and the role of mitophagy in both physiology and pathology progressions.

## 4.2 Targeting aggrephagy

Autophagy that can selectively eliminate aggregated proteins, termed aggrephagy, is essential to maintain protein homeostasis to remove damaged proteins.<sup>166</sup> Aggrephagy is closely correlated to a number of diseases, including cancer and neurodegeneration.<sup>4, 167-171</sup> However, the active induction of aggrephagy by simply introducing aggregation-prone proteins has been found to be infeasible. The aggregation-prone proteins may undergo clearance over time and/or negatively affect cell health and disrupt the autophagy pathway, which precludes the temporal control of such biosensor.<sup>172, 173</sup> A typical example is the expanded polyQ proteins, which perturb the cellular autophagic regulations via interfering with polyQ-





**Fig. 12** Monitoring aggrephagy by mCherry-EGFP-PIM biosensor. (a) Mechanistic illustration of mCherry-EGFP-PIM biosensor, in which cluster formation and degradation lead to yellow (EGFP+mCherry) and red (mCherry only) signals in cells, respectively. (b) Inverted contrast gray scale images of mCherry channel from HeLa cell expressing PIM construct after transfection for indicated timepoint. Insets show merged image of mCherry and EGFP channels. The image contrast in the left and middle panel are 2× that of the right panel. (c) Time-lapse images of an individual cluster. Arrow tracks cluster showing color conversion. (d) Normalized mCherry (red) and EGFP (green) fluorescent intensity of individual clusters versus time (mean ± s.e.m. n = 9 clusters). t = 0 marks entry into lysosome. (e) Immunofluorescence images of clusters in HeLa cells 24 h after cluster formation. Panels show endogenous staining of LAMP2A (cyan panel), clusters in mCherry (red panel) and EGFP channel (green panel). Reproduced from ref. 174 with permission from NPG, copyright 2018.

based protein-protein interactions.<sup>172</sup> In consequence, tools to directly induce and monitor aggrephagy pathway are limited.

To address this problem, Kapitein et al developed an inducible aggregate-forming system to create small fluorescent-tagged FKBP particles (particles induced by multimerization (PIMs)), mCherry-EGFP-PIM, based on a chemically induced dimerization approach (Fig. 12a).<sup>174</sup> Using this approach, PIMs can be generated in cells by expressing the construct including an array of FKBP12 domains, whereby the comprised four repeats of variant FKBP domain (FKBP\*) in this array undergo homodimerization upon addition of the rapamycin-analog AP20187 (rapalog2) that has been proven to have no impact on basal autophagy. Likewise, the usage of a dual fluorescent tag allows the direct observation of cargo delivery to the lysosome, thus achieving the accurate quantification of the flux of aggregate turnover by autophagy. Upon expression in HeLa cells, mCherry-EGFP-PIM firstly showed diffused distribution in the cytosol before the addition of rapalog2. Next, the rapalog2-induced homodimerization concentrates the transfected protein to form yellow mCherry-EGFP-PIM clusters in the cell. In accordance with live-cell imaging shown in Fig. 12b and 12c,

clusters start switching from yellow (EGFP+mCherry) to red (mCherry only) approximately after 2 h of their formation, losing nearly 70% of the EGFP fluorescence (Fig. 12d). Immunofluorescence images of HeLa cells expressing PIM construct show that the red clusters are well colocalized with the lysosome marker LAMP2A (Fig. 12e), confirming the occurrence of lysosomal fusion. Quantitative analysis of the images reveals an average autophagic flux of 3.4 clearance events (clusters) per hour per cell in this system is calculated. Moreover, results also indicate that the PIM clusters are ubiquitinated and recruit p62/SQSTM1, NBR1, and LC3 before final degradation in lysosomes, serving as a tool for probing the dynamic properties of aggrephagy. Interestingly, cells with high PIM-protein expression initially shown some clearance of small aggregates, but then bigger clusters were also formed by merging multiple PIMs, which might imply another protective mechanism existing (i.e. aggresomes<sup>175</sup>) when the clearance machinery is overwhelmed.

Other systems for aggrephagy monitoring include the luciferase-based reporters developed by Jäättelä et al and Weihi et al, which have also been used for quantitation of both bulk autophagy or selective aggrephagy in vitro and in vivo.<sup>176, 177</sup> Current tools for aggrephagy studies are still limited. Future work is required to uncover how cells sense their aggregate burden and determine which clearance mechanism to use. With this information, aggrephagy-specific biosensors with improved performance will be explored.

## 5. Visualizing CMA by protein-based biosensors

Chaperone-mediated autophagy (CMA), as a part of cellular proteostasis networks, is a selective mechanism for the degradation of cytosolic proteins via lysosomes.<sup>178-180</sup> Two unique features of CMA regarding substrate identification and translocation into lysosomes make it distinct from the other types of autophagy.<sup>11</sup> In detail, the cargo selectivity of CMA is originated from the recognition of the CMA-targeting chaperone – heat shock cognate 71 kDa protein (HSC70)<sup>181, 182</sup>, which can only bind to the KFERQ-like motif-bearing residues<sup>181, 183</sup>. Basically, HSC70 participates in multiple cellular processes to assist during both folding of de novo synthesized native proteins and unfolding of originally folded proteins. Also, the relevance of cytosolic HSC70 with autophagy has been greatly expanded beyond CMA, suggesting its central role in protein triage among three different types of autophagy.<sup>184, 185</sup> In the CMA pathway, upon recognizing the “bait” provided by the KFERQ-like motif, the chaperone/substrate complex is directed to the lysosomal receptor, lysosome-associated membrane protein type 2A (LAMP2A)<sup>186, 187</sup>, with the aid of a series of cochaperones<sup>188, 189</sup>. Unfolding of the substrate protein then occurs on the outer lysosomal membrane<sup>190</sup>, followed by the internalization into lysosomes mediated by the receptor LAMP2A and the assist of resident lysosomal HSC70 (lys-HSC70)<sup>191, 192</sup>. Once in the lysosomal lumen, CMA substrates are rapidly degraded by a diverse range of proteases.

LAMP2A is the only one of the three splice variants of a single gene, *LAMP2*<sup>193</sup>, contributing to CMA processes, which



acts as the rate-limiting component in different steps of this pathway. First, the 12-amino-acid cytosolic tail of LAMP2A is essential for lysosomal docking of HSC70-substrate complexes.<sup>186, 187</sup> Next, substrate translocation across lysosomal membrane into the lumen entails LAMP2A assembly into a 700kDa multimetric protein complex to facilitate ablated substrate binding and internalization.<sup>194-196</sup> Therefore, blockage of LAMP2A is the most effective way to inhibit CMA activity in cells. Moreover, CMA flux can be regulated by interferences in expression levels and dynamics of LAMP2A on the lysosomal membrane. Owing to the critical roles of LAMP2A and HSC70 in CMA, the most popular approach reported so far for evaluating CMA activity was to use antibodies against LAMP2A and HSC70 to label CMA-active lysosomes or for biochemical analysis with isolated lysosomes.<sup>196</sup> Except for their incompatibility with live cells or in vivo system, these methods require intricate experimental procedures and suffer from lack of sensitivity.

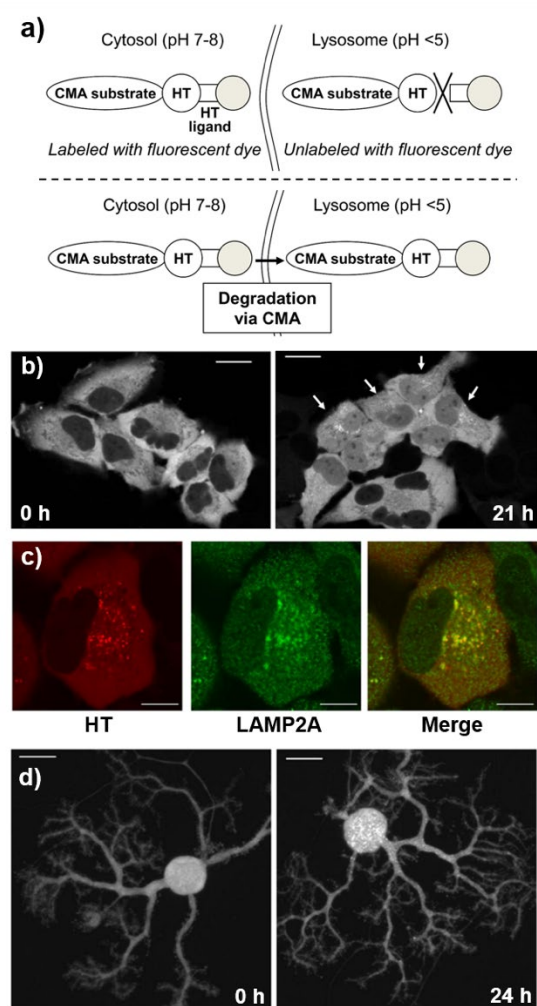
CMA activation can be induced in response to external stresses such as mild oxidative stress<sup>197, 198</sup>, genotoxic damage<sup>199</sup> or hypoxia<sup>200</sup>, accompanying with transcriptional upregulation of LAMP2A. On contrary to macroautophagy which has been well-studied, rigorous mechanistic study of CMA regulatory functions and related disease models is required. More and more evidence has shown that CMA decline with age may aggravate diseases, especially age-related neurodegeneration and cancers.<sup>167</sup> However, the difficulty in monitoring CMA in intact cells greatly hampers the study of CMA pathophysiology. In this section, we focus on fluorescent CMA substrates, a novel approach for CMA detection emerging in the recent decade. There are two design strategies of fluorescent CMA substrates highlighted in the following discussion: a) using additional-added fluorophores to label a known CMA substrate; b) modifying a cytosolic fluorescent protein with a sequence containing the KFERQ-like motif.

### 5.1 GAPDH-HaloTag

Self-labeling enzyme tags have been an emerging technology that shows many advantages over classical fluorescent proteins for the analysis and imaging of protein-of-interest (POI).<sup>201</sup> This methodology combines the specificity offered by a genetically encoded protein tag and the functional diversity afforded by synthetic chemistry.<sup>202</sup> Among these tags, HaloTag (HT) is a modified haloalkane dehalogenase which can selectively bind to a chloroalkane linker (HT ligand) to form irreversible covalent bond rapidly under physiological conditions.

Seki et al reported a fluorescence-based method based on the HaloTag fused glyceraldehyde-3-phosphate dehydrogenase (GAPDH), a CMA substrate, to evaluate CMA activity at the single cell level.<sup>203</sup> As illustrated in Fig. 13a, the covalent binding between GAPDH-HT and HT ligands can only occur at neutral pH (cytosol and nucleus) but not in the acidic lysosome lumen, providing a possibility for researchers to visualize the translocation of cytosolic GAPDH to lysosomes. By attaching the HT ligand with acid-insensitive fluorophores, such as tetramethylrhodamine (TMR) and Oregon green (OG), the localization of GAPDH-HT can be followed, which was uniformly

distributed over cytoplasm immediately after labeling (Fig. 13b) and exhibited some dot-like clusters after 21 h incubation (Fig. 13b, white arrows). The latter overlaps with LAMP2A signals, indicating the translocation of GAPDH-HT into lysosome (Fig. 13c). CMA-activating stimulations such as long-term serum deprivation, oxidative stress ( $H_2O_2$ ), mycophenolic acid (MPA) and 6-aminonicotinamide treatment were tested in GAPDH-HT expressing HeLa cells or mouse primary cultured Purkinje cells (PCs). Under all these conditions, increased proportion of cells showing dot-like accumulations of GAPDH-HT signals as well as the increased number of dots per cell were observed (Fig. 13d). siRNA-mediated knockdown of LAMP2A lead to not only significant decrease of dot-like accumulation of GAPDH-HT but



**Fig. 13** Monitoring CMA activity by GAPDH-HT. (a) Schematic illustration of the working mechanism of GAPDH-HT. Covalent labeling of fluorophore-conjugated HT ligand (gray circle) to CMA substrate (GAPDH)-HT does not occur in low pH in lysosome and thus enable tracking CMA substrate-HT translocation from cytosol to lysosome. (b) Representative fluorescent images of TMR-labeled GAPDH-HT immediately (0 h, left) and 21 h after labeling (21 h, right) in HeLa cells. Arrows on the right image indicate the cells with dot-like accumulations to indicate active CMA. Scale bar, 20  $\mu$ m. (c) Representative GAPDH-HT fluorescence (left), LAMP2A immunostaining (center) and merged (right) images of HeLa cells 21 h after labeling with TMR-HT ligand. Scale bar, 5  $\mu$ m. (d) Representative fluorescent images of TMR-labeled GAPDH-HT immediately (0 h, left) and 24 h after labeling (24 h, right) with TMR-HT ligand in primary cultured Purkinje cells. Scale bar, 20  $\mu$ m. Reproduced from ref. 203 with permission from PLOS, copyright 2012.

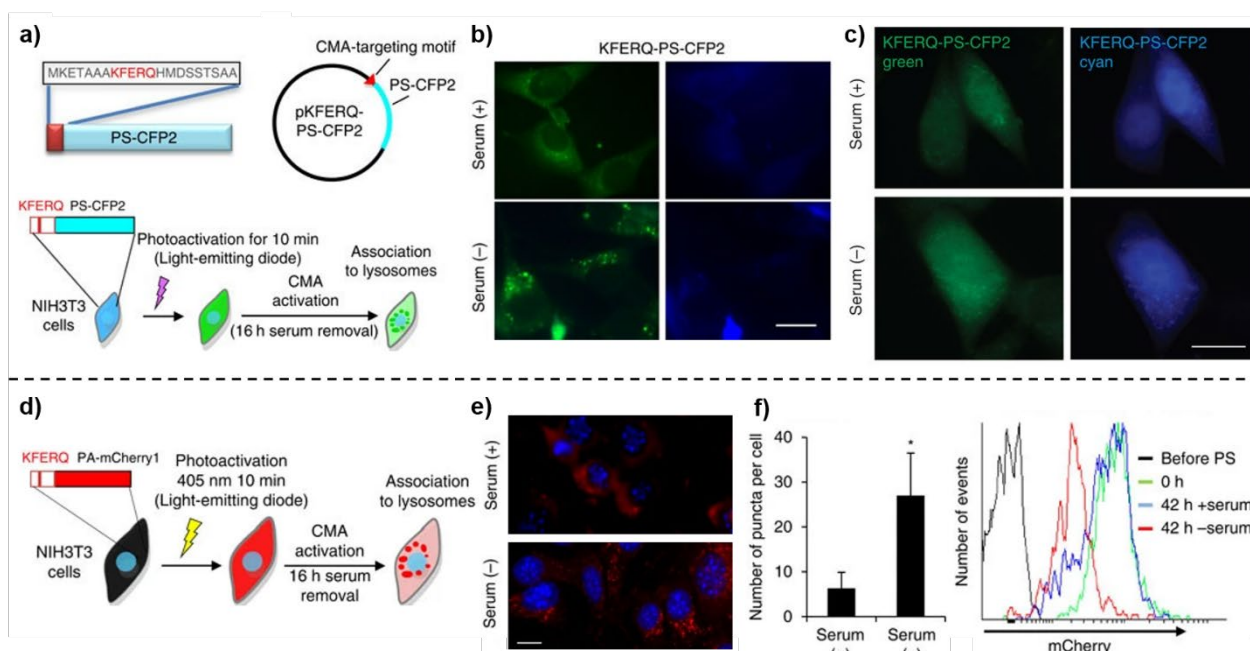
also triggers the enhancement of macroautophagy level as a compensation for maintaining intracellular homeostasis. In the control experiments, treatments of macroautophagic inhibitors, 3-MA and ATG5-siRNA, did not demonstrate any impact on the lysosomal translocation of GAPDH-HT. Plus the finding that immunostaining signals of LC3 and GAPDH-HT exhibited totally separate localization in cells, the relationship between GAPDH-HT signals with CMA but not macroautophagy was verified. Subsequently, GAPDH-HT-based assay was applied to elucidate the CMA function in certain pathogenesis, which might inspire future discovery of novel CMA-targeted therapeutics for disease treatment. Somehow the background signals of this assay are relatively high, as Fig 13 demonstrated, making it impossible to pick the CMA-active lysosomes by naked eye observation. The performance of this assay requires further optimisation to yield a CMA-specific biosensor with higher specificity.

## 5.2 KFERQ tagged fluorescence proteins

Previous biochemical studies have proven that the cargo selectivity of CMA is achieved by the recognition system of HSC70 chaperone towards the KFERQ motif-bearing substrate proteins. Based on this understanding, Cuervo et al have developed a series of photoconvertible fluorescence proteins to measure CMA activity in live cells.<sup>204</sup> This type of fluorescent substrates was constructed by genetically encoding the first 21 amino acids of ribonuclease A (the first protein identified as a CMA substrate) bearing the KFERQ motif, into the N-terminus

of a fluorescent protein. Their first attempt, KFERQ-EGFP, failed owing to the intrinsic characteristics of CMA that the precedent protein unfolding occurs prior to translocation to lysosomes where the EGFP fluorescence will be quenched. In this case, it would be impossible to differentiate the small portion of KFERQ-EGFP that binds to lysosomal membrane, which represents the actual CMA event, from those newly synthesized reporter proteins fluorescing with the same photophysical properties.

To solve this issue, a monomeric cyan fluorescent protein with the photoswitchable property was introduced to construct KFERQ-PS-CFP2. In cells stably expressing KFERQ-PS-CFP2, the existing reporter can be converted to green fluorescent state ( $\lambda_{\text{ex}} = 490 \text{ nm}$ ,  $\lambda_{\text{em}} = 511 \text{ nm}$ ) by 10-min excitation of 405 nm light, which can be well separated from the newly synthesized reporter after the photoconversion with an original cyan fluorescence ( $\lambda_{\text{ex}} = 400 \text{ nm}$ ,  $\lambda_{\text{em}} = 468 \text{ nm}$ ) (Fig. 14a). Upon CMA activation, the distribution of the photoconverted reporter is changed from diffuse to the typical punctate pattern. The degradation of KFERQ-PS-CFP2 in the photoconverted pool, as the decrease of the green fluorescence, can thus be measured at a given timepoint. This approach does not require additional treatment such as inhibiting protein synthesis, blocking lysosomal proteolysis, etc., that may provoke variation of basal CMA level in cell, and thus makes it appealing to evaluate the CMA activity more accurately under normal physiological conditions.

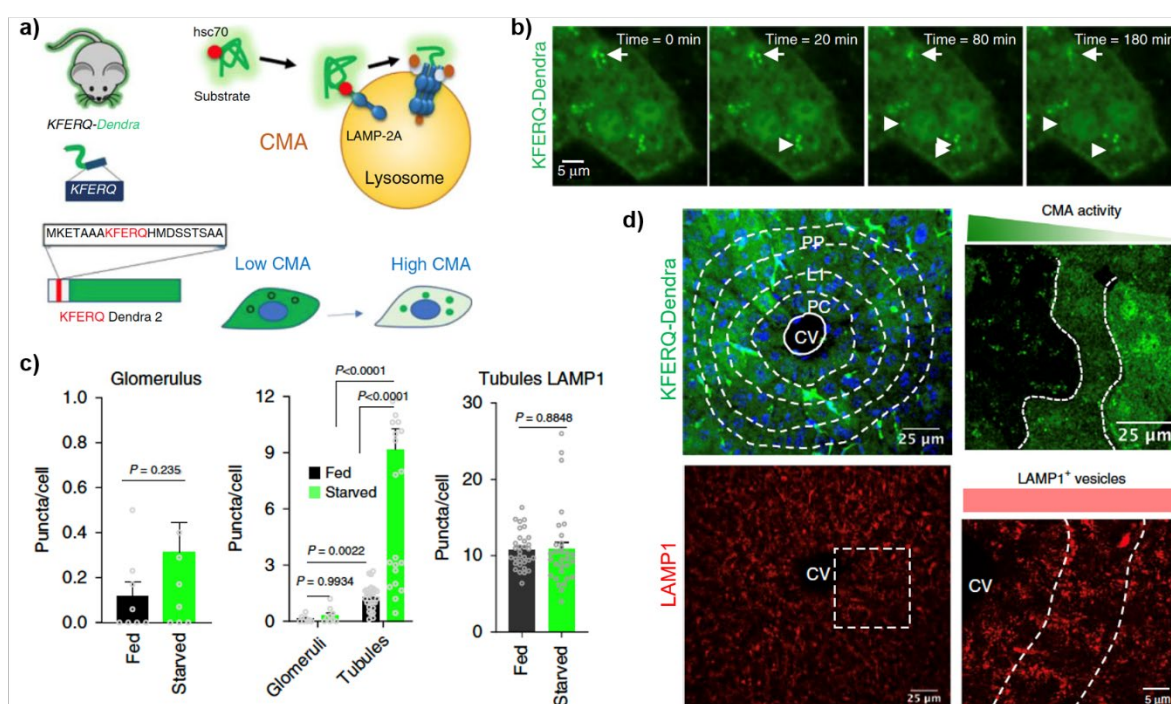


**Fig. 14** KFERQ-photoswitchable protein reporters for monitoring and quantifying CMA in cells. (a) Top: scheme of the insertion of the CMA-targeting motif in PS-CFP2 and map of pKFERQ-PS-CFP2. Bottom: Schematic illustration of the working principle of KFERQ-PS-CFP2 reporter. (b) Images of NIH3T3 cells stably expressing KFERQ-PS-CFP2 after being photoconverted and maintained in media supplemented with (+) or without (-) serum for 16 h. Scale bar, 5  $\mu\text{m}$ . (c) Representative images of LAMP2A-knockdown NIH3T3 cells transfected with KFERQ-PS-CFP2 after being photoconverted and maintained in media supplemented with (+) or without (-) serum. Scale bar, 5  $\mu\text{m}$ . (d) Scheme of the working principle of KFERQ-PA-mCherry1 reporter. (e) Representative images of NIH3T3 cells stably expressing KFERQ-PA-mCherry1 after being photoactivated and maintained in media supplemented with (+) or without (-) serum for 16 h. Nuclei are staining with DAPI (blue). (f) Left: quantification of the number of red fluorescent puncta per cell. Values are mean  $\pm$  s.e. of three different experiments with >20 cells counted per experiment. \* $P=0.001$ , ANOVA-Bonferroni. Scale bars, 5  $\mu\text{m}$ . Right: Representative flow cytometry histogram showing the effect of serum removal for 42 h. PS, photoswitching. Reproduced from ref. 204 with permission from NPG, copyright 2011.

As shown in Fig. 14b in KFERQ-PS-CFP2-expressing mouse fibroblasts (NIH3T3), 10 h serum starvation results in the change of the photoconverted green fluorescence from mostly diffuse pattern under control condition to a punctate pattern (Fig. 14b). The pattern transformation of green fluorescence was not observed in cells transfected with PS-CFP2 due to the lack of appropriate CMA recognition sequence on the reporter protein, or in LAMP2A-knockdown cell line where the active CMA function was blocked (Fig. 14c). Collectively, these results support the specificity of KFERQ-PS-CFP2 to CMA. Moreover, prolonged starvation for a 30 h temporal course results in a gradual increase in the number of puncta per cell and a concomitant faster decay of the green fluorescence intensity, which was coincident with the kinetics of CMA activation described in *in vitro* studies using isolated lysosomes.<sup>205</sup> In contrast, levels of cyan fluorescence restored within 1 h after photoconversion and remained relatively constant in the following time course, indicating that the degraded cyan protein was replenished by *de novo* synthesized protein that exhibited original cyan emission. Next, the preferential association of KFERQ-PS-CFP2 towards CMA-active lysosomes was further verified by positive colocalization between green puncta and lysosomal markers including LysoTracker, LAMP-1, LAMP-2, HSC70-positive acidic vesicles. Whereas there was rare colocalization of KFERQ-PS-CFP2 with LC3, mannose-6-phosphate receptor (CD-M6PR) or Rab5, markers of AVs, late endocytic recycling compartment and early endosomes, respectively. Immunoblotting results further confirmed the high

abundance of KFERQ-PS-CFP2 on both membranes and lumens of isolated lysosomes from cells previously deprived of serum, which were in agreement with the imaging results. In several aspects including imaging and biochemical assays, it was extensively validated that functional CMA activity in cells was indispensable for the translocation of this reporter from cytosol to lysosomes. Besides, KFERQ-PS-CFP2 reported the compensatory upregulation of CMA in response to the blockage of macroautophagy or proteasomal proteolysis, extending the crosstalk of CMA with other proteolytic pathways. Aided by the universal applicability of this reporter across species, comparative quantification of fluorescent puncta unveiled that the basal levels of CMA and the extent of the response of this pathway to serum starvation was cell-type-dependent.

To further prevent the interference from background noise arising from autofluorescence, a variation of this type of CMA reporters, PA-mCherry1, was constructed, which consists of a photoactivable mCherry protein and the KFERQ-bearing motif (Fig. 14d). KFERQ-PA-mCherry1 processes a turn-on emission ( $\lambda_{\text{ex}} = 564 \text{ nm}$ ,  $\lambda_{\text{em}} = 595 \text{ nm}$ ) upon irradiation of 405 nm light and thereby can be used to track CMA activity by forming red fluorescent puncta in the cell (Fig. 14e). The photoactivable effect facilitates high-content imaging and flow cytometry for quantitative analysis of the CMA activity via calculating number of puncta per cell, and to measure CMA flux by estimating fluorescence decrease (Fig. 14f).



**Fig. 15** Monitoring spatiotemporal CMA activity in vivo. (a) KFERQ-Dendra mouse model and the proposed response to CMA. (b) Time-course snapshots of the liver from KFERQ-Dendra mouse showing the dynamic change of CMA lysosomes (arrows). (c) Quantification of CMA as number of fluorescent puncta per cell in sections from kidney in glomerulus (left) or glomerulus compared to tubules (middle) and in LAMP1 staining in tubules (right) in KFERQ-Dendra mice in response to starvation. (d) Top: KFERQ-Dendra mice liver section with delineated sub-zoning in full field (left) or in higher magnification region (right). CV: central vein; L1 PC: layer 1 pericentral; L5 PP: layer 5 periportal. DAPI is shown in blue. Bottom: LAMP1 staining of full field (left) and higher magnification region with delineated zones (right) of liver. Reproduced from ref. 206 with permission from NPG, copyright 2011.

Using the same approach, a transgenic mouse model systemically expressing KFERQ-Dendra CMA reporter was generated by Cuervo et al and its versatility for monitoring cell-type/tissue/organ-specific spatiotemporal changes in response to activations of CMA has been carefully characterized and validated.<sup>206</sup> With the KFERQ-like motif, this reporter can be recognized by Hsc70 and directed to CMA-active lysosomes, forming fluorescent puncta upon CMA activation (Fig. 15a). This dynamic process can be measured in vivo in live animals using techniques like two-photon imaging (Fig. 15b). Interestingly, image-based analysis of tissue context from the KFERQ-Dendra mouse model reveals remarkable differences between CMA in tubules and glomeruli where starvation did not alter the CMA activity in glomerular cells (Fig. 15c). A striking zonal difference in CMA was observed in hepatocytes in the liver whereby CMA activity decreases from the central vein to the portal region with no significant differences in their lysosome numbers (Fig. 15d). These results highlight the utility of this in vivo reporter for studying CMA activity in diseases pathogenesis and susceptibility at the single cell resolution in organs.

Moreover, the comparison of levels of different types of autophagy using this transgenic mouse model with GFP-LC3 mice for macroautophagy evaluation, *mito*-QC or mt-Keima mice for mitophagy monitoring yielded a preliminary understanding of cell and tissue prevalence of each of these autophagy pathways under basal conditions and of their coordination in response to stress. Considering the association between CMA impairment and human diseases<sup>207-210</sup>, this mouse model is anticipated to play a more important role for modulating CMA activity in the course of different diseases and for evaluating the efficiency of therapeutic interventions with future developments of advanced imaging technologies.

Overall, this fluorescent reporter system paves the new way for measurement and visualization of CMA in several models including cell lines, in vivo animal model, fixed tissue sections, organotypic cultures and primary cells isolated from transgenic animals. It represents a vigorous advance in the development of the CMA toolkit. However, several factors such as autofluorescence in untransfected cells, the kinetics of expression, efficiency of photoconversion and even the cell viability after photo-irradiation may affect the experimental analysis, which are highly advised to be included in the pilot assay. Also, it is recommended to confirm that the formation of punctate structures indeed results from the CMA-mediated translocation of the reporter to lysosomes when applying this system. The validation can be achieved by checking the colocalization of the puncta with lysosomes, confirming the dependence of puncta formation with LAMP2A, removing the impact of other pyrolytic activities, and measuring the transcriptional level of the protein reporter. Notably, the change of fluorescent signals of these reporters observed is referred to the binding of the reporters to lysosomal membrane, which is a transient state and cannot be used to present a cumulative readout of CMA effects in a given time frame. Future tools for measuring the cumulative amount of CMA-active lysosomes in cells or demonstrating the

translocation to lysosomal lumen via differing signals will offer new perspectives for CMA studies and be valuable for the expansion of the CMA toolkit.

## 6. Chemical probes for monitoring autophagy

The development of effective protein-based autophagy reporters has largely contributed to autophagy research and boosted the mechanistic understanding of autophagy pathway and its relationship with a variety of human disease. However, protein-based biosensors require transfection to produce genetically modified models, which is non-trivial and thus not always compatible with the system of interest especially in clinical context. A range of small molecules have been developed as the supplement of the autophagic toolbox, which will be introduced in this section. The development of chemical probes for monitoring autophagy is still at the initial stage and the reported approaches are mainly focusing on bulk autophagy and mitophagy. Table 4 summaries the design rationale of small molecule and nanoparticle-based probes which will be introduced with more details in this section. The readout methods are also shown for comparison.

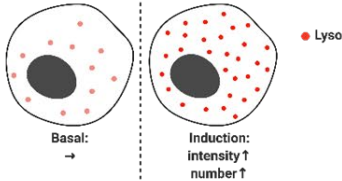
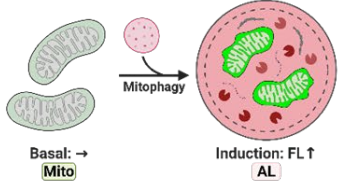
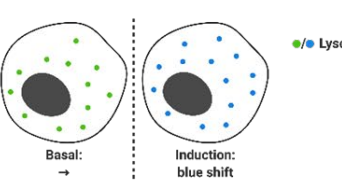
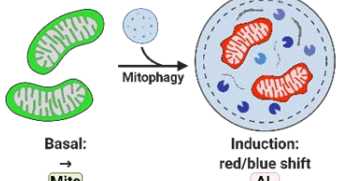
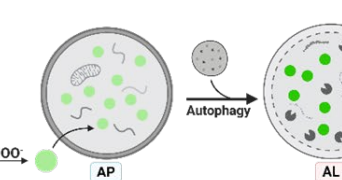
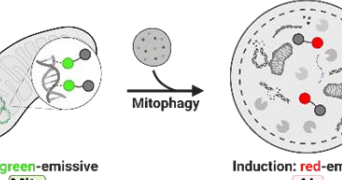
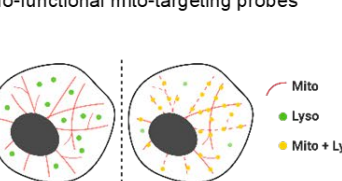
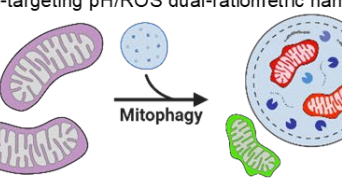
### 6.1 Lysosome-targeting probes

Lysosome plays a vital role in the downstream autophagy execution, which provides an acidic environment and lysosomal hydrolases to finalize the degradation of encapsulated cargoes in autophagosomes. Based on this understanding, lysosome-targeting fluorescent probes would be useful for visualizing the autophagy process (Table 4, Entry a). Two commercially available acidophilic lysosome-targeting dyes, LysoTracker Red DND-99 (LTR) and LysoTracker Green DND-29 (LTG), have both been tested in several autophagy-related models (Fig. 16a).<sup>63, 211-215</sup> These dyes exhibit fluorescence turn-on effect in an acidic environment, due to the removal of intramolecular photoinduced electron transfer (PeT) quenching process by the protonation effect of the weak base units, such as the dimethylamino group. Therefore, as revealed by both image-based and flow cytometry analysis, the fluorescence of these dyes increases along with the increased number of dot-like structures in the cells under the conditions where the level of LC3-II is upregulated (Fig. 16b,c). However, as the fluorescence of this type of sensors can be activated non-selectively by low pH, other acidic granules in the cells such as endosomes or secretory granule might inference with the readout. Fine tuning of the  $pK_a$  will be required to achieve the specificity to lysosomes.

Moreover, the working concentration of conventional lysosome-targeting dyes is normally low to prevent the aggregation-caused quenching (ACQ) effect, which greatly hampers their performance such as photostability in long-term cell tracking. Thereby, Tang et al reported a lysosome-targeting probe with aggregation-induced emission (AIE) property, AIE-LysoY, for tracking autophagy (Fig. 16d).<sup>216</sup> Rationalized by the



**Table 4** Summary of design strategies of chemical probes for monitoring autophagy.

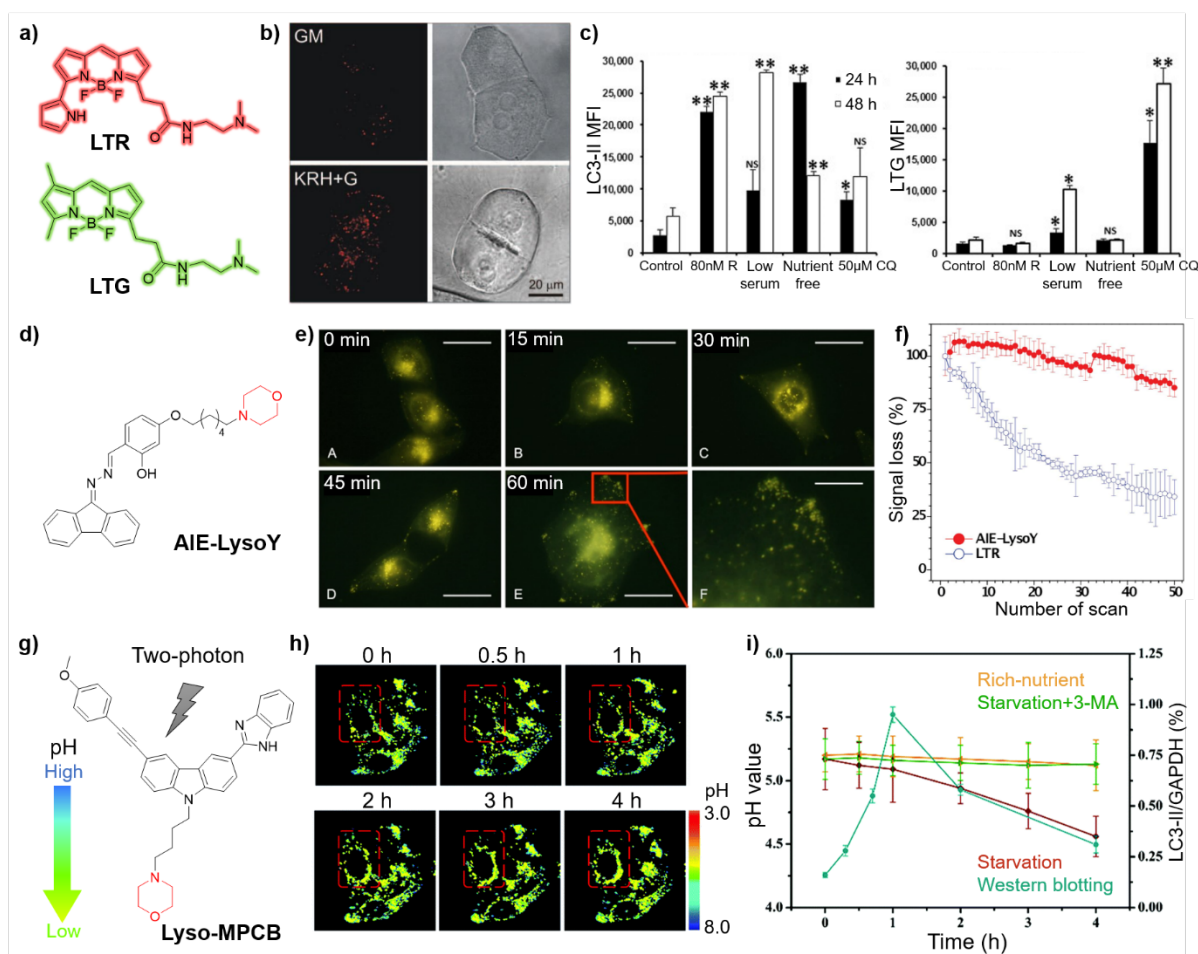
Type	Design strategy	Methods	Type	Design strategy	Methods
Bulk Autophagy	a) (AIE-active) lyso-targeting probes 	In cells: FACS, FM	Mitophagy	e) Mito-targeting light-up/viscosity probes 	In cells: FM
	b) Lyso-targeting ratiometric pH-sensitive probe 	In cells: TP		f) Mito-targeting ratiometric pH-sensitive probe 	In cells: FM
	c) ROS-triggered tandem reaction probe 	In vivo: TP In cells: FM		g) Organelle-redirected nucleic acid sensors 	In cells: FM, TP
Mitophagy	d) Mono-functional mito-targeting probes 	Ex vivo: FACS In cells: FACS, FM		h) Mito-targeting pH/ROS dual-ratiometric nanoprobe 	In cells: FM

**Lyso:** lysosome; **Mito:** mitochondria; **AP:** autophagosome; **AL:** autolysosome; **FM:** fluorescence microscopy; **TP:** two-photon imaging; **FACS:** flow cytometry.

introduction of the morpholine group with moderate alkalinity,<sup>217, 218</sup> AIE-LysoY can be used to visualize lysosomes when excited by the 400–440 nm laser on fluorescence microscopy. With emission peaked at 565 nm, AIE-LysoY processes a large Stokes shift compared to LysoTrackers with BODIPY as the chromophore, which minimizes the self-absorption problem. AIE-LysoY was thus used to follow the change of the number, size and distribution of the lysosome during the time course of rapamycin induced autophagy (Fig. 16e). By virtue of lysosome specificity and improved photostability (Fig. 16f) compared with LTR, AIE-LysoY is capable to provide more insight of lysosomal activities in a long-term experimental setup of autophagy research.

The aforementioned lysosome-targeting probes show fluorescence turn-on effect under low pH. In certain situation, the uneven distribution or uptake of the probe between control cells and stressed cells may complex the quantification. To avoid this issue and better illustrate the autophagy process by using the lysosome-targeting probe, a ratiometric pH fluorescent probe (Table 4, Entry b), Lyso-MPCB (Fig. 16g), was designed and synthesized by Meng et al.<sup>219</sup> By introducing the benzimidazole and morpholine group into *p*-

methoxyphenylacetylene-substituted carbazole, Lyso-MPCB processes a significant emission red shift (from 410 to 475 nm) in response to the pH decrease from 9.6 to 3.2 under the excitation at 370 nm. Adapting two-photon excitation at 760 nm, the fluorescent signals of Lyso-MPCB in cells can be separated into two channels: the blue channel ranged from 400–420 nm and the green channel ranged from 465–485 nm. With pH changing from 3.0 to 8.0, the blue channel ( $I_{blue}$ ) exhibits a continual enhancement accompanying with a gradual decrease of fluorescent intensity in the green channel. The ratio of  $I_{green}/I_{blue}$  obtained from the fluorescence images can thus be converted to the corresponding intracellular pH, which reveals the lysosomal pH fluctuation in cells during the autophagy process stimulated by HBSS starvation (Fig. 16h). The lysosomal pH values at a single time point of autophagy induction can be calculated using this probe. Specifically, a time-course pH change in lysosomes from 5.2 to 4.6 was observed in cells under starvation-induced autophagy, whereas such change did not occur in cells with rich nutrient or co-treated with 3-MA to block autophagy. This variation tendency was coincided with the change of LC3-II level (normalized to GAPDH level) in the



**Fig. 16** Lysosome-targeting small molecule fluorophores for monitoring autophagy. (a) Chemical structures of LTR and LTG. (b) Representative fluorescence (left) and bright-field (right) images of LTR (200 nM, 20 min) stained hepatocytes in growth medium (GM, top panels) or serum-free Krebs-Ringer-HEPES buffer plus glucagon (KRH+G, lower panels). (c) Statistical analysis of median fluorescence intensity (MFI) values of Alexa Fluor647 antibody labeled LC3-II (left) or LTG (right) signals detected in untreated cells and cells treated with 80 nM rapamycin, low serum, nutrient free conditions or 50 μM CQ for 24 or 48 h. Student t tests between control and test cell samples were performed, \*P = <0.05, \*\*P = <0.01, NS – not significant; error bars indicate SEM, n = 3. (d) Chemical structure of AIE-LysoY. (e) Fluorescence images of AIE-LysoY (10 μM, 10 min) stained HeLa cells before and after rapamycin treatment (50 μg/mL) for different periods of time (A–E); enlarged region of interest of panel E shown in panel F. Scale bar, A–E: 30 μm; F: 10 μm. (f) Signal loss (%) of AIE-LysoY fluorescence vs LTR with increasing number of scans. λ<sub>ex</sub> = 405 nm (for AIE-LysoY) and 561 nm (for LTR); λ<sub>em</sub> = 468–696 nm (for AIE-LysoY) and 573–696 nm (for LTR); irradiation time: 7.75 s per scan. (g) The working mechanism and molecular structure of Lyso-MPCB. (h) Time course ratiometric (I<sub>green</sub>/I<sub>blue</sub>) images of Lyso-MPCB (10 μM, 30 min) in MCF-7 cells cultured in HBSS medium. Blue channel λ<sub>em</sub> range: 400–420 nm, green channel λ<sub>em</sub> range: 465–485 nm, two-photon excitation wavelength: λ<sub>ex</sub> = 760 nm. (i) Change in pH values of the time point (0–4 h) under different conditions (Starvation, Rich-nutrient and Starvation + 3-MA) along with expression level of LC3-II/GAPDH under starvation conditions. (b,c) Reproduced from ref. 214 with permission from Taylor & Francis, copyright 2006. (e,f) Reproduced from ref. 216 with permission from John Wiley and Sons, copyright 2016. (h,i) Reproduced from ref. 219 with permission from Royal Society of Chemistry, copyright 2019.

western blotting experiment (Fig. 16i). Based on these results, Lyso-MPCB represents a unique tool with two-photon excitation for measuring lysosomal pH change in real time during the autophagy processes.

Additionally, the combination of monodansylcadaverine (MDC) and lysosomotropic drugs has been used in the early stage of autophagy research for measuring autophagic flux in cultured cells and in non-transgenic animals.<sup>73</sup> However, MDC was originally proposed as a specific autophagosome indicator. It was later on verified to have high affinity to lysosomes, which works similarly as other lysosome probes mentioned above.<sup>72, 86</sup> Although in some cases, the number and acidity of lysosomes are consistent with the extend of cellular autophagy activity, the same conclusion is not always correct in more complicated

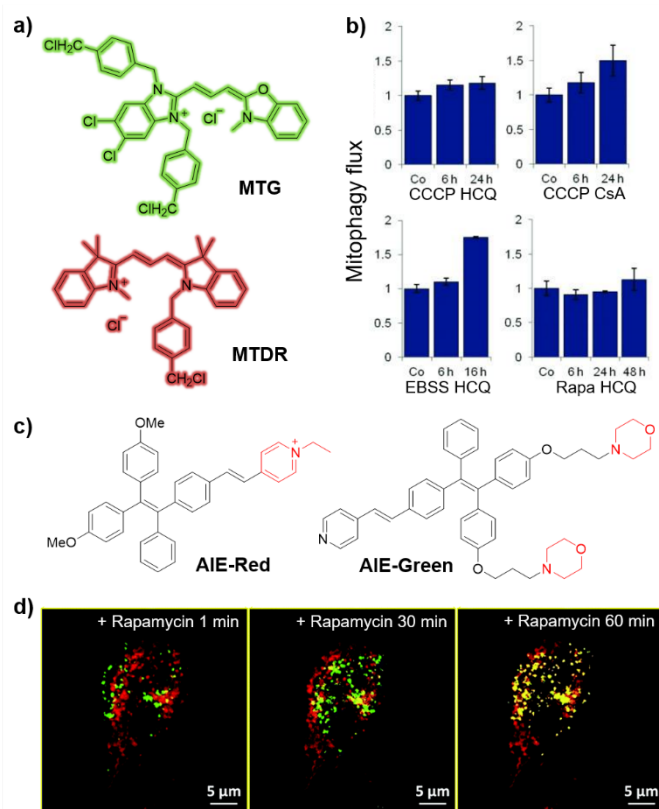
models. Using lysosome-targeting probes alone, technically, is not considered as a precise and acceptable approach for studying cellular autophagy activity by most experts in the field. However, these probes can be useful when combined with other measures of autophagy activity and serve as a supplemental method to support the final conclusion. Some of the examples where LysoTrackers are used can be found in the other sections in this review.

## 6.2 Mitochondria-targeting probes for mitophagy

### 6.2.1 Mono-functional mitochondrial dyes

Mitophagy is a type of selective autophagy, which involves the sequestration of the entire mitochondria by autophagosome

and further fusion with lysosome for degradation. Apart from the previously mentioned protein-based biosensors (Section 4.1), small molecule fluorophores have been developed for mitophagy study. The most straightforward way is to use mitochondria-targeting dyes in combination with lysosome-targeting trackers (Table 4, Entry d). For example, commercially available mitochondria probes, including MitoTracker Deep Red (MTDR) and MitoTracker Green (MTG), have been used together with the LysoTracker or selective inhibitor to monitor mitophagy (Fig. 17a).<sup>214, 220</sup> With this regard, Boya et al raised a new index for determining the mitophagy flux by using flow cytometry. The definition of mitophagy flux, herein, is the ratio of fluorescence intensity of MTDR in the presence of mitophagy and lysosomal inhibitors to that in the absence of those inhibitors, which is further normalized to the corresponding value in control cells.<sup>220</sup> Although this index allows for the direct comparison of mitophagy induced by different treatments in a quantitative manner, parallel experiments using appropriate negative control is always necessary (Fig. 17b).



**Fig 17.** Monitoring and quantifying mitophagy by mitochondria-targeting dyes. (a) Chemical structures of MTG and MTDR. (b) Comparison of mitophagy flux induced by CCCP, EBSS and rapamycin (Rapa) in SH-SY5Y cells in the presence of the indicated inhibitor (HCQ, hydroxychloroquine; CsA, cyclosporin A) at different timepoints. (c) Structures of AIE-Red and AIE-Green. (d) Real-time overlay confocal images of AIE-Red- and AIE-Green-stained HeLa cells after rapamycin (50  $\mu$ g/mL) treatment for indicated time. (b) Reproduced from ref. 220 with permission from Taylor & Francis, copyright 2015. (d) Reproduced from ref. 221 with permission from Royal Society of Chemistry, copyright 2018.

To overcome the previously mentioned ACQ and self-absorption problem encountered by many conventional fluorophores, Liu et al proposed an approach for multicolour

monitoring of mitophagy based on two AIE-active fluorogens, AIE-Red and AIE-Green (Fig. 17c), both with large Stokes shift and excellent photostability, to selectively target mitochondria and lysosomes, respectively.<sup>221</sup> These two dyes can be excited by using a single 405 nm laser to achieve two distinguishable emission colors. Time-lapse confocal imaging of rapamycin treated HeLa cells showed minimal colocalization between the green (500–525 nm) and red (650–700 nm) emission patterns at the beginning of the treatment but better colocalization occurred after 1 h rapamycin incubation (Fig. 17d). This observation was also supported by the change of Pearson correlation coefficient that changed from 0.23 at 1 min to 0.46 at 60 min time point, indicating the activation and enhancement of mitophagy upon rapamycin treatment. Multiplexed cellular organelle imaging can thus be conducted by combining two organelle-specific probes with separate spectra to facilitate the visualization of the mitophagy process with a simple experimental setup.

A wide diversity of AIE-active probes with different spectral characteristics for subcellular organelle targeting have been developed, which will provide more options for imaging and monitoring biological processes. Other AIE fluorogens with mitochondrial specificity have also been explored as mitophagy probes in various models, which includes TPE-Py-NCS reported by Tang et al<sup>222</sup>, a series of Ir (III) complexes<sup>223</sup> and so on.

### 6.2.2 pH-sensitive mitochondria-targeting probes

To monitor autophagy, using the aforementioned mono-functional mitochondria-targeting probes requires the use of lysosome-targeting reporters at the same time to follow the translocation of the mitochondria with lysosomes. To simplify the process, pH-sensitive mitochondria-targeting probes have been developed, which can report the change of mitochondrial pH as the result of mitophagy activation (Table 4, Entry e). Kim et al reported a system, probe **1**, consisting of three key moieties: 1) a piperazine-linked naphthalimide as the fluorescence turn-on unit upon acidification with  $pK_a$  of  $\sim 6.2$ , 2) a cationic triphenylphosphonium group for mitochondrial targeting, and 3) a reactive benzyl chloride subunit for immobilization on biomacromolecules to facilitate long-term tracking even after acidification or membrane depolarization (Fig. 18a).<sup>224</sup> In HeLa cells cultured in serum-free medium containing pepstatin A, a lysosomal protease inhibitor used for delaying mitochondrial degradation in autolysosomes, stronger fluorescent intensity of probe **1** was observed with larger overlapping with LTR signals when compared with intact cells (Fig. 18b). The Pearson's correlation coefficient of probe **1** and LTR increased from 0.85 to 0.91 during the starvation process, which could not be observed in intact cells. By combining with the pH-insensitive MitoTracker Red, the mitochondrial pH can be determined by using the ratiometric method.

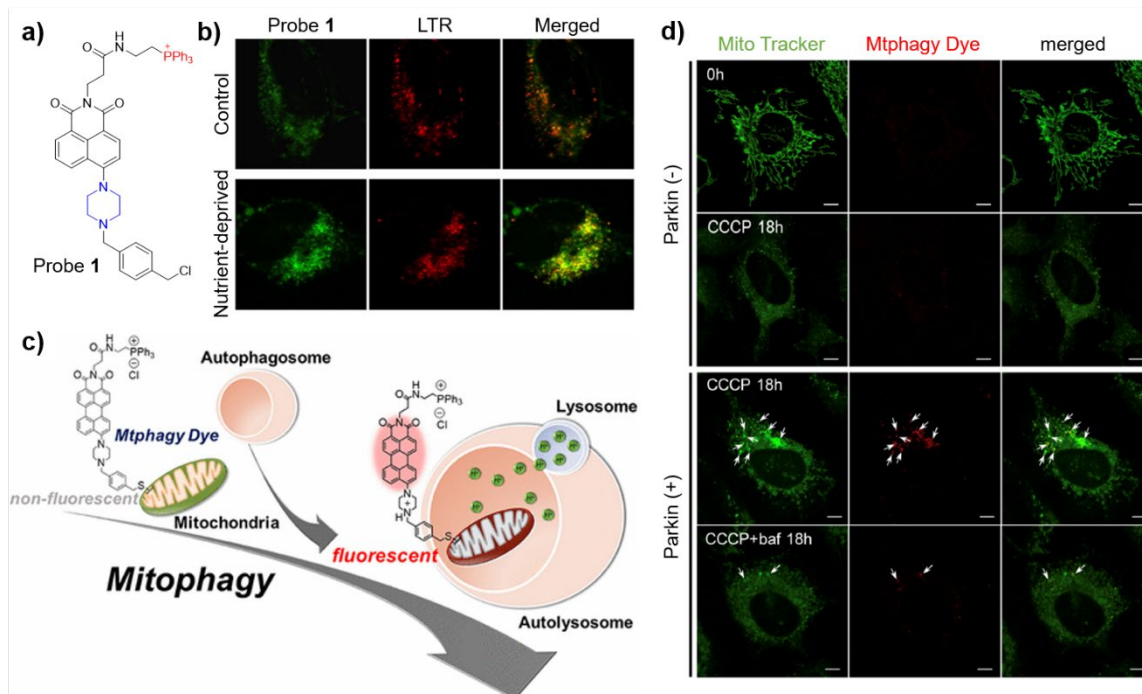
With the promising results gained from probe **1**, a red-shifted version with extended  $\pi$ -conjugated system, Mtpagy Dye, were reported by Iwashita and co-workers (Fig. 18c). Based on the same working mechanism as probe **1**, Mtpagy Dye has been demonstrated to be a reliable pH indicator for detecting mitophagic phenomena in a wide range of cell lines.<sup>225</sup> Mtpagy

Dye displayed very weak fluorescence in normal HeLa cells (Parkin(-)) but showed red-emissive puncta with Parkin-expressed HeLa cells (Parkin(+)) (Fig. 18d). Parkin is an E3 ligase enzyme known to mediate ubiquitin signalling to promote mitophagy. With the additional bafilomycin A1 to block the acidification, the red emission cannot be observed in Parkin(+) cells.

To further improve the quantification of the pH-sensitive mitochondrial probes, Tan et al developed a ratiometric cyanine-based fluorescent probe, HQO (Fig. 19a), which can simultaneously detect mitochondria and lysosomes, and thus is highly specific for mitochondria-containing autolysosomes.<sup>226</sup> In vitro experiments have proven that HQO is protonated to form HQOH<sup>+</sup> and HQOH<sub>2</sub><sup>2+</sup> in low pH buffers. The transition from HQO to HQOH<sup>+</sup> results in a giant redshift of the absorption and emission maximum from 530/650 nm to 710/750 nm. In LoVo cells and MCF-7 cells, HQO selectively accumulates in mitochondria and exhibits strong fluorescence upon 559 nm excitation, whereas the signal from the channel excited by 635 nm, which indicates the location of HQOH<sup>+</sup>, is very dim under in control condition. Costaining with GFP-LC3A suggested that HQO can be engulfed into mitophagosomes along with the damaged mitochondria, whereas no colocalization between GFP-LC3A and HQOH<sup>+</sup> can be observed. This is consistent with the instability of GFP in the acidic autolysosome as previously reported.<sup>71</sup> The fluorescence of HQOH<sup>+</sup> was found to largely overlap with a small portion of lysosome areas by using LysoTracker Blue or GFP-LAMP1 but still within the regions of high density mitochondria (Fig. 19b), indicating that HQOH<sup>+</sup> may

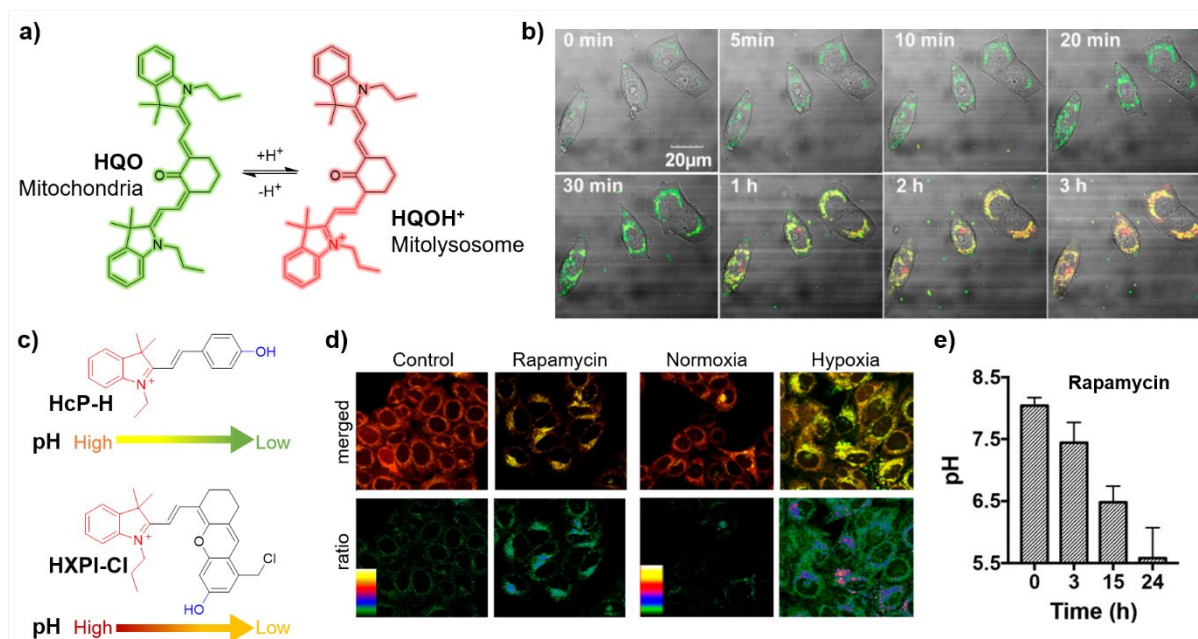
be able to specifically target autolysosomes derived from mitophagy. Subsequently, Bafilomycin A1 is employed to block the acidification of lysosomes, whereby HQOH<sup>+</sup> fluorescence became much weaker than that in untreated cells under mitophagy condition. Time-lapse confocal imaging of MCF-7 cells incubated with HQO in serum-free medium revealed that HQO only fluoresced at the beginning of the treatment, mainly accumulated in the mitochondrial area, while fluorescent signals of HQOH<sup>+</sup> was gradually intensified during the treatment period until finally colocalize with all HQO stained regions, perfectly demonstrating the overall mitophagy process in live cells, thanks to the protonation-induced ratiometric fluorescence from a simply one-step staining.

Similar design strategy was applied in a series of hemicyanine-based pH sensors, among which HcP-H<sup>227</sup> and HXPI-Cl<sup>228</sup> are two of the most recently reported probes used for detecting the mitochondrial pH variation during mitophagy. Different from HQO, emission spectra of these two dyes experience a blue-shift upon acidification (Table 4, Entry f; Fig. 19c). Both dyes exhibit a dual-emission response according to the intracellular mitochondrial pH environment. Taken HXPI-Cl as an example, the mitochondrial pH change can be simply analysed by merged or ratio images of HXPI-Cl signals collected from green (emission ranged from 655-685 nm) and red (emission ranged from 695-725 nm) channels with a single excitation wavelength at 635 nm. During the rapamycin/hypoxia-induced mitophagy, significant color change (from red to yellow) was observed, accompanying with



**Fig. 18** Acidification turn-on mitochondria probes for visualizing mitophagy. (a) Structure of probe 1. (b) Confocal images of HeLa cells stained with probe 1 (5.0  $\mu$ M, 5 h) and LTR in growth medium (control) or in serum-free KRH buffer containing pepstatin A (nutrient-deprived cells). Probe 1:  $\lambda_{\text{ex}}$  = 488 nm; emission filters at 510–550 nm. (c) Illustration of the working mechanism of Mtpagy Dye. (d) Parkin-dependent mitophagy induced by CCCP (10  $\mu$ M) revealed by confocal images of normal and Parkin-expressed HeLa cells with or without bafilomycin A1 treatment stained by Mtpagy Dye (0.1  $\mu$ M). Scale bar: 10  $\mu$ m. (b) Reproduced from ref. 224 with permission from American Chemical Society, copyright 2014. (c,d) Reproduced from ref. 225 with permission from American Chemical Society, copyright 2017.





**Fig. 19** Protonation-induced ratiometric measurement of mitophagy in cells. (a) Transition and translocation between HQO and HQOH<sup>+</sup>. (b) Real-time confocal imaging of MCF-7 cells incubated with HQO (20  $\mu$ M) in serum-free medium. All pictures are overlaid images of optical images and fluorescence images excited at 559 and 635 nm. (c) Structures and pH sensing of HcP-H and HXPI-Cl. (d) Merged green ( $\lambda_{em}$  = 655–685 nm) and red ( $\lambda_{em}$  = 695–725 nm) fluorescence images of HeLa cells pre-treated by HXPI-Cl (5.0  $\mu$ M, 5 h) during the rapamycin (left) /hypoxia (1% O<sub>2</sub>; right) induced mitophagy. Scale bar, 10  $\mu$ m. (e) Quantification of mitochondrial pH change during rapamycin treatment in different incubation time. (b) Reproduced from ref. 226 with permission from American Chemical Society, copyright 2016. (d,e) Reproduced from ref. 228 with permission from American Chemical Society, copyright 2019.

less mitochondria-like tubular structure in extended stress timeframes (Fig. 19d). By fitting the  $I_{green}/I_{red}$  ratio to the calibration curve of intracellular pH, the corresponding time-dependent mitochondrial pH change in the process of mitophagy can be determined (Fig. 19e), which demonstrated a graduate acidification process of mitochondria during mitophagy.

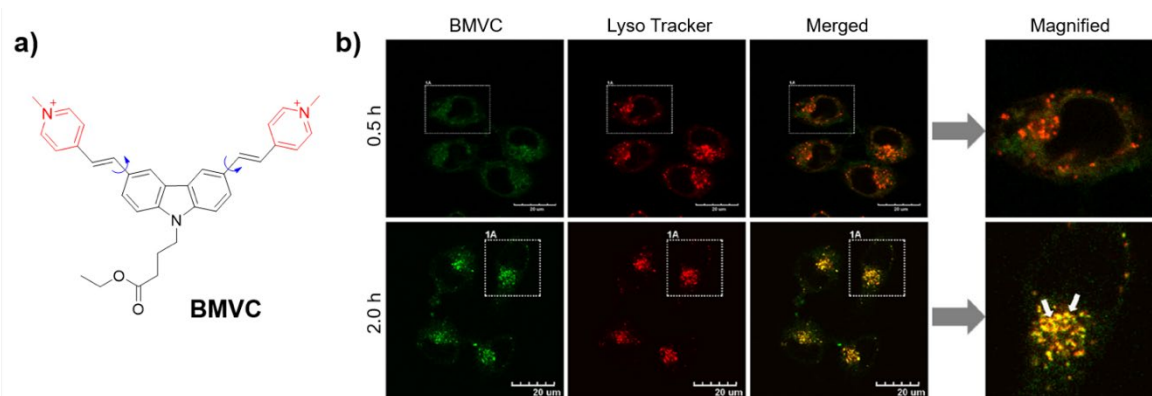
Another similar example was reported by Yu et al.<sup>229</sup> In general, it is acceptable that such pH-sensitive ratiometric probes are useful for real-time monitoring of cellular mitophagy process. The advantages of this type of probes include simple to use, good sensitivity, with internal reference, and thus represent promising small molecule tools for mitophagy study with the possibility of quantitative analysis.

### 6.2.3 Mitophagy-specific viscosity sensitive probes

In addition to mitochondrial pH change, other microenvironment factors such as viscosity can also be altered during mitophagy (Table 4, Entry e). Yang et al. reported a mitochondria-anchored fluorescent viscosimeter, BMVC, and explored its application in visualizing the dynamic change of viscosity during mitophagy (Fig. 20a).<sup>230</sup> BMVC contains two cationic and lipophilic 1-methyl-4-vinylpyridium components, serving both as rotor units and mitochondrial anchor. As a molecular rotor, the free rotation of the C-C bond in BMVC would be hindered when the local viscosity increases, resulting in a linear relationship between the fluorescence intensity and the viscosity in the range from 17.96 to 168.6 cP. Subsequently, the mitochondria specificity and response to intracellular

viscosity change were investigated. Notably, with the aid of BMVC, a gradual increase of mitochondrial viscosity was observed when the damaged mitochondria are fused with lysosomes into autolysosomes during mitophagy. An example is shown in Fig. 20b, where dim and dispersed signals of BMVC exhibited a dramatic enhancement in starved HeLa cells. With the expanding degree of mitophagy, the BMVC fluorescence was considerably colocalized with lysosomes, which, on the contrary, cannot be observed in CQ-treated cells. These results indicate the potential of using mitochondrial viscosity as a parameter to follow the fusion of the lysosomes and the mitochondria-entrapped autophagosomes, which could provide new perspective for mitophagy-related fundamental and clinical investigations. However, the mitochondria-anchoring property of BMVC is dependent on the mitochondria-membrane potential. The changes of membrane potential need to be taken into account when interpreting the analysis using this type of probes.

Apart from viscosity, the large negative membrane potential is the unique feature of mitochondria among all the organelles. Han et al. developed two dual-color mitochondrial-membrane potential responsive probes, RC-TPP<sup>231</sup> and RC-AMI<sup>232</sup>, both containing a Rhodamine-lactam that turns on the red fluorescent in acidic environment when proton triggers the opening of the spiro-lactam, a potential responsive linker, and a “always-on” blue-emissive coumarin. Similarly, when the mitochondria lose the large membrane potential, these molecules escape from the mitochondria and translocate to other compartments in the cells where lysosomes with low pH



**Fig. 20** Measuring mitochondrial viscosity change during mitophagy. (a) Structure of BMVC. (b) Fluorescence images of HeLa cell incubated with BMVC (4  $\mu$ M) and LTR in serum-free medium for 0.5 and 2.0 h. BMVC:  $\lambda_{\text{ex}}$  = 488 nm. Scale bar, 20  $\mu$ m. (b) Reproduced from ref. 230 with permission from American Chemical Society, copyright 2019.

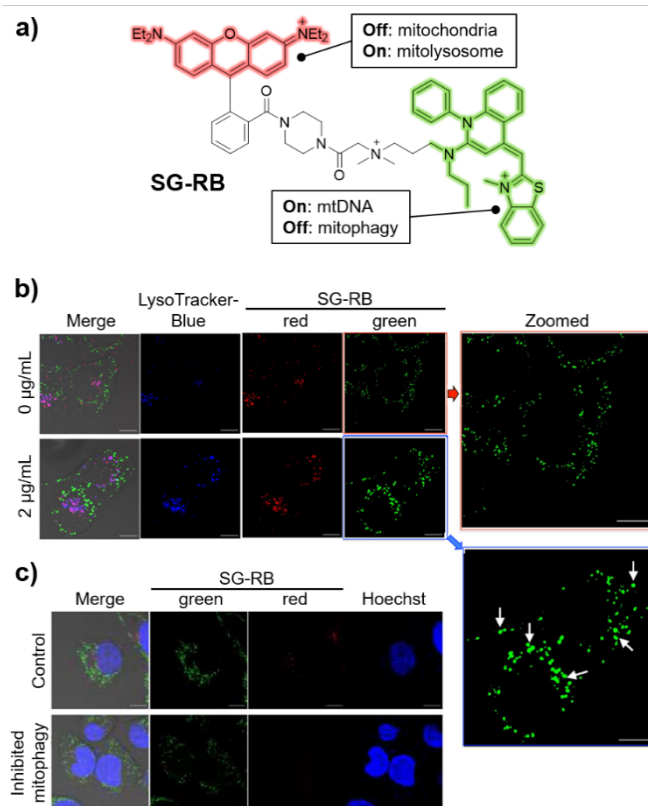
activate their red emission. Therefore, they used this method to confirm the depolarized mitochondria in the conditions that enhance mitophagy. However, as mitochondrial depolarization is a pathologically relevant event that can be triggered by diverse cellular activities, these two probes are thus not specific for monitoring autophagy pathway.

#### 6.2.4 Tracking mitochondrial nucleic acid for mitophagy

Mitochondria not only play a vital role in cellular energy provision, but also contain their own genetic materials.<sup>233</sup> These genetic materials, including both DNA and RNA, in mitochondria are essential for normal mitochondrial function and even cellular viability. Changes in the structures or levels of mitochondrial genome are associated with various types of health conditions.<sup>234–236</sup> On the other hand, as a major target of many disease models, the functions of autophagy in terms of genome regulating have not yet been systematically studied.<sup>237</sup> In this regard, monitoring mitochondrial nucleic acid could be used as a novel approach for probing mitophagy as well as provide a new perspective for pathology studies (Table 4, Entry g).

Han et al. reported a dual-functional fluorescent probe, SG-RB, integrating a red-emissive rhodamine B (RB) entity for mitochondria targeting and a fluorogenic SYBR Green-I (SG) entity for DNA sensing, for detecting mitochondrial DNA (mtDNA) and tracking the delivery of mitochondria into lysosomes in mitophagy (Fig. 21a).<sup>238</sup> At lower dye concentration (0.1–2.0  $\mu$ M), SG-RB selectively binds to mtDNA with the green SG fluorescence exclusively in mitochondria, while at higher concentration, excess SG-RB accumulates within nuclear DNA (nuDNA) after reaching the full capacity of mtDNA. In CCCP-pretreated cells, SG-RB not long accumulates in the mitochondria and mainly in nucleus, suggesting the selectivity to mtDNA is mediated by the negative transmembrane potentials of mitochondria. Interestingly, the RB signal was largely diminished in SG-RB/mtDNA, which they attributed to the physical contact of SG-RB with complex mitochondrial nucleoids that contain diverse proteins. Next, when cells

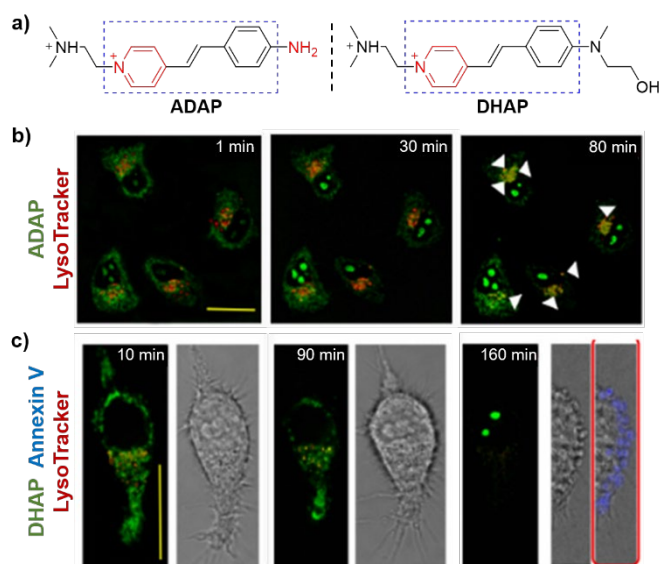
executed mitophagy under prolonged basal and Bafilomycin A1/doxorubicin-stressed conditions, SG-RB restored red RB fluorescence together with the loss of green SG fluorescence upon mitophagic delivery of SG-RB/mtDNA into lysosomes (Fig. 21b,c). Aided with the distinct dual-color imaging of SG-RB/mtDNA in mitochondria over lysosomes, this approach offers a unique tool to assessing mtDNA in mitophagy to unwind the interplay of mtDNA, mitophagy and diverse pathological orders.



**Fig. 21** Tracking mtDNA in mitophagy. (a) Chemical structure of SG-RB. (b) Confocal microscopy images of HeLa cells pre-treated with SG-RB (1  $\mu$ M, 30 min) under control condition (0  $\mu$ g/mL) or during doxorubicin-induced mitophagy (2

$\mu\text{g/mL}$ ). (c) Confocal microscopy imaging of SG-RB/Hoechst co-stained HeLa cells in DMEM supplemented with (control) or without bafilomycin A1 to inhibit mitophagy. Red:  $\lambda_{\text{ex}} = 561 \text{ nm}$ ,  $\lambda_{\text{em}} = 570\text{--}625 \text{ nm}$ ; green,  $\lambda_{\text{ex}} = 488 \text{ nm}$ ,  $\lambda_{\text{em}} = 499\text{--}553 \text{ nm}$ . Scale bars,  $10 \mu\text{m}$ . (b,c) Reproduced from ref. 238 with permission from American Chemical Society, copyright 2019.

The similar molecular design was adopted by Zhou et al to construct a series of RNA-targeted probes, which were applied for the exploration of spatiotemporal coordination among organelles during autophagy process using two-photon imaging.<sup>239</sup> In Zhou's work, the styrylpyridine salt scaffold, functioning for both mitochondrial targeting and groove insertion with RNA, was modified with different substitutions to achieve distinctive permeability into nucleoli. Both probes, ADAP and DHAP, can achieve an "off-on" two-photon fluorescence response towards RNA. Under normal condition, these two probes anchor mitochondria and interact with mitochondrial RNA, exhibiting two-photon emission. However, the location of these two probes changes from the mitochondria in control cells to lysosomes along with dysfunctional mitochondria under mild oxidation ( $\text{H}_2\text{O}_2$ )-induced autophagy. Interestingly, the introduction of amino group enables the probe ADAP to translocate from eliminated mitochondria to nucleus by binding to the nuclear pore complexes (NPCs) and then stain nucleoli RNA, highlighting the dynamic characters of autophagy. On the contrary, after the intact amino moiety was substituted by 2-(methylamino) ethanol unit, the resultant probe, DHAP, can only penetrate through nuclear membrane when cell apoptosis occurs. The advanced version of this series – a RNA-specific photosensitizer was also developed by the same group, which was used as both stressor and imaging agent to demonstrate how cells struggle in the balance of autophagy (survival) and apoptosis (death) as results of mitochondrial damage.<sup>240</sup>

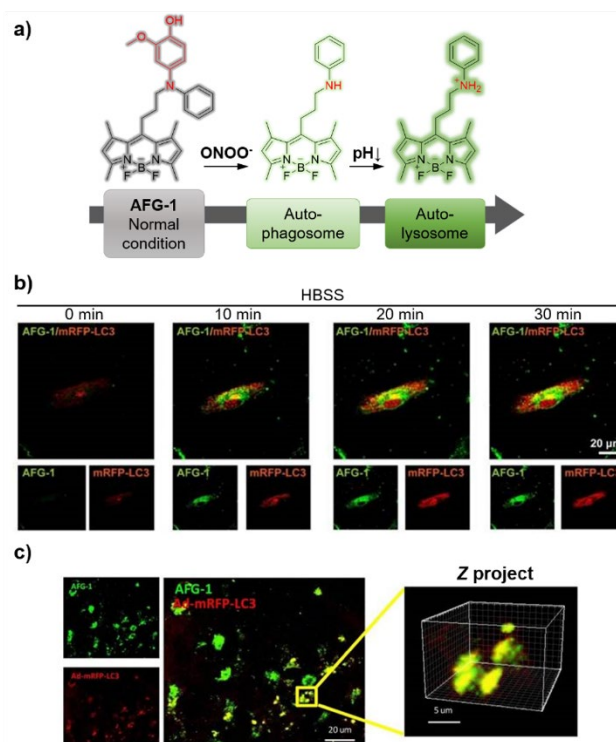


**Fig. 22** Tracking spatiotemporal coordination among organelles during autophagy by mitochondrial RNA probes. (a) Chemical structures of ADAP and DHAP. (b) TP confocal fluorescence images of live HeLa cells treated with  $\text{H}_2\text{O}_2$  ( $20 \mu\text{M}$ , 1–80 min) after staining by ADAP ( $10 \mu\text{M}$ , 30 min) and Lysosome-Tracker Deep Red, ADAP:  $\lambda_{\text{ex}} = 860 \text{ nm}$ ,  $\lambda_{\text{em}} = 550\text{--}600 \text{ nm}$ . (c) Confocal fluorescence images of live HeLa cells treated with  $\text{H}_2\text{O}_2$  ( $20 \mu\text{M}$ , 10–160 min) after stained by DHAP ( $10 \mu\text{M}$ , 30 min), Lysosome-Tracker Deep Red, and Annexin V (as the apoptosis indicator).

DHAP:  $\lambda_{\text{ex}} = 880 \text{ nm}$ ,  $\lambda_{\text{em}} = 570\text{--}620 \text{ nm}$ . Scale bars,  $20 \mu\text{m}$ . (b,c) Reproduced from ref. 239 with permission from American Chemical Society, copyright 2019.

### 6.3 ROS-triggered autophagy probes

Autophagy, in another aspect, is considered as a potential protective mechanism that contributes to cell resilience to environmentally induced oxidative stress. It has been found in some models that autophagy boosts "cellular housekeeping" through promoting the removal of reactive oxygen species (ROS)-damaged proteins and organelles, minimizing accumulation of potentially harmful species to reduce cell stress.<sup>241</sup> Furthermore, the overproduction of mitochondria-generated ROS can serve as the cell signalling molecules for triggering autophagy under various conditions.<sup>242, 243</sup> As such, targeting ROS could provide a new angle for probing autophagy (Table 4, Entry c).



**Fig. 23**  $\text{ONOO}^-$  initiated autophagy probe. (a) Molecular structure of AFG-1 and the proposed tandem reaction-based mechanism for autophagy monitoring. (b) Representative confocal images of AFG-1 and mRFP-LC3 puncta at indicated timeframe in HBSS-treated live endothelial cells. (c) Z-project data of in vivo two-photon fluorescence imaging for the colocalization of AFG-1 and the adenovirus-mRFP-LC3 in the ischemia brain, 150–200  $\mu\text{m}$  below the cortical surface was selected for imaging. AFG-1,  $\lambda_{\text{ex}} = 495\text{--}500 \text{ nm}$ ; mRFP,  $\lambda_{\text{em}} = 575\text{--}645 \text{ nm}$ ; two-photon  $\lambda_{\text{ex}} = 800 \text{ nm}$ . (b,c) Reproduced from ref. 244 with permission from Ivyspring International Publisher, copyright 2019.

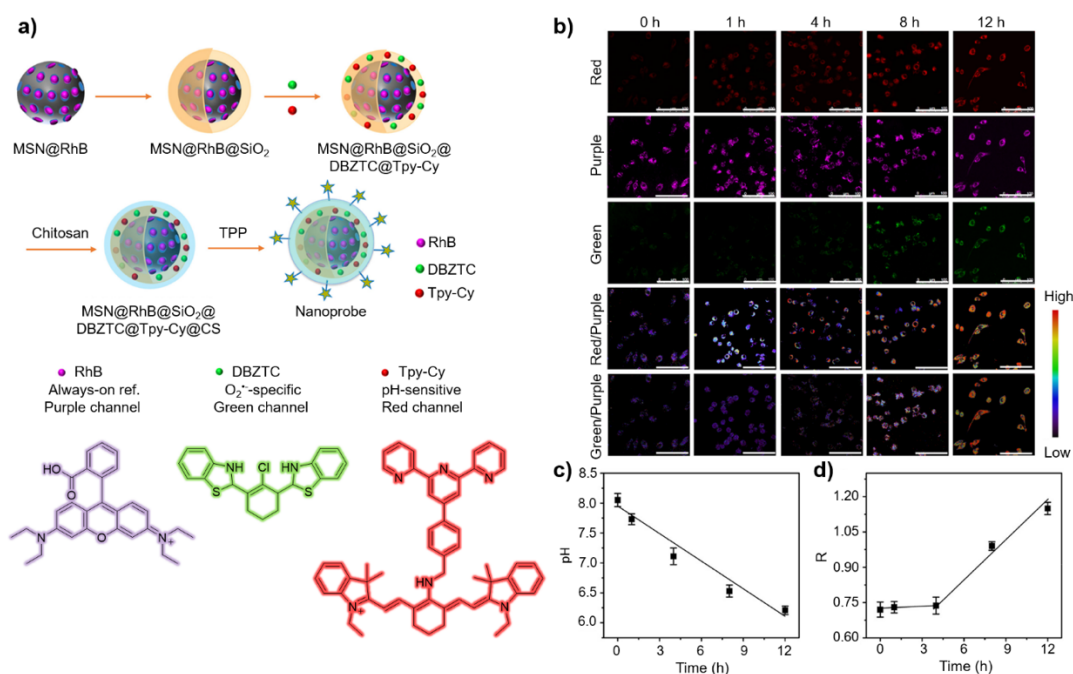
One of the most typical examples is a peroxyxynitrite ( $\text{ONOO}^-$ )-sensitive probe, AFG-1, recently reported by Han et al. AFG-1 incorporates a well-tailored *o*-methoxyphenol moiety as a fluorescence quencher, which can be cleaved by  $\text{ONOO}^-$  to yield a fluorescent aniline, into the BODIPY fluorophore block.<sup>244</sup> At the early stage of autophagy, endogenous  $\text{ONOO}^-$ , one of the nitrosative stress markers, triggers the oxidative dearylation



reaction and transforms the diphenylamines of AFG-1 to aniline that is more acidotropic, switching on its fluorescence. As the autophagic process proceeds, the daughter probe containing unsubstituted phenylamino group can be engulfed into the autophagosomes and delivered into autolysosomes where it can be protonated and thus cause a further fluorescence enhancement (Fig. 22a).

In the endothelial cells subjected to HBSS treatment, the AFG-1 fluorescence increased gradually with the continuous nutrient starvation and was found to co-exist with that of mRFP-LC3 (Fig. 22b), demonstrating the capability of AFG-1 for tracing the cellular autophagy process. The feasibility of AFG-1 to monitor the autophagy process was further verified by using several genetic and pharmacological autophagic interventions, including *Atg5* knockdown and 3-MA treatment to block autophagosome formation, and Bafilomycin A1 treatment to inhibit the fusion between autophagosomes and lysosomes. Noteworthy, combined with in vivo two-photon laser scanning microscopy, the elevation of local autophagy vacuoles in neurovascular components of living mice after photothrombosis-induced brain ischemia can be visualized by strong AFG-1 fluorescence signals, which well colocalized with the adenovirus-mRFP-LC3 staining (Fig. 22c). The excellent performance of AFG-1 in live mice provides the direct in vivo observation on ONOO<sup>-</sup>-initiated autophagy activation upon ischemia injury. Due to its sensitivity and the easy operation, AFG-1 represents a powerful imaging tool to explore autophagy-related biology under a variety of pathological contexts both in vitro and in vivo.

On the other hand, Tang et al reported a dual-ratiometric fluorescent nanoprobe for quantitatively monitoring the dynamic process of superoxide anion ( $O_2^{\bullet-}$ ) and pH changes differentiatingly in live cells (Table 4, Entry h).<sup>245</sup> This core-shell structure-based nanoprobe was constructed by using the rhodamine B (RhB) loaded mesoporous silica nanoparticle (MSN) as the core, with the outer  $SiO_2$  shell doping with  $O_2^{\bullet-}$ -specific DBZTC and pH-sensitive Tpy-Cy, and the surface functionalized with mitochondria targeting triphenylphosphonium (TPP) (Fig. 23a). Utilizing the environmentally stable RhB as the reference, the nanoprobe is able to selectively target mitochondria and simultaneously measure kinetic constants of pH (Red/Purple channel) and  $O_2^{\bullet-}$  (Green/Purple channel) by dual-ratiometric imaging in HeLa cells. Results in Fig. 23b indicated that  $O_2^{\bullet-}$  remained unchanged and the mitochondrial pH value decreased in the early stage of starvation-triggered autophagy, followed by the increase of  $O_2^{\bullet-}$  at the later stage. In addition, Zhu et al developed multi-functionalized gold@silver nanoprobe for real-time detection of in situ  $O_2^{\bullet-}$  during the entire autophagy process.<sup>246</sup> Several interesting findings were pointed out according to their results: a) intracellular  $O_2^{\bullet-}$  level controlled the autophagy process by mediating the autolysosome generation; b) different starvation conditions can induce different autophagy processes, such as diverse transition time to reach steady state. The proposed methods will enlighten more and more potentials in studying the key role of ROS in autophagy or exploring novel approaches to regulate autophagy for disease treatment.



**Fig. 24** Dual-ratiometric fluorescent nanoprobe for quantifying  $O_2^{\bullet-}$  and pH changes during autophagy. (a) Illustration of the composition and formation of the nanoprobe. (b) Fluorescence ratiometric images of nanoprobe (0.2 mg/mL)-incubated HeLa cells treated by GP-starvation for different time periods. Scale bars, 100  $\mu$ m. (c) The pH of HeLa cells treated by GP-starvation for different time periods. (d) The ratio values ( $R = F_{\text{Green}}/F_{\text{Purple}}$ ) of HeLa cells treated by GP-starvation for different time periods. Reproduced from ref. 245 with permission from American Chemical Society, copyright 2017.



## 7. Conclusion and prospective

Decades of research has linked autophagy with various fundamental cellular functional networks. As a powerful programme for intracellular garbage disposal and recycling, autophagy features characteristic cytoprotective and druggable properties and is increasingly getting attention owing to its therapeutic potential in cancer and other diseases. Despite that autophagy currently enjoys star status in cell biology, the establishment of related methodological system is far from complete. Unbiased re-evaluations and further expansion of the existing autophagy toolkit are still in demand to further uncover diverse and challenging aspects in the field. Readers may notice that only fluorescence-based assays for bulk autophagy, mitophagy, aggrephagy and CMA are included in this review, as there is rare fluorescent monitoring approach for other subtypes of autophagy presented in the past reports. In particular, although chemical probes possess several properties that can be used to overcome intrinsic shortcoming of protein markers, such as the complexity and heterogeneity of transfection, the development of chemical probes is still in the early stage and thus is barely applied in the frontline of biomedical studies. Based on our understanding, there are still challenges and perhaps future opportunities to further advance the autophagy toolkit for real-world applications. We summarize a few points as follows:

### 1. Autophagy and other organelles

Apart from autophagosome and lysosome, which directly take part in autophagy activities, other organelles also have inextricable connections with this pathway. First, it is widely agreed that ER-Golgi associated compartments and endocytosis are implicated in membrane contribution to phagophore formation.<sup>247-250</sup> Particularly, ER membrane contributes to the initiation of autophagosome through the formation of omegasomes.<sup>251</sup> Also, in endosomal microautophagy, cytosolic proteins are trapped in vesicles generated at the surface of late endosomes through the assembly of endosomal sorting complexes required for transport (ESCRT).<sup>185</sup> Moreover, some behaviours of lipid droplets are ascribed to the intracellular autophagy activities<sup>252, 253</sup> and the molecular mechanisms behind this remains not fully understood. Hence, tools that can be used to uncover the roles and interactions of different organelles in autophagy activities are urgently needed and may play a crucial part for the crosstalk between autophagy and other cellular pathways.

### 2. Current limitations and future potential of chemical probes

As illustrated in this review, it seems like that the utility and applicability of chemical probes are nowhere near as noticeable as protein-based biosensors, which is worth provoking reflective thinking to give the future amelioration of probe designs. There are several reasons that may explain why this is the case. First, most chemical probes were concluded as the autophagy indicators by simply using several

types of autophagic modulators to alter cellular autophagy activities. Some of them even lack of verification by autophagic inhibitors, which, undoubtedly, fails to be convincing in biological studies. In this regard, standard criteria for experimental verifications of a novel autophagy probe should be established to avoid misconception and development of several protein-based biosensors can be used for reference. Next, methods for quantitation of autophagy regulation are extremely important for biomedical research, whereas most of chemical probes were only demonstrated as qualitative tools for visualizing certain changes during autophagy. Moreover, because of inadequate specificity, chemical probes sometimes may require extra restrictions to better functionate.

Those limitations have greatly hampered the usage of existing chemical probes of autophagy in real-world application. However, numerous instinct advantages of chemical probes make it promising for researchers to develop next generation of autophagy indicators. Small molecules can be easily modified to achieve good cell permeability, by which no transfection is required. The intensity and distribution of fluorescence tagged protein markers sometimes may differ due to the uneven expression levels, while using chemical probes can directly tackle this issue. Aided by some anchoring groups or peptide sequences, the specificity of chemical probes can also be improved to some extent. Generally, there are great potential of chemical probes in this field awaiting for future exploration.

### 3. Dual-function fluorescent probes in autophagy

Recently, several dual-function small molecule probes for autophagy-related research have been developed. Zhao et al develop two type I photosensitizers based on phosphindole oxide, which can selectively accumulate in a neutral lipid region in cells and induce ER-stress mediated apoptosis and autophagy by photodynamic therapy (PDT).<sup>254</sup> Besides, Zhang et al synthesized a series of pyridinium-substituted tetraphenylethylene salts that can serve as mitochondria trackers as well as mitophagy modulators for cancer therapy.<sup>255</sup> These approaches highlight the demand of fluorescent chemicals that exhibit multiple functionalities – serving as imaging agents, autophagy modulators, and may also take part in other physiological functions.

### 4. Autophagy-targeting chimeras (AUTACs)

Unlike starvation-induced bulk autophagy, the selectivity of xenophagy relies on receptor proteins such as SQSTM1, which link selective cargoes and nascent autophagosomes through the LC3-interacting ubiquitination.<sup>256-258</sup> Arimoto et al firstly demonstrated S-guanylation, one of protein post-translational modifications (PTMs), on the endogenous nucleotide 8-nitroguanosine 3',5'-cyclic monophosphate (8-nitro-cGMP) of invading cytoplasmic group A streptococci is involved in bacteria-cell recognition for autophagy.<sup>259</sup> As a standalone tag that destines substrates for selective autophagic clearance, S-guanylation was then used by the same group as a chemical tool to construct autophagy-

targeting chimeras (AUTACs) for targeted protein degradation.<sup>260</sup> AUTACs can be utilized as linkages between specific disease-related targets (proteins, fragmented mitochondria) and autophagosomes, providing a new strategy for targeted degradation of pathogens. Aided by the fluorescent labelling, the turnover of those proteins and mitochondria in lysosomes can be monitored by using microscopy imaging, achieving the combination of drug delivery and therapy visualization. How to exploit the S-guanine tag to design and construct more robust tools for selective autophagy remains further consideration.

#### 5. LIR motif

In addition to S-guanylations tag, other selective mechanism of macroautophagy processes involves the specific interaction of Atg8 protein and cargo receptor molecules on the nascent autophagosomal membrane via short peptide motifs called LC3-interacting regions (LIRs).<sup>261, 262</sup> The exploration of the LIR database provides potential instructions for probe constructions and is expected to lead future expansion of the autophagy toolbox.

#### 6. Other cargo-specific types of autophagy.

Like we mentioned before, there is a lack of fluorescence-based tools for microautophagy and other cargo-specific subtypes of autophagy, including pexophagy, xenophagy, ER-phagy, lipophagy, ferritinophagy and glycophyagy. Remarkably, in a series of studies unearthing the molecular machinery of ER-phagy and ribophagy, numerous selective receptors or markers were identified and well characterised.<sup>263-266</sup> Being conjugated with Keima protein or other fluorescence proteins, they were also used as tools for studying selective forms of autophagy.<sup>264, 267</sup> There is no doubt that in-depth studies of these areas will certainly accelerate the development and expansion of autophagy toolkit.

#### 7. Relationship between oxidative stress and autophagy

Interestingly, most forms of autophagy, including bulk autophagy, reflect the response of cells towards direct or indirect oxidative damage.<sup>268, 269</sup> Pexophagy is a typical case in point.<sup>270, 271</sup> Autophagy also functions to clear intracellular oxidised proteins. Contextually, studies of probes that can specifically target oxidised products in cells should yield valuable conclusions and offer some insights for probing these cargo-specific types of autophagy.

In summary, we present the advantages, limitations, and future directions for fluorescence-based autophagy tools, which are still at the growing stage for cell biology studies. Although much effort and rigour are still required to fulfil the systematic investigation of the autophagy toolkit, we believe that both protein marker-based assays and synthetic chemical probes could provide new opportunities to study this fundamental pathway. Through this review, we look forward to stimulating collaborative research interests from both chemical and biological fields to develop advanced strategies to reinforce the autophagy toolkit.

## Conflicts of interest

There are no conflicts to declare.

## Acknowledgements

We thank Australian Research Council (DE170100058) and Australia-China Science and Research Fund-Joint Research Centre on Personal Health Technologies for the financial support.

## Notes and references

1. P. Ravanan, I. F. Srikumar and P. Talwar, *Life Sci*, 2017, **188**, 53-67.
2. C. Masclaux-Daubresse, Q. Chen and M. Have, *Curr Opin Plant Biol*, 2017, **39**, 8-17.
3. H. Martini-Stoica, Y. Xu, A. Ballabio and H. Zheng, *Trends Neurosci*, 2016, **39**, 221-234.
4. B. Levine and G. Kroemer, *Cell*, 2008, **132**, 27-42.
5. V. Deretic, T. Saitoh and S. Akira, *Nat Rev Immunol*, 2013, **13**, 722-737.
6. T. Iida, K. Onodera and H. Nakase, *World J Gastroenterol*, 2017, **23**, 1944-1953.
7. N. S. Katheder, R. Khezri, F. O'Farrell, S. W. Schultz, A. Jain, M. M. Rahman, K. O. Schink, T. A. Theodossiou, T. Johansen, G. Juhasz, D. Bilder, A. Brech, H. Stenmark and T. E. Rusten, *Nature*, 2017, **541**, 417-420.
8. J. M. Mulcahy Levy and A. Thorburn, *Cell Death Differ*, 2020, **27**, 843-857.
9. D. Mijaljica, M. Prescott and R. J. Devenish, *Autophagy*, 2011, **7**, 673-682.
10. W. W. Li, J. Li and J. K. Bao, *Cell Mol Life Sci*, 2012, **69**, 1125-1136.
11. S. Kaushik and A. M. Cuervo, *Nat Rev Mol Cell Biol*, 2018, **19**, 365-381.
12. Y. Feng, D. He, Z. Yao and D. J. Klionsky, *Cell Res*, 2014, **24**, 24-41.
13. B. Ravikumar, M. Futter, L. Jahreiss, V. I. Korolchuk, M. Lichtenberg, S. Luo, D. C. Massey, F. M. Menzies, U. Narayanan, M. Renna, M. Jimenez-Sanchez, S. Sarkar, B. Underwood, A. Winslow and D. C. Rubinshtein, *J Cell Sci*, 2009, **122**, 1707-1711.
14. R. K. Amaravadi, A. C. Kimmelman and J. Debnath, *Cancer Discov*, 2019, **9**, 1167-1181.
15. S. Sudarsanam and D. E. Johnson, *Curr Opin Drug Discov Devel*, 2010, **13**, 31-40.
16. C. H. Jung, S. H. Ro, J. Cao, N. M. Otto and D. H. Kim, *FEBS Lett*, 2010, **584**, 1287-1295.
17. Y. Y. Chang, G. Juhasz, P. Goraksha-Hicks, A. M. Arsham, D. R. Mallin, L. K. Muller and T. P. Neufeld, *Biochem Soc Trans*, 2009, **37**, 232-236.
18. G. Herrero-Martin, M. Hoyer-Hansen, C. Garcia-Garcia, C. Fumarola, T. Farkas, A. Lopez-Rivas and M. Jaattela, *EMBO J*, 2009, **28**, 677-685.
19. D. Meley, C. Bauvy, J. H. Houben-Weerts, P. F. Dubbelhuis, M. T. Helmond, P. Codogno and A. J. Meijer, *J Biol Chem*, 2006, **281**, 34870-34879.
20. J. Kim, M. Kundu, B. Viollet and K. L. Guan, *Nat Cell Biol*, 2011, **13**, 132-141.

21. S. F. Funderburk, Q. J. Wang and Z. Yue, *Trends Cell Biol*, 2010, **20**, 355-362.
22. R. Kang, H. J. Zeh, M. T. Lotze and D. Tang, *Cell Death Differ*, 2011, **18**, 571-580.
23. Y. Wei, M. Liu, X. Li, J. Liu and H. Li, *Biomed Res Int*, 2018, **2018**, 1012789.
24. A. C. Nascimbeni, P. Codogno and E. Morel, *FEBS J*, 2017, **284**, 1267-1278.
25. L. W. Brier, L. Ge, G. Stjepanovic, A. M. Thelen, J. H. Hurley and R. Schekman, *Mol Biol Cell*, 2019, **30**, 1098-1107.
26. Y. Ichimura, T. Kirisako, T. Takao, Y. Satomi, Y. Shimonishi, N. Ishihara, N. Mizushima, I. Tanida, E. Kominami, M. Ohsumi, T. Noda and Y. Ohsumi, *Nature*, 2000, **408**, 488-492.
27. H. Nakatogawa, Y. Ichimura and Y. Ohsumi, *Cell*, 2007, **130**, 165-178.
28. B. Ravikumar, K. Moreau, L. Jahreiss, C. Puri and D. C. Rubinsztajn, *Nat Cell Biol*, 2010, **12**, 747-757.
29. M. Walczak and S. Martens, *Autophagy*, 2013, **9**, 424-425.
30. L. Thukral, D. Sengupta, A. Ramkumar, D. Murthy, N. Agrawal and R. S. Gokhale, *Biophys J*, 2015, **109**, 2067-2078.
31. T. Kirisako, Y. Ichimura, H. Okada, Y. Kabeya, N. Mizushima, T. Yoshimori, M. Ohsumi, T. Takao, T. Noda and Y. Ohsumi, *J Cell Biol*, 2000, **151**, 263-276.
32. P. Wild, D. G. McEwan and I. Dikic, *J Cell Sci*, 2014, **127**, 3-9.
33. T. Lamark, S. Svenning and T. Johansen, *Essays Biochem*, 2017, **61**, 609-624.
34. K. R. Parzych and D. J. Klionsky, *Antioxid Redox Signal*, 2014, **20**, 460-473.
35. L. Yu, Y. Chen and S. A. Tooze, *Autophagy*, 2018, **14**, 207-215.
36. S. Jawhari, M. H. Ratinaud and M. Verdier, *Cell Death Dis*, 2016, **7**, e2434.
37. J. Yang, R. Zhou and Z. Ma, *Adv Exp Med Biol*, 2019, **1206**, 329-357.
38. S. Song, J. Tan, Y. Miao and Q. Zhang, *J Cell Physiol*, 2018, **233**, 3867-3874.
39. W. S. Lee, W. H. Yoo and H. J. Chae, *Curr Mol Med*, 2015, **15**, 735-745.
40. S. Ko, M. J. Gu, C. G. Kim, Y. C. Kye, Y. Lim, J. E. Lee, B. C. Park, H. Chu, S. H. Han and C. H. Yun, *Antiviral Res*, 2017, **146**, 86-95.
41. F. Hua, K. Li, S. Shang, F. Wang and Z. Hu, *Adv Exp Med Biol*, 2019, **1206**, 551-593.
42. Y. Choi, J. W. Bowman and J. U. Jung, *Nat Rev Microbiol*, 2018, **16**, 341-354.
43. S. Dolai, T. Liang, A. I. Orabi, D. Holmyard, L. Xie, D. Greitzer-Antes, Y. Kang, H. Xie, T. A. Javed, P. P. Lam, D. C. Rubin, P. Thorn and H. Y. Gaisano, *Gastroenterology*, 2018, **154**, 1805-1821 e1805.
44. A. S. Gukovskaya, I. Gukovsky, H. Algul and A. Habtezion, *Gastroenterology*, 2017, **153**, 1212-1226.
45. J. Mialet-Perez and C. Vindis, *Essays Biochem*, 2017, **61**, 721-732.
46. Y. T. Wu, H. L. Tan, G. Shui, C. Bauvy, Q. Huang, M. R. Wenk, C. N. Ong, P. Codogno and H. M. Shen, *J Biol Chem*, 2010, **285**, 10850-10861.
47. D. J. Klionsky, K. Abdelmohsen, A. Abe, M. J. Abedin, H. Abeliovich, A. Acevedo Arozana, H. Adachi, C. M. Adams, P. D. Adams, K. Adeli, P. J. Adhihetty, S. G. Adler, G. Agam, R. Agarwal, M. K. Aghi, M. Agnello, P. Agostinis, P. V. Aguilar, J. Aguirre-Ghisso, E. M. Airolidi, et al., *Autophagy*, 2016, **12**, 1-222.
48. G. Kroemer and B. Levine, *Nat Rev Mol Cell Biol*, 2008, **9**, 1004-1010.
49. N. Mizushima, T. Yoshimori and B. Levine, *Cell*, 2010, **140**, 313-326.
50. E. L. Eskelinen, F. Reggiori, M. Baba, A. L. Kovacs and P. O. Seglen, *Autophagy*, 2011, **7**, 935-956.
51. S. J. Kang and W. J. Rhee, *Int J Mol Sci*, 2019, **20**.
52. D. Cui, D. Sun, X. Wang, L. Yi, E. Kulikowicz, M. Reyes, J. Zhu, Z. J. Yang, W. Jiang and R. C. Koehler, *Cell Death Dis*, 2017, **8**, e2919.
53. X. Zeng and C. R. Carlin, *J Virol*, 2013, **87**, 2307-2319.
54. T. Zhang, C. Wolfe, A. Pierle, K. A. Welle, J. R. Hryhorenko and S. Ghaemmamghami, *Proc Natl Acad Sci U S A*, 2017, **114**, E10329-E10338.
55. S. H. Oh, Y. B. Choi, J. H. Kim, C. C. Weihl and J. S. Ju, *Anal Biochem*, 2017, **530**, 57-67.
56. J. Hemelaar, V. S. Lelyveld, B. M. Kessler and H. L. Ploegh, *J Biol Chem*, 2003, **278**, 51841-51850.
57. R. Scherz-Shouval, Y. Sagiv, H. Shorer and Z. Elazar, *J Biol Chem*, 2003, **278**, 14053-14058.
58. Y. Kabeya, N. Mizushima, A. Yamamoto, S. Oshitani-Okamoto, Y. Ohsumi and T. Yoshimori, *J Cell Sci*, 2004, **117**, 2805-2812.
59. Y. Kabeya, N. Mizushima, T. Ueno, A. Yamamoto, T. Kirisako, T. Noda, E. Kominami, Y. Ohsumi and T. Yoshimori, *EMBO J*, 2000, **19**, 5720-5728.
60. I. H. Lee, L. Cao, R. Mostoslavsky, D. B. Lombard, J. Liu, N. E. Bruns, M. Tsokos, F. W. Alt and T. Finkel, *Proc Natl Acad Sci U S A*, 2008, **105**, 3374-3379.
61. D. S. Leeman, K. Hebestreit, T. Ruetz, A. E. Webb, A. McKay, E. A. Pollina, B. W. Dulken, X. Zhao, R. W. Yeo, T. T. Ho, S. Mahmoudi, K. Devarajan, E. Passegue, T. A. Rando, J. Frydman and A. Brunet, *Science*, 2018, **359**, 1277-1283.
62. P. Rockenfeller, M. Koska, F. Pietrocola, N. Minois, O. Knittelfelder, V. Sica, J. Franz, D. Carmona-Gutierrez, G. Kroemer and F. Madeo, *Cell Death Differ*, 2015, **22**, 499-508.
63. G. Warnes, *Methods*, 2015, **82**, 21-28.
64. J. Zhou, S. H. Tan, V. Nicolas, C. Bauvy, N. D. Yang, J. Zhang, Y. Xue, P. Codogno and H. M. Shen, *Cell Res*, 2013, **23**, 508-523.
65. S. Jung, S. Choe, H. Woo, H. Jeong, H. K. An, H. Moon, H. Y. Ryu, B. K. Yeo, Y. W. Lee, H. Choi, J. Y. Mun, W. Sun, H. K. Choe, E. K. Kim and S. W. Yu, *Autophagy*, 2020, **16**, 512-530.
66. X. Chen, Y. Hu, W. Zhang, K. Chen, J. Hu, X. Li, L. Liang, X. Cai, J. Hu, K. Wang, A. Huang and N. Tang, *Free Radic Biol Med*, 2019, **131**, 225-236.
67. K. Kucharewicz, M. Dudkowska, A. Zawadzka, M. Ogronnik, A. A. Szczepankiewicz, Z. Czarnocki and E. Sikora, *Cell Death Dis*, 2018, **9**, 353.
68. A. Tamura and N. Yui, *J Biol Chem*, 2015, **290**, 9442-9454.
69. W. P. Flavin, L. Bousset, Z. C. Green, Y. Chu, S. Skarpathiotis, M. J. Chaney, J. H. Kordower, R. Melki and E. M. Campbell, *Acta Neuropathol*, 2017, **134**, 629-653.
70. L. Jahreiss, F. M. Menzies and D. C. Rubinsztajn, *Traffic*, 2008, **9**, 574-587.
71. S. Kimura, T. Noda and T. Yoshimori, *Autophagy*, 2007, **3**, 452-460.
72. N. Mizushima, A. Yamamoto, M. Matsui, T. Yoshimori and Y. Ohsumi, *Mol Biol Cell*, 2004, **15**, 1101-1111.
73. E. Iwai-Kanai, H. Yuan, C. Huang, M. R. Sayen, C. N. Perry-Garza, L. Kim and R. A. Gottlieb, *Autophagy*, 2008, **4**, 322-329.

74. H. Zhu, P. Tannous, J. L. Johnstone, Y. Kong, J. M. Shelton, J. A. Richardson, V. Le, B. Levine, B. A. Rothmel and J. A. Hill, *J Clin Invest*, 2007, **117**, 1782-1793.
75. J. Haspel, R. S. Shaik, E. Ifedigbo, K. Nakahira, T. Dolinay, J. A. Englert and A. M. Choi, *Autophagy*, 2011, **7**, 629-642.
76. T. E. Rusten, K. Lindmo, G. Juhasz, M. Sass, P. O. Seglen, A. Brech and H. Stenmark, *Dev Cell*, 2004, **7**, 179-192.
77. R. C. Scott, O. Schuldiner and T. P. Neufeld, *Dev Cell*, 2004, **7**, 167-178.
78. A. Melendez, Z. Tallozy, M. Seaman, E. L. Eskelinen, D. H. Hall and B. Levine, *Science*, 2003, **301**, 1387-1391.
79. K. Yoshimoto, Y. Jikumar, Y. Kamiya, M. Kusano, C. Consonni, R. Panstruga, Y. Ohsumi and K. Shirasu, *Plant Cell*, 2009, **21**, 2914-2927.
80. H. J. Maier, E. M. Cottam, P. Stevenson-Leggett, J. A. Wilkinson, C. J. Harte, T. Wileman and P. Britton, *Autophagy*, 2013, **9**, 496-509.
81. C. He, C. R. Bartholomew, W. Zhou and D. J. Klionsky, *Autophagy*, 2009, **5**, 520-526.
82. A. du Toit, J. S. Hofmeyr, T. J. Gniadek and B. Loos, *Autophagy*, 2018, **14**, 1060-1071.
83. A. Kuma, M. Matsui and N. Mizushima, *Autophagy*, 2007, **3**, 323-328.
84. I. Tanida, T. Ueno and E. Kominami, *Methods Mol Biol*, 2008, **445**, 77-88.
85. K. E. Eng, M. D. Panas, G. B. Karlsson Hedestam and G. M. McInerney, *Autophagy*, 2010, **6**, 634-641.
86. E. T. Bampton, C. G. Goemans, D. Niranjana, N. Mizushima and A. M. Tolkovsky, *Autophagy*, 2005, **1**, 23-36.
87. H. Katayama, A. Yamamoto, N. Mizushima, T. Yoshimori and A. Miyawaki, *Cell Struct Funct*, 2008, **33**, 1-12.
88. A. B. Blazquez, E. Escribano-Romero, T. Merino-Ramos, J. C. Saiz and M. A. Martin-Acebes, *PLoS Negl Trop Dis*, 2013, **7**, e2509.
89. T. Y. Lin, H. H. Chan, S. H. Chen, S. Sarvagalla, P. S. Chen, M. S. Coumar, S. M. Cheng, Y. C. Chang, C. H. Lin, E. Leung and C. H. A. Cheung, *Autophagy*, 2020, **16**, 1296-1313.
90. H. Zhuang, F. Wu, W. Wei, Y. Dang, B. Yang, X. Ma, F. Han and Y. Li, *Cell Death Dis*, 2019, **10**, 192.
91. K. Sakamoto, T. Ozaki, Y. C. Ko, C. F. Tsai, Y. Gong, M. Morozumi, Y. Ishikawa, K. Uchimura, S. Nadeana, H. Kitagawa, M. M. L. Zulueta, A. Bandaru, J. I. Tamura, S. C. Hung and K. Kadomatsu, *Nat Chem Biol*, 2019, **15**, 699-709.
92. J. M. Gump and A. Thorburn, *Autophagy*, 2014, **10**, 1327-1334.
93. P. Hundeshagen, A. Hamacher-Brady, R. Eils and N. R. Brady, *BMC Biol*, 2011, **9**, 38.
94. S. Matus, V. Valenzuela and C. Hetz, *Autophagy*, 2014, **10**, 710-714.
95. K. Castillo, V. Valenzuela, S. Matus, M. Nassif, M. Onate, Y. Fuentealba, G. Encina, T. Irrazabal, G. Parsons, F. A. Court, B. L. Schneider, D. Armentano and C. Hetz, *Cell Death Dis*, 2013, **4**, e917.
96. L. Li, Z. V. Wang, J. A. Hill and F. Lin, *J Am Soc Nephrol*, 2014, **25**, 305-315.
97. M. A. Gurney, C. Huang, J. M. Ramil, N. Ravindran, A. M. Andres, J. Sin, P. J. Linton and R. A. Gottlieb, *Methods Mol Biol*, 2015, **1219**, 187-197.
98. J. S. Ju, A. S. Varadhachary, S. E. Miller and C. C. Weihl, *Autophagy*, 2010, **6**, 929-935.
99. L. Esteban-Martinez and P. Boya, *Methods*, 2015, **75**, 79-86.
100. C. Zhou, W. Zhong, J. Zhou, F. Sheng, Z. Fang, Y. Wei, Y. Chen, X. Deng, B. Xia and J. Lin, *Autophagy*, 2012, **8**, 1215-1226.
101. G. Maulucci, M. Chiarpotto, M. Papi, D. Samengo, G. Pani and M. De Spirito, *Autophagy*, 2015, **11**, 1905-1916.
102. B. Loos, A. du Toit and J. H. Hofmeyr, *Autophagy*, 2014, **10**, 2087-2096.
103. T. Kaizuka, H. Morishita, Y. Hama, S. Tsukamoto, T. Matsui, Y. Toyota, A. Kodama, T. Ishihara, T. Mizushima and N. Mizushima, *Mol Cell*, 2016, **64**, 835-849.
104. I. Tanida, T. Ueno and E. Kominami, *Int J Biochem Cell Biol*, 2004, **36**, 2503-2518.
105. A. Kuma, M. Komatsu and N. Mizushima, *Autophagy*, 2017, **13**, 1619-1628.
106. C. J. Rosado, D. Mijaljica, I. Hatzinisiouri, M. Prescott and R. J. Devenish, *Autophagy*, 2008, **4**, 205-213.
107. H. Katayama, T. Kogure, N. Mizushima, T. Yoshimori and A. Miyawaki, *Chem Biol*, 2011, **18**, 1042-1052.
108. Y. Nishida, S. Arakawa, K. Fujitani, H. Yamaguchi, T. Mizuta, T. Kanaseki, M. Komatsu, K. Otsu, Y. Tsujimoto and S. Shimizu, *Nature*, 2009, **461**, 654-658.
109. H. Katayama, H. Hama, K. Nagasawa, H. Kurokawa, M. Sugiyama, R. Ando, M. Funata, N. Yoshida, M. Homma, T. Nishimura, M. Takahashi, Y. Ishida, H. Hioki, Y. Tsujihata and A. Miyawaki, *Cell*, 2020, **181**, 1176-1187 e1116.
110. C. M. Hale, Q. Cheng, D. Ortuno, M. Huang, D. Nojima, P. D. Kassner, S. Wang, M. M. Ollmann and H. J. Carlisle, *Autophagy*, 2016, **12**, 713-726.
111. K. Phadwal, J. Alegre-Abarrategui, A. S. Watson, L. Pike, S. Anbalagan, E. M. Hammond, R. Wade-Martins, A. McMichael, P. Klenerman and A. K. Simon, *Autophagy*, 2012, **8**, 677-689.
112. C. Follo, D. Barbone, W. G. Richards, R. Bueno and V. C. Broadus, *Autophagy*, 2016, **12**, 1180-1194.
113. H. C. Dooley, M. Razi, H. E. Polson, S. E. Girardin, M. I. Wilson and S. A. Tooze, *Mol Cell*, 2014, **55**, 238-252.
114. A. Gaugel, D. Bakula, A. Hoffmann and T. Proikas-Cezanne, *J Mol Signal*, 2012, **7**, 16.
115. Q. Lu, P. Yang, X. Huang, W. Hu, B. Guo, F. Wu, L. Lin, A. L. Kovacs, L. Yu and H. Zhang, *Dev Cell*, 2011, **21**, 343-357.
116. M. Mauthe, A. Jacob, S. Freiburger, K. Hentschel, Y. D. Stierhof, P. Codogno and T. Proikas-Cezanne, *Autophagy*, 2011, **7**, 1448-1461.
117. H. E. Polson, J. de Lartigue, D. J. Rigden, M. Reedijk, S. Urbe, M. J. Clague and S. A. Tooze, *Autophagy*, 2010, **6**, 506-522.
118. A. K. Thost, P. Donnes, O. Kohlbacher and T. Proikas-Cezanne, *Methods*, 2015, **75**, 69-78.
119. L. Galluzzi, E. H. Baehrecke, A. Ballabio, P. Boya, J. M. Bravo-San Pedro, F. Cecconi, A. M. Choi, C. T. Chu, P. Codogno, M. I. Colombo, A. M. Cuervo, J. Debnath, V. Deretic, I. Dikic, E. L. Eskelinen, G. M. Fimia, S. Fulda, D. A. Gewirtz, D. R. Green, M. Hansen, J. W. Harper, M. Jaattela, T. Johansen, G. Juhasz, A. C. Kimmelman, C. Kraft, N. T. Ktistakis, S. Kumar, B. Levine, C. Lopez-Otin, F. Madeo, S. Martens, J. Martinez, A. Melendez, N. Mizushima, C. Munz, L. O. Murphy, J. M. Penninger, M. Piacentini, F. Reggiori, D. C. Rubinsztein, K. M. Ryan, L. Santambrogio, L. Scorrano, A. K. Simon, H. U. Simon, A. Simonsen, N. Tavernarakis, S. A. Tooze, T. Yoshimori, J. Yuan, Z. Yue, Q. Zhong and G. Kroemer, *EMBO J*, 2017, **36**, 1811-1836.
120. J. C. Farre and S. Subramani, *Nat Rev Mol Cell Biol*, 2016, **17**, 537-552.



121. I. Kissova, B. Salin, J. Schaeffer, S. Bhatia, S. Manon and N. Camougrand, *Autophagy*, 2007, **3**, 329-336.
122. F. Reggiori, I. Monastyrskaya, T. Shintani and D. J. Klionsky, *Mol Biol Cell*, 2005, **16**, 5843-5856.
123. S. Schuck, C. M. Gallagher and P. Walter, *J Cell Sci*, 2014, **127**, 4078-4088.
124. C. Kraft, A. Deplazes, M. Sohrmann and M. Peter, *Nat Cell Biol*, 2008, **10**, 602-610.
125. B. Ossareh-Nazari, M. Bonizec, M. Cohen, S. Dokudovskaya, F. Delalande, C. Schaeffer, A. Van Dorselaer and C. Dargemont, *EMBO Rep*, 2010, **11**, 548-554.
126. R. Singh, S. Kaushik, Y. Wang, Y. Xiang, I. Novak, M. Komatsu, K. Tanaka, A. M. Cuervo and M. J. Czaja, *Nature*, 2009, **458**, 1131-1135.
127. Y. H. Hung, L. M. Chen, J. Y. Yang and W. Y. Yang, *Nat Commun*, 2013, **4**, 2111.
128. I. Maejima, A. Takahashi, H. Omori, T. Kimura, Y. Takabatake, T. Saitoh, A. Yamamoto, M. Hamasaki, T. Noda, Y. Isaka and T. Yoshimori, *EMBO J*, 2013, **32**, 2336-2347.
129. J. Huang and J. H. Brumell, *Nat Rev Microbiol*, 2014, **12**, 101-114.
130. A. Schlegel, T. H. Giddings, Jr., M. S. Ladinsky and K. Kirkegaard, *J Virol*, 1996, **70**, 6576-6588.
131. J. D. Mancias, X. Wang, S. P. Gygi, J. W. Harper and A. C. Kimmelman, *Nature*, 2014, **509**, 105-109.
132. G. Biasiotto, D. Di Lorenzo, S. Archetti and I. Zanella, *Mol Neurobiol*, 2016, **53**, 5542-5574.
133. R. S. Marshall, F. Li, D. C. Gemperline, A. J. Book and R. D. Vierstra, *Mol Cell*, 2015, **58**, 1053-1066.
134. R. S. Marshall, F. McLoughlin and R. D. Vierstra, *Cell Rep*, 2016, **16**, 1717-1732.
135. L. M. Delbridge, K. M. Mellor, D. J. Taylor and R. A. Gottlieb, *Am J Physiol Heart Circ Physiol*, 2015, **308**, H1194-1204.
136. D. Mijaljica, M. Prescott and R. J. Devenish, *Nucleus*, 2010, **1**, 213-223.
137. M. E. Papandreou and N. Tavernarakis, *Cell Death Differ*, 2019, **26**, 630-639.
138. B. Kalyanaraman, G. Cheng, M. Hardy, O. Ouari, M. Lopez, J. Joseph, J. Zielonka and M. B. Dwinell, *Redox Biol*, 2018, **14**, 316-327.
139. J. J. Lemasters, *Rejuvenation Res*, 2005, **8**, 3-5.
140. C. De Duve and R. Wattiaux, *Annu Rev Physiol*, 1966, **28**, 435-492.
141. K. Okamoto, N. Kondo-Okamoto and Y. Ohsumi, *Dev Cell*, 2009, **17**, 87-97.
142. T. Kanki, K. Wang and D. J. Klionsky, *Autophagy*, 2010, **6**, 278-280.
143. T. Kanki, K. Wang, Y. Cao, M. Baba and D. J. Klionsky, *Dev Cell*, 2009, **17**, 98-109.
144. M. Kundu, T. Lindsten, C. Y. Yang, J. Wu, F. Zhao, J. Zhang, M. A. Selak, P. A. Ney and C. B. Thompson, *Blood*, 2008, **112**, 1493-1502.
145. M. Mortensen, D. J. Ferguson, M. Edelmann, B. Kessler, K. J. Morten, M. Komatsu and A. K. Simon, *Proc Natl Acad Sci U S A*, 2010, **107**, 832-837.
146. J. Zhang, M. S. Randall, M. R. Loyd, F. C. Dorsey, M. Kundu, J. L. Cleveland and P. A. Ney, *Blood*, 2009, **114**, 157-164.
147. R. L. Schweers, J. Zhang, M. S. Randall, M. R. Loyd, W. Li, F. C. Dorsey, M. Kundu, J. T. Opferman, J. L. Cleveland, J. L. Miller and P. A. Ney, *Proc Natl Acad Sci U S A*, 2007, **104**, 19500-19505.
148. H. Sandoval, P. Thiagarajan, S. K. Dasgupta, A. Schumacher, J. T. Prchal, M. Chen and J. Wang, *Nature*, 2008, **454**, 232-235.
149. W. Aerbajinai, M. Giattina, Y. T. Lee, M. Raffeld and J. L. Miller, *Blood*, 2003, **102**, 712-717.
150. M. Schwarten, J. Mohrluder, P. Ma, M. Stoldt, Y. Thielmann, T. Stangler, N. Hersch, B. Hoffmann, R. Merkel and D. Willbold, *Autophagy*, 2009, **5**, 690-698.
151. I. Novak, V. Kirkin, D. G. McEwan, J. Zhang, P. Wild, A. Rozenknop, V. Rogov, F. Lohr, D. Popovic, A. Occhipinti, A. S. Reichert, J. Terzic, V. Dotsch, P. A. Ney and I. Dikic, *EMBO Rep*, 2010, **11**, 45-51.
152. E. M. Valente, P. M. Abou-Sleiman, V. Caputo, M. M. Muqit, K. Harvey, S. Gispert, Z. Ali, D. Del Turco, A. R. Bentivoglio, D. G. Healy, A. Albanese, R. Nussbaum, R. Gonzalez-Maldonado, T. Deller, S. Salvi, P. Cortelli, W. P. Gilks, D. S. Latchman, R. J. Harvey, B. Dallapiccola, G. Auburger and N. W. Wood, *Science*, 2004, **304**, 1158-1160.
153. T. Kitada, S. Asakawa, N. Hattori, H. Matsumine, Y. Yamamura, S. Minoshima, M. Yokochi, Y. Mizuno and N. Shimizu, *Nature*, 1998, **392**, 605-608.
154. I. E. Clark, M. W. Dodson, C. Jiang, J. H. Cao, J. R. Huh, J. H. Seol, S. J. Yoo, B. A. Hay and M. Guo, *Nature*, 2006, **441**, 1162-1166.
155. J. Park, S. B. Lee, S. Lee, Y. Kim, S. Song, S. Kim, E. Bae, J. Kim, M. Shong, J. M. Kim and J. Chung, *Nature*, 2006, **441**, 1157-1161.
156. D. Narendra, A. Tanaka, D. F. Suen and R. J. Youle, *J Cell Biol*, 2008, **183**, 795-803.
157. K. Mizumura, S. M. Cloonan, K. Nakahira, A. R. Bhashyam, M. Cervo, T. Kitada, K. Glass, C. A. Owen, A. Mahmood, G. R. Washko, S. Hashimoto, S. W. Ryter and A. M. Choi, *J Clin Invest*, 2014, **124**, 3987-4003.
158. Y. Kageyama, M. Hoshijima, K. Seo, D. Bedja, P. Sysa-Shah, S. A. Andrabi, W. Chen, A. Hoke, V. L. Dawson, T. M. Dawson, K. Gabrielson, D. A. Kass, M. Iijima and H. Sesaki, *EMBO J*, 2014, **33**, 2798-2813.
159. B. Bingol, J. S. Tea, L. Phu, M. Reichelt, C. E. Bakalarski, Q. Song, O. Foreman, D. S. Kirkpatrick and M. Sheng, *Nature*, 2014, **510**, 370-375.
160. N. Sun, J. Yun, J. Liu, D. Malide, C. Liu, Rovira, II, K. M. Holmstrom, M. M. Fergusson, Y. H. Yoo, C. A. Combs and T. Finkel, *Mol Cell*, 2015, **60**, 685-696.
161. G. F. Allen, R. Toth, J. James and I. G. Ganley, *EMBO Rep*, 2013, **14**, 1127-1135.
162. T. G. McWilliams, A. R. Prescott, G. F. Allen, J. Tamjar, M. J. Munson, C. Thomson, M. M. Muqit and I. G. Ganley, *J Cell Biol*, 2016, **214**, 333-345.
163. R. Loew, N. Heinz, M. Hampf, H. Bujard and M. Gossen, *BMC Biotechnol*, 2010, **10**, 81.
164. T. G. McWilliams, A. R. Prescott, L. Montava-Garriga, G. Ball, F. Singh, E. Barini, M. M. K. Muqit, S. P. Brooks and I. G. Ganley, *Cell Metab*, 2018, **27**, 439-449 e435.
165. G. Hernandez, C. Thornton, A. Stotland, D. Lui, J. Sin, J. Ramil, N. Magee, A. Andres, G. Quarato, R. S. Carreira, M. R. Sayen, R. Wolkowicz and R. A. Gottlieb, *Autophagy*, 2013, **9**, 1852-1861.
166. V. Rogov, V. Dotsch, T. Johansen and V. Kirkin, *Mol Cell*, 2014, **53**, 167-178.
167. N. Mizushima, B. Levine, A. M. Cuervo and D. J. Klionsky, *Nature*, 2008, **451**, 1069-1075.
168. D. C. Rubinsztein, *Nature*, 2006, **443**, 780-786.

169. R. A. Nixon, *Nat Med*, 2013, **19**, 983-997.
170. S. T. Stern and D. N. Johnson, *Autophagy*, 2008, **4**, 1097-1100.
171. J. J. Shacka, K. A. Roth and J. Zhang, *Front Biosci*, 2008, **13**, 718-736.
172. A. Ashkenazi, C. F. Bento, T. Ricketts, M. Vicinanza, F. Siddiqi, M. Pavel, F. Squitieri, M. C. Hardenberg, S. Imarisio, F. M. Menzies and D. C. Rubinshtein, *Nature*, 2017, **545**, 108-111.
173. M. Martinez-Vicente, Z. Tallozy, E. Wong, G. Tang, H. Koga, S. Kaushik, R. de Vries, E. Arias, S. Harris, D. Sulzer and A. M. Cuervo, *Nat Neurosci*, 2010, **13**, 567-576.
174. A. F. J. Janssen, E. A. Katrukha, W. van Straaten, P. Verlhac, F. Reggiori and L. C. Kapitein, *Nat Commun*, 2018, **9**, 4245.
175. J. A. Johnston, C. L. Ward and R. R. Kopito, *J Cell Biol*, 1998, **143**, 1883-1898.
176. J. S. Ju, S. E. Miller, E. Jackson, K. Cadwell, D. Piwnicka-Worms and C. C. Wehl, *Autophagy*, 2009, **5**, 511-519.
177. T. Farkas, M. Hoyer-Hansen and M. Jaattela, *Autophagy*, 2009, **5**, 1018-1025.
178. A. E. Majeski and J. F. Dice, *Int J Biochem Cell Biol*, 2004, **36**, 2435-2444.
179. S. J. Orenstein and A. M. Cuervo, *Semin Cell Dev Biol*, 2010, **21**, 719-726.
180. Douglas R. Green and B. Levine, *Cell*, 2014, **157**, 65-75.
181. J. Fred Dice, *Trends in Biochemical Sciences*, 1990, **15**, 305-309.
182. H. L. Chiang, S. R. Terlecky, C. P. Plant and J. F. Dice, *Science*, 1989, **246**, 382-385.
183. J. F. Dice, *J Biol Chem*, 1982, **257**, 14624-14627.
184. V. Arndt, N. Dick, R. Tawo, M. Dreiseidler, D. Wenzel, M. Hesse, D. O. Furst, P. Saftig, R. Saint, B. K. Fleischmann, M. Hoch and J. Hohfeld, *Curr Biol*, 2010, **20**, 143-148.
185. R. Sahu, S. Kaushik, C. C. Clement, E. S. Cannizzo, B. Scharf, A. Follenzi, I. Potolicchio, E. Nieves, A. M. Cuervo and L. Santambrogio, *Dev Cell*, 2011, **20**, 131-139.
186. A. M. Cuervo and J. F. Dice, *Science*, 1996, **273**, 501-503.
187. A. M. Cuervo and J. F. Dice, *J Cell Sci*, 2000, **113 Pt 24**, 4441-4450.
188. J. V. Ferreira, H. Fofo, E. Bejarano, C. F. Bento, J. S. Ramalho, H. Girao and P. Pereira, *Autophagy*, 2013, **9**, 1349-1366.
189. F. A. Agarraberes and J. F. Dice, *J Cell Sci*, 2001, **114**, 2491-2499.
190. N. Salvador, C. Aguado, M. Horst and E. Knecht, *J Biol Chem*, 2000, **275**, 27447-27456.
191. A. M. Cuervo, J. F. Dice and E. Knecht, *J Biol Chem*, 1997, **272**, 5606-5615.
192. F. A. Agarraberes, S. R. Terlecky and J. F. Dice, *J Cell Biol*, 1997, **137**, 825-834.
193. E. L. Eskelinen, A. M. Cuervo, M. R. Taylor, I. Nishino, J. S. Blum, J. F. Dice, I. V. Sandoval, J. Lippincott-Schwartz, J. T. August and P. Saftig, *Traffic*, 2005, **6**, 1058-1061.
194. U. Bandyopadhyay, S. Sridhar, S. Kaushik, R. Kiffin and A. M. Cuervo, *Mol Cell*, 2010, **39**, 535-547.
195. U. Bandyopadhyay, S. Kaushik, L. Varticovski and A. M. Cuervo, *Mol Cell Biol*, 2008, **28**, 5747-5763.
196. A. K. Rout, M. P. Strub, G. Piszczek and N. Tjandra, *J Biol Chem*, 2014, **289**, 35111-35123.
197. R. Valdor, E. Mocholi, Y. Botbol, I. Guerrero-Ros, D. Chandra, H. Koga, C. Gravekamp, A. M. Cuervo and F. Macian, *Nat Immunol*, 2014, **15**, 1046-1054.
198. R. Kiffin, C. Christian, E. Knecht and A. M. Cuervo, *Mol Biol Cell*, 2004, **15**, 4829-4840.
199. C. Park, Y. Suh and A. M. Cuervo, *Nat Commun*, 2015, **6**, 6823.
200. M. E. Hubbi, D. M. Gilkes, H. Hu, Kshitiz, I. Ahmed and G. L. Semenza, *Proc Natl Acad Sci U S A*, 2014, **111**, E3325-3334.
201. V. Liss, B. Barlag, M. Nietschke and M. Hensel, *Sci Rep*, 2015, **5**, 17740.
202. G. V. Los, L. P. Encell, M. G. McDougall, D. D. Hartzell, N. Karassina, C. Zimprich, M. G. Wood, R. Learish, R. F. Ohana, M. Urh, D. Simpson, J. Mendez, K. Zimmerman, P. Otto, G. Vidugiris, J. Zhu, A. Darzins, D. H. Klaubert, R. F. Bulleit and K. V. Wood, *ACS Chem Biol*, 2008, **3**, 373-382.
203. T. Seki, K. I. Yoshino, S. Tanaka, E. Dohi, T. Onji, K. Yamamoto, I. Hide, H. L. Paulson, N. Saito and N. Sakai, *PLoS One*, 2012, **7**, e31232.
204. H. Koga, M. Martinez-Vicente, F. Macian, V. V. Verkhusha and A. M. Cuervo, *Nat Commun*, 2011, **2**, 386.
205. A. M. Cuervo, H. Hildebrand, E. M. Bomhard and J. F. Dice, *Kidney Int*, 1999, **55**, 529-545.
206. S. Dong, C. Aguirre-Hernandez, A. Scrivo, C. Eliscovich, E. Arias, J. J. Bravo-Cordero and A. M. Cuervo, *Nat Commun*, 2020, **11**, 645.
207. A. Scrivo, M. Bourdenx, O. Pampliega and A. M. Cuervo, *The Lancet Neurology*, 2018, **17**, 802-815.
208. I. Tasset and A. M. Cuervo, *The FEBS Journal*, 2016, **283**, 2403-2413.
209. R. Valdor, E. Mocholi, Y. Botbol, I. Guerrero-Ros, D. Chandra, H. Koga, C. Gravekamp, A. M. Cuervo and F. Macian, *Nature Immunology*, 2014, **15**, 1046-1054.
210. S. Kaushik and A. M. Cuervo, *Nature Reviews Molecular Cell Biology*, 2018, **19**, 365-381.
211. S. Chikte, N. Panchal and G. Warnes, *Cytometry Part A*, 2014, **85**, 169-178.
212. P. Boya, R. A. Gonzalez-Polo, N. Casares, J. L. Perfettini, P. Dessen, N. Larochette, D. Metivier, D. Meley, S. Souquere, T. Yoshimori, G. Pierron, P. Codogno and G. Kroemer, *Mol Cell Biol*, 2005, **25**, 1025-1040.
213. P. Boya, R.-A. Gonzalez-Polo, D. Poncet, K. Andreau, H. L. A. Vieira, T. Roumier, J.-L. Perfettini and G. Kroemer, *Oncogene*, 2003, **22**, 3927-3936.
214. S. Rodriguez-Enriquez, I. Kim, R. T. Currin and J. J. Lemasters, *Autophagy*, 2006, **2**, 39-46.
215. J. Y. Byun, C. H. Yoon, S. An, I. C. Park, C. M. Kang, M. J. Kim and S. J. Lee, *Carcinogenesis*, 2009, **30**, 1880-1888.
216. C. W. Leung, Z. Wang, E. Zhao, Y. Hong, S. Chen, R. T. Kwok, A. C. Leung, R. Wen, B. Li, J. W. Lam and B. Z. Tang, *Adv Healthc Mater*, 2016, **5**, 427-431.
217. L. Wang, Y. Xiao, W. Tian and L. Deng, *J Am Chem Soc*, 2013, **135**, 2903-2906.
218. H. Yu, Y. Xiao and L. Jin, *J Am Chem Soc*, 2012, **134**, 17486-17489.
219. P. Ning, L. Hou, Y. Feng, G. Xu, Y. Bai, H. Yu and X. Meng, *Chem Commun (Camb)*, 2019, **55**, 1782-1785.
220. M. Mauro-Lizcano, L. Esteban-Martinez, E. Seco, A. Serrano-Puebla, L. Garcia-Ledo, C. Figueiredo-Pereira, H. L. Vieira and P. Boya, *Autophagy*, 2015, **11**, 833-843.
221. F. Hu, X. Cai, P. N. Manghnani, Kenry, W. Wu and B. Liu, *Chem Sci*, 2018, **9**, 2756-2761.
222. W. Zhang, R. T. Kwok, Y. Chen, S. Chen, E. Zhao, C. Y. Yu, J. W. Lam, Q. Zheng and B. Z. Tang, *Chem Commun (Camb)*, 2015, **51**, 9022-9025.
223. C. Jin, J. Liu, Y. Chen, R. Guan, C. Ouyang, Y. Zhu, L. Ji and H. Chao, *Scientific Reports*, 2016, **6**.

224. M. H. Lee, N. Park, C. Yi, J. H. Han, J. H. Hong, K. P. Kim, D. H. Kang, J. L. Sessler, C. Kang and J. S. Kim, *J Am Chem Soc*, 2014, **136**, 14136-14142.
225. H. Iwashita, S. Torii, N. Nagahora, M. Ishiyama, K. Shioji, K. Sasamoto, S. Shimizu and K. Okuma, *ACS Chem Biol*, 2017, **12**, 2546-2551.
226. Y. Liu, J. Zhou, L. Wang, X. Hu, X. Liu, M. Liu, Z. Cao, D. Shangguan and W. Tan, *J Am Chem Soc*, 2016, **138**, 12368-12374.
227. L.-Q. Niu, J. Huang, Z.-J. Yan, Y.-H. Men, Y. Luo, X.-M. Zhou, J.-M. Wang and J.-H. Wang, *Spectrochimica Acta Part A: Molecular and Biomolecular Spectroscopy*, 2019, **207**, 123-131.
228. X. Li, Y. Hu, X. Li and H. Ma, *Anal Chem*, 2019, **91**, 11409-11416.
229. M. Y. Wu, K. Li, Y. H. Liu, K. K. Yu, Y. M. Xie, X. D. Zhou and X. Q. Yu, *Biomaterials*, 2015, **53**, 669-678.
230. Z. Zou, Q. Yan, S. Ai, P. Qi, H. Yang, Y. Zhang, Z. Qing, L. Zhang, F. Feng and R. Yang, *Anal Chem*, 2019, **91**, 8574-8581.
231. Z. Xue, H. Zhao, J. Liu, J. Han and S. Han, *Chem Sci*, 2017, **8**, 1915-1921.
232. Z. Xue, H. Zhao, J. Liu, J. Han and S. Han, *Analytical Chemistry*, 2017, **89**, 7795-7801.
233. E. M. McCormick, C. C. Muresku and M. J. Falk, *Curr Genet Med Rep*, 2018, **6**, 52-61.
234. A. Hahn and S. Zuryin, *Trends Cell Biol*, 2019, **29**, 227-240.
235. W. C. Copeland and M. J. Longley, *DNA Repair (Amst)*, 2014, **19**, 190-198.
236. N. Thakur, A. K. Sharma, H. Singh and S. Singh, *Cancer Invest*, 2020, **38**, 375-393.
237. S. Ambrosio and B. Majello, *Cancers (Basel)*, 2020, **12**.
238. X. Zou, Y. Shi, R. Zhu, J. Han and S. Han, *Anal Chem*, 2019, **91**, 15899-15907.
239. H. Zhang, X. Zhu, H. Li, G. Liu, J. Wang, A. Wang, L. Kong, W. Zhu and H. Zhou, *Anal Chem*, 2019, **91**, 14911-14919.
240. X. Zhu, G. Liu, Y. Bu, J. Zhang, L. Wang, Y. Tian, J. Yu, Z. Wu and H. Zhou, *Anal Chem*, 2020, **92**, 10815-10821.
241. M. N. Moore, *Autophagy*, 2008, **4**, 254-256.
242. M. B. Azad, Y. Chen and S. B. Gibson, *Antioxid Redox Signal*, 2009, **11**, 777-790.
243. L. Li, Y. Chen and S. B. Gibson, *Cell Signal*, 2013, **25**, 50-65.
244. Y. Lei, W. Ren, C. K. Wang, R. R. Tao, H. J. Xiang, L. L. Feng, Y. P. Gao, Q. Jiang, X. Li, Y. Hu and F. Han, *Theranostics*, 2019, **9**, 5672-5680.
245. L. Yang, Y. Chen, Z. Yu, W. Pan, H. Wang, N. Li and B. Tang, *ACS Appl Mater Interfaces*, 2017, **9**, 27512-27521.
246. Z. Chen, J. Li, X. Chen, J. Cao, J. Zhang, Q. Min and J. J. Zhu, *J Am Chem Soc*, 2015, **137**, 1903-1908.
247. H. Yamamoto, S. Kakuta, T. M. Watanabe, A. Kitamura, T. Sekito, C. Kondo-Kakuta, R. Ichikawa, M. Kinjo and Y. Ohsumi, *J Cell Biol*, 2012, **198**, 219-233.
248. M. Mari, J. Griffith, E. Rieter, L. Krishnappa, D. J. Klionsky and F. Reggiori, *J Cell Biol*, 2010, **190**, 1005-1022.
249. Y. Ohashi and S. Munro, *Mol Biol Cell*, 2010, **21**, 3998-4008.
250. K. Shirahama-Noda, S. Kira, T. Yoshimori and T. Noda, *J Cell Sci*, 2013, **126**, 4963-4973.
251. E. L. Axe, S. A. Walker, M. Manifava, P. Chandra, H. L. Roderick, A. Habermann, G. Griffiths and N. T. Ktistakis, *J Cell Biol*, 2008, **182**, 685-701.
252. T. Shpilka, E. Welter, N. Borovsky, N. Amar, F. Shimron, Y. Peleg and Z. Elazar, *Proc Natl Acad Sci U S A*, 2015, **112**, 1434-1439.
253. N. Dupont, S. Chauhan, J. Arko-Mensah, E. F. Castillo, A. Masedunskas, R. Weigert, H. Robenek, T. Proikas-Cezanne and V. Deretic, *Curr Biol*, 2014, **24**, 609-620.
254. Z. Zhuang, J. Dai, M. Yu, J. Li, P. Shen, R. Hu, X. Lou, Z. Zhao and B. Z. Tang, *Chemical Science*, 2020, **11**, 3405-3417.
255. Y. Huang, X. You, L. Wang, G. Zhang, S. Gui, Y. Jin, R. Zhao and D. Zhang, *Angewandte Chemie International Edition*, 2020, **59**, 10042-10051.
256. A. Stolz, A. Ernst and I. Dikic, *Nature Cell Biology*, 2014, **16**, 495-501.
257. A. Prince, S.-L. Lu, T. Kawabata, Y.-L. Cheng, H. Omori, M. Hamasaki, T. Kusaba, R. Iwamoto, H. Arimoto, T. Noda, Y.-S. Lin and T. Yoshimori, *PLOS Pathogens*, 2017, **13**.
258. V. Sharma, S. Verma, E. Seranova, S. Sarkar and D. Kumar, *Frontiers in Cell and Developmental Biology*, 2018, **6**.
259. C. Ito, Y. Saito, T. Nozawa, S. Fujii, T. Sawa, H. Inoue, T. Matsunaga, S. Khan, S. Akashi, R. Hashimoto, C. Aikawa, E. Takahashi, H. Sagara, M. Komatsu, K. Tanaka, T. Akaike, I. Nakagawa and H. Arimoto, *Mol Cell*, 2013, **52**, 794-804.
260. D. Takahashi, J. Moriyama, T. Nakamura, E. Miki, E. Takahashi, A. Sato, T. Akaike, K. Itto-Nakama and H. Arimoto, *Molecular Cell*, 2019, **76**, 797-810.e710.
261. D. Fracchiolla, J. Sawa-Makarska and S. Martens, *Autophagy*, 2017, **13**, 978-979.
262. A.-C. Jacomín, S. Samavedam, V. Promponas and I. P. Nezis, *Autophagy*, 2016, **12**, 1945-1953.
263. M. D. Smith, M. E. Harley, A. J. Kemp, J. Wills, M. Lee, M. Arends, A. von Kriegsheim, C. Behrends and S. Wilkinson, *Developmental Cell*, 2018, **44**, 217-232.e211.
264. H. An, A. Ordureau, J. A. Paulo, C. J. Shoemaker, V. Denic and J. W. Harper, *Molecular Cell*, 2019, **74**, 891-908.e810.
265. H. Chino, T. Hatta, T. Natsume and N. Mizushima, *Molecular Cell*, 2019, **74**, 909-921.e906.
266. H. An, A. Ordureau, M. Körner, J. A. Paulo and J. W. Harper, *Nature*, 2020, **583**, 303-309.
267. H. An and J. W. Harper, *Nature Cell Biology*, 2017, **20**, 135-143.
268. G. Filomeni, D. De Zio and F. Cecconi, *Cell Death Differ*, 2015, **22**, 377-388.
269. S. Galati, C. Boni, M. C. Gerra, M. Lazzaretti and A. Buschini, *Oxid Med Cell Longev*, 2019, **2019**, 5692958.
270. J. F. Moruno-Manchon, N.-E. Uzor, S. R. Kesler, J. S. Wefel, D. M. Townley, A. S. Nagaraja, S. Pradeep, L. S. Mangala, A. K. Sood and A. S. Tsvetkov, *Molecular and Cellular Neuroscience*, 2018, **86**, 65-71.
271. D. H. Cho, Y. S. Kim, D. S. Jo, S. K. Choe and E. K. Jo, *Mol Cells*, 2018, **41**, 55-64.